Spring 2015

Processing And Characterization Of Innovative Magnesium Alloys For Biodegradable Orthopaedic Implants

Christopher E. Smith
North Carolina Agricultural and Technical State University

Processing and Characterization of Innovative Magnesium Alloys for Biodegradable Orthopaedic Implants

Christopher E. Smith

North Carolina A&T State University

A dissertation submitted to the graduate faculty

in partial fulfillment of the requirements for the degree of

DOCTOR OF PHILOSOPHY

Department: Mechanical Engineering

Major: Mechanical Engineering

Major Professor: Dr. Jagannathan Sankar

Greensboro, North Carolina

2014

The Graduate School
North Carolina Agricultural and Technical State University
This is to certify that the Doctoral Dissertation of

Christopher E. Smith

has met the dissertation requirements of
North Carolina Agricultural and Technical State University

Greensboro, North Carolina
2014

Approved by:

Dr. Jagannathan Sankar Major Professor	Dr. Zhigang Xu Co-Advisor
Dr. Devdas Pai Committee Member	Dr. Yeoheung Yun Committee Member
Dr. Samuel P. Owusu-Ofori Department Chair	Dr. Jenora T. Waterman Committee Member

Dr. Sanjiv Sarin
Dean, The Graduate School

Biographical Sketch

Christopher E. Smith is a direct Ph. D. candidate researcher for the Engineering Research Center for Revolutionizing Metallic Biomaterials (ERC-RMB) in the Department of Mechanical Engineering at North Carolina A&T State University. He graduated from North Carolina A&T State University in May 2009 with a Bachelor of Science degree in mechanical engineering. Under the close tutelage of Dr. Jagannathan Sankar and Dr. Zhigang Xu, Christopher executed scientific research on biodegradable and bioabsorbable magnesium based alloys for Orthopaedic applications.

Christopher's research efforts are under the Engineering System I: Craniofacial and Orthopaedic research plan and Thrust I: New Materials Development section of the strategic plan for the ERC-RMB. Consequently, his research is in harmony with the ERC-RMB and its overall vision and goals. In addition, Christopher cultivated professional leadership skills outside of applied research in an effort to develop an advantage as a professional competitor on a global level. Throughout his matriculation through the Ph.D. program, Christopher has held positions on the Student Leadership Council (SLC) within the ERC as SLC President, Thrust I: New Materials Development student leader, SLC Professional Development leader, and Education and Outreach volunteer. As an Education and Outreach volunteer, he was vital in his participation in the NSF Science Technology Engineering and Mathematics Career Fair held in Dulles, Va, in September 2013, where he was able to increase awareness of research challenges and job opportunities in the growing biomedical field.

Dedication

To my siblings Adrian, Alex, and Danielle as well as my parents Angela Robinson and Vincent Smith, thank you for all your love and support.

Acknowledgements

I would like to express my sincere gratitude to my advisors Dr. Jagannathan Sankar and Dr. Zhigang Xu, for their guidance throughout my graduate studies. I am very grateful to have had your knowledge and expertise at my disposal throughout the rigorous and demanding commitment of my graduate studies.

I would like to thank my committee members Dr. Devdas Pai, Dr. Jenora Waterman, and Dr. Yeoheung Yun for their invaluable assistance, support and contribution towards the success of this research.

I would also like to acknowledge the help and support that I received from my colleagues and friends in the Engineering Research Center especially: Lauren Douglas-Byrd, Yongjun Chen, Da-Tren Chou, Dae Ho Hong, Christopher Mahoney, Eric Norman, Satish Singh, Juan Wang, Nevija Watson, Leon White, Ashlyn Worthy, and Nan Zhao.

This work was financially supported by the National Science Foundation Engineering Research Center for Revolutionizing Metallic Biomaterials. This support is greatly appreciated.

Finally and most importantly, I would like to acknowledge and express my sincere thanks to my Lord and Savior Jesus Christ for your spiritual, mental, and emotional blessings and support. I have truly matured and grown into a dynamic person these past few years which could not be accomplished without your grace, mercy, and patience.

Table of Contents

List of Figures

List of Tables

Abstract

There is a need for innovation in medical implant devices through novel biomaterials that will improve the quality of life. The first step in the creation of a foundation of knowledge and technology to improve these implant devices is through the creation of new alloys with the capabilities of biodegradation and bioabsorption without a toxic effect that will pass through FDA regulatory procedures. In this study, unique heat treatment processing techniques coupled with innovation in elemental alloying produced distinctive magnesium (Mg) based alloy systems. The MgZnCa system was used as the underpinning system where four groups of novel alloys were developed, which include the as-cast Mg−*x*Zn−0.3Ca system, the heat treated Mg−4.0Zn−0.3Ca system and as-cast and heat treated Mg−1.0Zn−0.3Ca system alloyed with 1.3% rare earth elements. All alloy groups were assessed through immersion corrosion tests utilizing 0.9% NaCl physiological solution and MEMα cell culture medium, tensile and compressive mechanical testing, and cytotoxicity assays. The increase of Zn content in the Mg−*x*Zn−0.3Ca system had an effect on phase precipitation and grain size refinement, which caused an increase in mechanical strength and a reduction of corrosion resistance up to a Zn content of 4.0 wt.%. The cytotoxicity assays determined that the Mg−4.0Zn−0.3Ca system showed negative cytocompatibility with the MC3T3-E1 cell line which can be reduced or eliminated by diluting the interaction between the two. The addition of rare earth elements caused significant grain size refinement, increased corrosion resistance, increased mechanical strength compared to the MgZnCa system, and positive cytocompatibility. Through this research, novel Mg-based alloys were developed with the potential of being employed as orthopaedic biomaterials capable of supporting the mechanical and physical function of an injured tissue throughout the entire healing process.

CHAPTER 1

Introduction

1.1 Orthopaedic Implants and the Medical Device Industry

Orthopaedics is a medical specialty that pertains to the diagnosis and treatment of disorders, conditions, and injuries of the musculoskeletal system. More specifically, orthopaedics is a branch of medicine focused on the skeletal system and related muscles, joints, ligaments, and tendons. It was reported that in 2012 the orthopaedic device market consisted of 9.4% of the worldwide device market share which was 4th in the Top 15 device areas [1]. Musculoskeletal ailments and injuries account for more than 130 million visits to orthopaedic specialists per year. One in four Americans suffer from musculoskeletal impairment resulting in more than $180 billion in sales annually [2]. In short, the orthopaedic device market is a large market. This is important because a larger market allows time for error and the development of valuable products, as well as time to produce a repeatable and scalable business model.

Orthopaedic fixation devices, which include joint reconstruction materials and biomaterials, are used in the reduction of fractures, bone manipulation, soft-tissue injuries, and reconstructive surgery. Reduction can be noninvasive (external splints and traction) or can involve surgery to implant and replace artificial joints. After fracture reduction, internal, external, or intramedullary fixation devices may be used to provide mechanical stability and maintain the alignment of bone fragments during the healing process. A fixation device must be strong and secure enough to allow early mobilization of the trauma area. Screws are used primarily to provide interfragmental compression or to attach plates, which can then provide compression, prevent displacement, and support the fragments during healing. Pins and wires can be used for fixation of small fragments or fractures in small bones [2, 3]. Figure 1 describes

commercial orthopaedic implant devices. In Figure 1a, the inferior view after the complete mandibular component has been inserted through soft tissue tunnels to the fossa regions. The chin bone has been attached with screws to the prosthesis. Figure 1b shows the right TMJ before closure. The condyle is seated in the posterior part of the fossa component [4]. Figure 1c illustrates the Anchorage™ Cross Plating System which uses an inset diagonal, cross-joint screw to develop true mechanical compression across the fusion site [5]. Lastly in Figure 1d, an interference screws is affixing a cadaveric ACL graft in where the arrows point out the pieces of cadaveric bone at both ends of the graft [6].

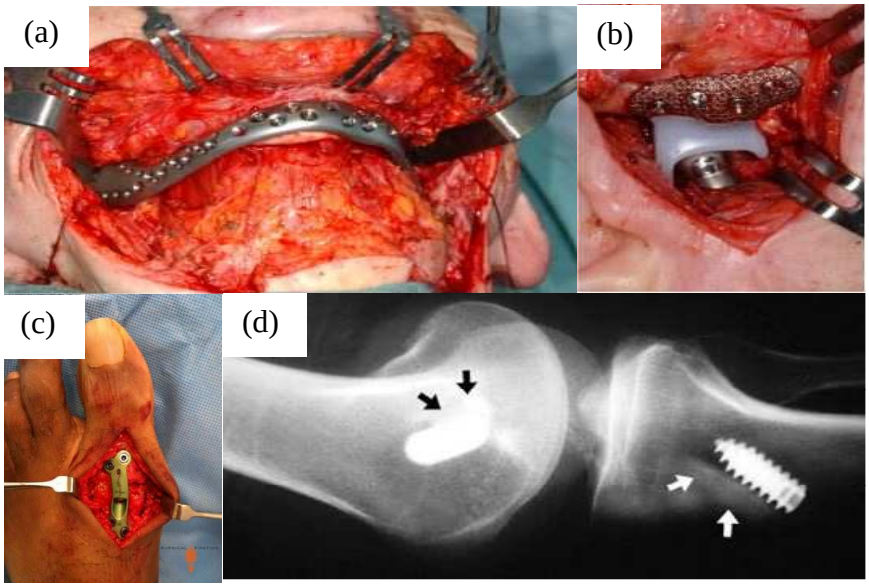

Figure 1. Examples of commercial orthopaedic implant devices.

The global orthopaedic sector is a dynamic component of the medical device industry. Highly competitive and forecasted to have a single-digit growth rate, the orthopaedic device market is primarily driven by artificial joints and orthobiologics which are estimated to be worth $17.5 billion and $9.6 billion by 2016 respectively. Segment growth is also boosted by the increase in knee implants and hip and knee replacements. By 2015 the world orthopaedic prosthesis market is anticipated to reach $19.4 billion, with growth driven by rising degenerative

joint diseases like osteoporosis and arthritis. The main cause is an aging global population and the desire to keep up an active lifestyle [2].

Although financial demographics remain favorable, medical devices have evolved and become more complex. Consequently, the federal device-approval regulatory system has become more stringent and scrutinized. The United States congress requires that high risk medical devices should be sanctioned through a more rigorous premarket approval (PMA) process, which requires clinical testing. Moreover, the Safe Medical Devices Act of 1990 requires the FDA to either use the PMA process for high risk devices or reclassify them in a lower-risk category [7]. As a result, the medical device industry continues to feel a profound impact from a slowdown in procedure volumes coupled with uncertainties and delays at the FDA. In 2001, the U.S. House Energy and Commerce Subcommittee on Oversight and Investigations held a hearing entitled "Medical Device Regulation: Impact on American Patients, Innovation, and Jobs." In this hearing, Congressman Cliff Stearns argued that FDA regulation of medical devices is too arduous which stifles innovation and drives device manufacturer overseas [7].

Furthermore, there have been disagreements between FDA leadership and the medical device industry and politicians from states where device companies are located concerning the clearance process. The Institute of Medicine (IOM) released an FDA-commissioned report in 2011 on the 510(k) clearance process and it concluded that it was impossible for 510(k) clearance to assure the safety and effectiveness of devices and therefore recommended that it be eliminated. FDA leadership however does not intend to implement this key recommendation of the report [7].

Generating innovative products in the medical device industry has a lot of challenges that must be addressed. Proper physical and chemical characterization along with thorough biological

assessment of new medical devices and materials is vital to the success of future product commercialization.

1.2 Degradable Biomaterials

The first step in the creation of a foundation of knowledge and technology to improve orthopaedic implant devices is through the creation of new alloys with the capabilities of biodegradation and bioabsorption without a toxicity effect. The degradation properties of biodegradable implants in physiological environments are the key component in the interest of implementing these types of implants for medical purposes. Metals, ceramics, and polymers can all be used as biomaterials for implants. Physical properties of metals such as high impact strength, high wear resistance, high ductility, and the ability to absorb high strain energy make them applicable for orthopaedic load-bearing applications and fixation devices [8]. The implementation of metallic degradable biomaterials as an implant material is not a novel concept. In 1878, physician Edward C. Huse used Mg wires as ligatures to stop bleeding vessels of three human patients [8, 9].

Commonly used biomaterials include stainless steel, titanium, and cobalt-chromium based alloys because of their corrosion resistance, and consequently they are inherently permanent type of alloys. Biodegradability and biocompatibility are characteristics that gives an advantage to implants with these capabilities because they would be able to be resorbed and expelled safely out the body after the trauma site is healed, eliminating the need for iterative surgeries. In an effort to make more biocompatible implants, the emphasis for contemporary implants is not only on devices that are able to physically function in complex biological systems, but that will be successfully accepted by the body [8]. Surgeon Erwin Payr was one of the most influential pioneers of medicine whose versatile clinical applications and reports

inspired the advancement in the field of biodegradable Mg implants to various surgical areas. He first started experiments on Mg resorption in 1892 and by 1900 he proposed that tissue oxygen and water content, carbon dioxide, dissolved salts in blood, and the chemical processes in cells were mainly responsible for Mg corrosion *in vivo* [9].

Mg and Mg-based alloys have been investigated as implants for over 100 years. Implants containing Mg and Mg-based alloys are limited in the amount of approved alloys for commercial use. Due to Mg's good biocompatibility and biodegradability, and the possibility for bone generation engenders encouragement for biodegradable Mg implants for orthopaedic implant applications.

1.3 Research Objectives

The aim for this study is to provide innovation in medical devices that improve the quality of life through the development of novel Mg alloys with the capabilities of biodegradation without rendering a cytotoxic effect. More specifically, to create an assortment of uniquely composed and processed biodegradable Mg alloys that have the potential to meet different orthopaedic device requirements. To accomplish this, all alloys are produced according to the "Design and Assessment for New Alloy Development" research plan flow chart in Figure 2. This chart is designed as a standard for materials development to promote consistency when fabricating and characterizing all new materials developed in this study. The design objectives for the alloys presented in this dissertation are driven by the "Device Design" requirements and criteria of current orthopaedic medical devices which are described in the gray section. The research detailed in this dissertation falls under the "Materials Development" section of the flow chart.

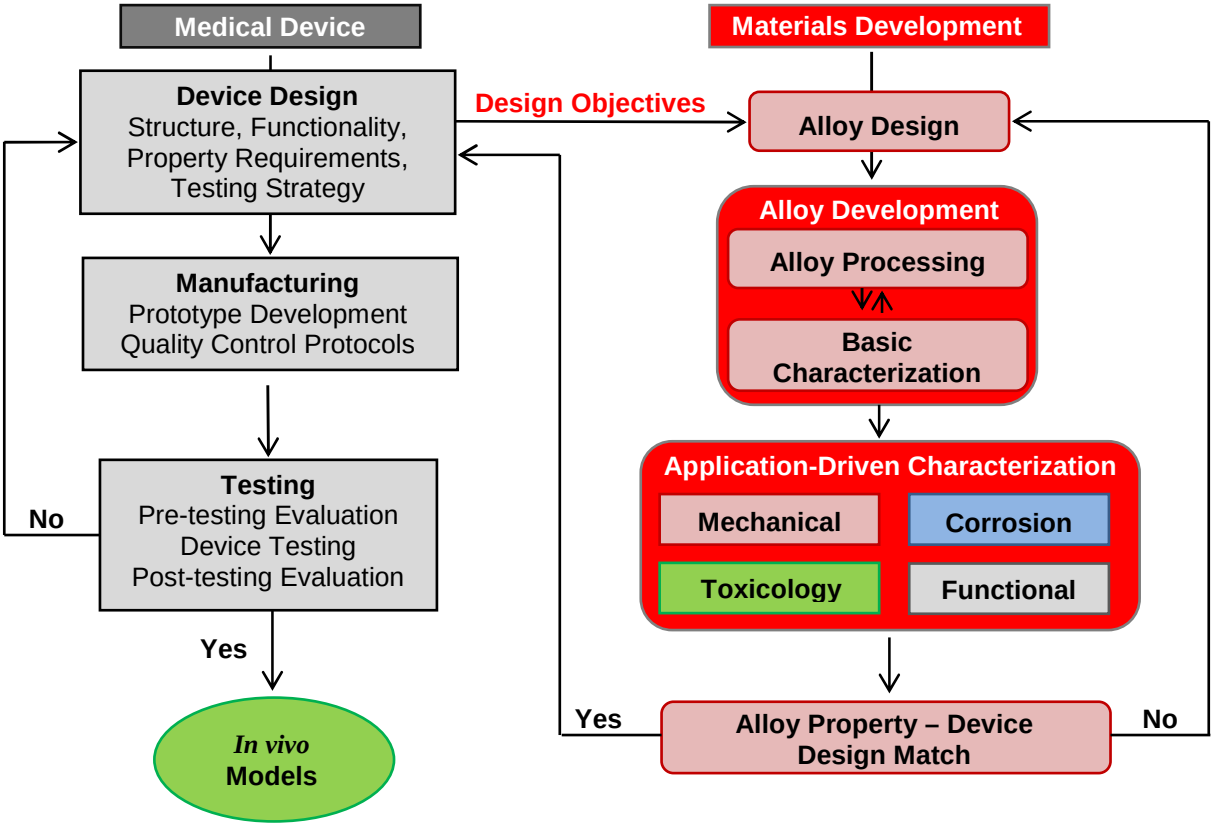

Figure 2. Design and assessment for "New Alloy Development" flow chart.

1.4 Dissertation Layout

The work presented in this dissertation has been organized under five chapters. Chapter 1 is dedicated to the introduction and explanation of pertinent background information to give a better perspective for the research work presented in the study. It encompasses the orthopaedic implant and medical device industry in which this research is purposed for, biodegradable materials and alloy development as well as specific research objectives for this study.

Chapter 2 incorporates a comprehensive look into specific scientific literature and commercial patents relevant to the work presented in this dissertation.

In Chapter 3, the concepts, set-up, and specifications of the experimental methods and material characterizations are discussed.

Chapter 4 is devoted to the results and discussion of all experimental procedures used in this research work. Furthermore, recommendations for alloys produced in this study for orthopaedic applications and future research work based on experimental results and inherent opportunities.

Lastly, Chapter 5 summarizes this dissertation and the potential impact of the research presented.

CHAPTER 2

Literature Review

The main focus of this chapter is to review pertinent background information and academic literature relevant to this field of study. Key theories and nomenclature will also be discussed. In this chapter, current academic studies involving the fabrication and characterization of biodegradable biomaterials consisting of Mg, zinc (Zn), and/or calcium (Ca) elements for biomedical applications are discussed. Additionally, relevant existing commercial patents are examined. Through the exploration of several current academic studies and commercial patents, the research work in this study will have a foundation of pertinent information to compare and contrast the novelty and impact of the results of this investigation.

2.1 History of Magnesium

Even though the history of Mg started in 1755 with the discovery of elementary Mg contained within magnesia by Scottish chemist Joseph Black, the British chemist Sir Humphrey Davy is credited as discoverer because he isolated the metal in 1808 [9, 10]. Sir Davy decomposed wet Mg sulfate through electrolysis using a voltaic cell and a mercury cathode [10]. In 1831, the French chemist Antoine Alexandre Brutus Bussy discovered a way to isolate Mg in large quantities by fusing dehydrated Mg chloride with potassium at elevated temperatures. He published his findings in the *'Mémoire sur le Radical métallique de la Magnésie'* shortly after. Subsequently, British scientist and former Sir Humphrey Davy assistant Michael Faraday reduced dehydrated Mg chloride by electrolysis and obtained pure metallic Mg in 1833 [10].

Throughout history, Mg found steady interest only in Germany, which, in 1868, was the only producer in the world. On April 9, 1885, Aluminium und Magnesiumfabrik Hemelingen was founded and started producing aluminum (Al) and Mg in an electrolytic process [10]. After

years of advancement in the Mg production process and federal safety regulations, by 1915, Germany remained the sole producer of Mg. In 1924 Mg alloys (AZ: 2.5-3.0% AL, 3.0-4.0% Zn) were used for the first time as pistons in automobiles [10]. The application of Mg was extended to a number of airship parts which included girdle connectors, steering gear fittings, and anchor cable sheaves. Furthermore, Mg castings were introduced into cars on a larger scale by German automotive engineer Ferdinand Porsche. As the years progressed, Mg production and application grew and developed in Germany to include a patent for continuous production of metallic Mg through thermic reduction.

The production of Mg has seen fluctuations throughout the 1900s, from production peak in World War II, to the production decreasing drastically afterwards [10, 11]. In Germany, Mg production was prohibited and ultimately terminated due, in part, to material shortages and the Berufsverbot which was an order of professional disqualification or disentitlement.

In the United States, the Korean War created a need to revive Mg production in 1951 [10]. Part of the electrolytic plant of the Titanium Metals Corporation of America was reactivated in 1950 to produce Mg for titanium reduction. After the Korean War, a strategic stockpile of Mg was produced in the amount of 195,000 short tons, but the U.S. government eventually sold the entire supply by auction. As the years progressed, the production of Mg was developed for a number of applications that resulted in failure, but there was a level of success focused toward transportation applications because Mg is a strong light weight metal that has less density than aluminum and steel.

2.2 History of Magnesium Implants

The major limitation of Mg in many engineering applications is its low corrosion resistance [12]. However, this intriguing feature has made Mg a potential prospect for a new

class of implant biomaterials for orthopaedic applications. The employment of Mg in medical applications is not a new idea. In 1878, physician Edward C. Huse successfully stopped a bleeding vessel using a Mg wire ligature [9, 13]. He observed that the corrosion of Mg was slower *in vivo* and that the time period of complete degradation was dependent on the size of the Mg wire [8, 9]. In 1900, after concluding that the Mg wires Edward Huse implemented in his blood vessel procedures were too brittle to be suitable sutures, Austrian-German surgeon Erwin Payr investigated the use of thin-walled tubular Mg cylinders as replacement connectors for the anastomosis of arterial and venous blood vessels [14]. Using pigs and the femoral artery of dogs for his test trials, Payr discovered that the connection of blood vessel ends became solid after 8 days, and severely thickened intima later at the anastomosis. The vessel thickness returned to normal after he waited 8 more days before reinvestigating the anastomosis [9]. It was noted that only the Mg tubes that were positioned intravascularly caused thrombotic blood clotting and no thrombosis was observed in the Mg tubes positioned extravascularly.

In terms of musculoskeletal applications, in 1900, Payr introduced the idea of using Mg plates and sheets in joint arthoplastics to regain or preserve joint motion [9]. At the 29th Congress of the German Society for Surgery, Payr lectured on the subject of using Mg sheets and plates to prevent the reunion of dissected bone tissues by a dense fibrous layer after full resorption of the Mg metal [9, 15]. This inspired the investigation of using Mg to regain motion stiffness in joints through animal and human trials. Furthermore, Payr proposed the use of Mg implants which include fixator pins, nails, wires (cerclage), pegs, and cramps for musculoskeletal applications; more specifically using a Mg peg as a stabilizer for bone fractures and pseudarthrosis [9, 15].

In 1906, Albin Lambotte fixed a Mg plate using six steel screws at the tibia for stabilization of a fracture of the lower leg of a 17 year old child [16]. It was discovered that the

patient had a painful inflammatory reaction to the plate due to the electrochemical difference between the Mg plate and the steel screws. After further investigation and animal test trials, Lambotte began treating human patients with Mg implants under careful observation. He treated patients suffering from supracondylar fractures with Mg nails and observed that there was normal healing without complications except the development of gas cavities which disappeared after several weeks [17]. Lambotte also observed total Mg resorption at one year post surgery and physiological bone healing without any hypertrophic bone formation [9]. From these findings, Lambotte broaden his clinical investigation and ultimately discovered the Mg could only be implanted without combining other metallic implants to prevent electrolytic corrosion. Based on his good clinical results, Lambotte recommended the use of Mg implants in the following clinical areas: bennet fracture, scafoid fractures, foot surgery, clavicular fractures, carpus fractures, phalanx and metacarpal fractures, radius epiphyseal fractures, lower arm diaphyseal fractures, supra- and condylar fractures in children, humerus head fractures, malleolus fractures, oblique tibial fractures and pertrochantic fractures [9, 16].

There has also been other reports on the use of Mg in orthopaedic applications, which were mainly based on *in vivo* animal experiments [9]. In 1913, Ernest William Hey Groves published his work on using a Mg intramedullary peg for stabilizing fragments in a fracture of rabbits [18]. He discovered that Mg produced inflammation cavities and disintegrated so rapidly that he deemed it undesirable. In 1924, Arthur A. Zierold compared the reaction of Mg on bone and determined that Mg has little action other than as a connective tissue stimulant, and theorized that it may hinder as well as accelerate new bone production [9, 19]. After many experiments and thorough investigation on Mg and its alloys as implantable biomaterials throughout history, Mg has established itself as an intriguing element worth the scrutiny and scientific debate. The many

inherent benefits of Mg as an implantable material as well as a century of historical research has push Mg to the forefront of potentially revolutionizing the biomedical engineering landscape.

2.3 Alloy Design

2.3.1 Alloying. Alloying is crucial in modifying the corrosion resistance and mechanical properties of Mg [12, 20-23]. Alloying is the most effective method to modify the microstructures and properties of Mg-based alloys. For example, it was found that the addition of Zn can increase the age-hardening response of Mg alloys which can significantly enhance the mechanical properties and corrosion resistance [24, 25]. The ternary addition of Ca to the Mg−Zn system is effective for the improvement of mechanical properties [24, 25]. Moreover, the mixture of rare earth elements (REE) in combination with other metals such as silver, and a small amount of zirconium (Zr) which imparts a fine grain microstructure, can enhance the mechanical properties of Mg [12].

2.3.2 Material selection.

2.3.2.1 Magnesium. Mg is the fourth most abundant mineral in the body and is vital to certain biological functions. Mg is needed for more than 300 biochemical reactions in the body which include muscle contraction, bone metabolism, and cellular proliferation. It helps maintain normal muscle and nerve function, stabilizes normal heart rhythm, and supports a healthy immune system [26]. Nearly 50% of the total Mg element in the body is found in bone and the other half is found within cells of body tissues and organs [27-30]. Around 1% of Mg is found in blood, but the body works vigorously to keep Mg levels within the blood constant [26].

The most commonly used biomaterials for orthopaedic devices include stainless steel (SS), titanium (Ti), and cobalt-chromium (Co-Cr) based alloys. The possible release of toxic elements during corrosion or wear processes create a significant weakness to these alloys as

implantable biomaterials [12]. Mg has a density, elastic modulus, and compressive yield strength closer to that of natural bone than for SS, Ti, and Co-Cr alloys. These similarities in properties (Table 1) lead to minimal or no stress shield phenomena in Mg bone implants that occur with SS and Ti alloys [31]. Additionally, histological studies show that new bone formation is observed *in vivo* around Mg alloy implants without inflammation reaction [32, 33].

Table 1

Summary of the physical and mechanical properties of various implant materials in comparison to natural bone [12].

Properties	Natural Bone	Mg	Ti	Co-Cr	Stainless Steel	Artificial HA
Density (g/cm^3)	1.8-2.1	1.74-2.0	4.4-4.5	8.3-9.2	7.9-8.1	3.1
Elastic Modulus (GPa)	3.0-20	41-45	110-117	230	189-205	73-117
Compressive Yield Strength (MPa)	130-180	65-100	758-1117	450-1000	170-310	600
Fracture Toughness ($MPa \cdot m^{1/2}$)	3.0-6.0	15-40	55-115	N/A	50-200	0.7

In terms of limitations, the corrosion resistance of Mg presents a major complication in using it as an implant biomaterial [34]. Poor corrosion resistance of Mg alloys results from the high dissolution tendency of Mg and the presence of secondary phases acting as local cathodes causing micro-galvanic corrosion [35]. Consequently, Mg usually has a fast corrosion rate in electrolytic physiological environments [12, 31].

Most Mg alloys are produced through metal casting techniques. One of the inherent risks of metallic casting is the introduction of impurities or contaminants throughout the melt. Common impurities found in Mg alloys include iron, copper, and nickel. Iron, copper, and nickel

are detrimental to the corrosion resistance of Mg because they have low solid solubility limits and provide efficient and active cathodic sites. This can lead to severe galvanic corrosion. Matsubara *et al.* [36] concluded that the corrosion rate of AM50 and AM60 Mg alloys depended on the impurity concentration of iron and increased with the iron-manganese ratio. Additionally, impurities will also influence the microstructure and mechanical properties of Mg alloys. In ZK60 Mg alloys, lower impurity content exhibited finer grains and subsequently an increase of the yield strength in the as-extruded alloy was observed [37]. It is clear impurity content must be considered in terms of producing successful Mg alloys for commercial use.

2.3.2.2 Calcium. Ca is the most abundant mineral in the body and the fifth most abundant element by mass in the Earth's crust. Ca is a silvery white alkaline soft metal and is essential to all living things [38]. The average human contains about one kg of Ca, and Ca phosphate is the main component of human bone. In terms of biological function, Ca is required for vascular contraction and vasodilation, muscle function, nerve transmission, intracellular signaling and hormonal secretion; though less than 1% of total body Ca is needed to support these critical metabolic functions [39]. The remaining 99% of the body's Ca supply is stored within the bones and teeth to support their structure and function. Bone undergoes continuous remodeling with constant resorption and deposition of Ca into new bone.

According to the Mg−Ca binary phase diagram, at 516°C, the maximum solubility of Ca in Mg is 1.34 wt%. Li *et al.* [40] designed experimental alloys with a Ca content ranging from 1-20 wt%. It was discovered that the as-cast Mg−5, 10, and 20Ca alloys were very brittle at room temperature and could be easily broken. Consequently, the Mg−Ca alloys had to be designed with low Ca contents (1-3 wt.%). Li *et al.* ascertained from XRD patterns that the formation of the secondary phase could be identified as Mg_2Ca. The EDS analysis indicated that the grain

boundaries were rich in Ca suggesting that the Mg_2Ca phase precipitated along the grain boundaries. However, inadequate mechanical properties as well as lower corrosion resistance were two major limitations of the Mg−Ca binary alloy.

Bettles *et al.* [41] reported that the addition of trace amounts of Ca to a Mg−Zn system led to a significant enhancement of age-hardening response by the refinement of the resulting precipitate microstructure. In conjunction with the enhancement of the age-hardening response by the addition of Ca, the optimization of the heat treatment cycle will result in further improvements to the material properties.

2.3.2.3 Zinc. Zn is a metallic chemical element and is, in some respects, chemically similar to Mg in terms of its ion size and its only common oxidation state of +2. Zn is the 24th most abundant element in the Earth's crust and is an essential mineral required by the body for keeping a healthy immune system, building proteins, triggering enzymes and creating DNA [42].

Metallic Zn appeared much later in history than the other common metals [43]. Copper, lead, tin, and iron can be obtained by a process called reduction, where their oxide ores are heated with carbon to produce these elements as molten metals. Zn oxide, however, cannot be reduced by carbon until temperatures exceed over its boiling point of 907°C and thus furnaces developed to smelt the other metals could not produce Zn.

There are substantial benefits to utilizing Zn as an alloying element in Mg-based alloys. It has been shown that Zn can significantly enhance the tensile strength, elongation and corrosion resistance of Mg alloys. Du *et al.* [25] concluded that the addition of Zn is helpful to refine the grain size of the as-cast Mg-3 wt.%Ca alloy. The grain boundaries become thinner and the grain size is refined. Grain refinement is important in alloy development because it can improve mechanical property and reduce corrosion rate. It was determined that the Mg−3 wt.%Ca−2

wt.%Zn alloy shows higher mechanical strength and ductility than Mg−3 wt.%Ca [25]. Additionally, the eutectic ($Mg+Mg_2Ca+Ca_2Mg_6Zn_3$) phase in the Mg−3 wt.%Ca−2 wt.%Zn alloy was found to improve its anticorrosion properties through potential dynamic polarization [25]. The addition of the Zn element shifts the corrosion potential towards the noble direction. Du *et al.* [25] also found that the ultimate tensile strength of Mg−3Ca alloys is increased significantly by adding the Zn element.

Sun *et al.* [44] prepared an Mg−4.0Zn−0.2Ca alloy for their investigation. XRD scans were used to examine the phase of the as-cast alloy from 20 to 90° with a step size of 0.05 (Figure 3). Peaks from α-Mg, $Ca_2Mg_6Zn_3$, and $Ca_2Mg_5Zn_{13}$ were discerned in the as-cast alloy. Additionally, the average grain size of the primary α-Mg phase was calculated to be 100-130 µm (Table 2) and the spherical secondary phases had an average diameter of 1-2 µm which were distributed mainly within the grains.

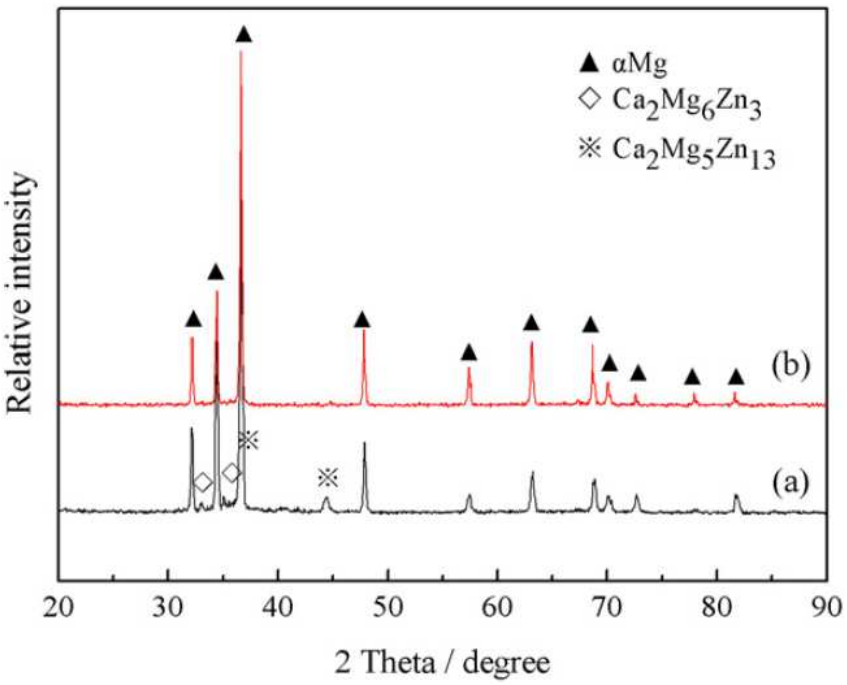

Figure 3. X-ray diffraction patterns of Mg−4.0Zn−0.2Ca alloys; (a) as-cast, (b) extruded [44].

Langelier *et al.* [45] found that the addition of Zn to the Mg−Ca alloy system resulted in significant improvement in the hardening capabilities through altering the precipitation process and refining the precipitate distribution. This improvement in precipitation hardening can be maximized by adding Zn in levels lower than its solid solubility limit.

Ohishi *et al.* [46] explored the optimum Zn composition for age-hardening in the Mg−Zn−Ca ternary system. Table 3 list the compositions of the investigated alloys in both at.% and wt.%. The Ca content of all alloy samples were fixed at 0.3 at.% (0.5 wt.%). The Mg−0.3Ca binary alloy is used as a control alloy to compare the Mg−*x*Zn−Ca ternary experimental alloys.

Table 2

Grain size and mechanical properties of Mg−4.0Zn−0.2Ca alloys [44].

Alloys	Grain Size (μm)	Yield strength (MPa)	Ultimate tensile strength (MPa)	Ductility (%)
As-cast	100−130	60±1.5	185±15	12.5±1.5
Extruded	3−7	240±5	297±5	21.3±3.0
After immersion	3−7	160±10	220±15	8.3±1.5

Ohishi *et al.* [46] concluded that the higher addition of Zn leads to completely different precipitation reaction having three types of precipitates; rod-shaped β_1'-$MgZn_2$ phase along the *c*-axis of the Mg, fine plate-like $Ca_2Mg_6Zn_3$ phase on the basal planes with coherent strain contrast, and elongated basal plates along the $\langle 1\ 1\ \bar{2}\ 0\rangle$ and $\langle 1\ 0\ \bar{1}\ 0\rangle$ directions (Figure 4).

2.3.2.4 Rare Earth. The International Union of Pure and Applied Chemistry defines rare earth elements (REE) or rare earth metals (REM) as a collection of 17 chemical elements in the periodic table, specifically 15 elements in the lanthanide series along with yttrium (Y) and scandium (Sc) which is described in Figure 5.

Table 3

All compositions [46].

Designations	at.%			wt.%		
	Mg	Ca	Zn	Mg	Ca	Zn
Mg−0.3Ca	Bal.	0.3	−	Bal.	0.5	−
0.1Zn	Bal.	0.3	0.1	Bal.	0.5	0.3
0.3Zn	Bal.	0.3	0.3	Bal.	0.5	0.8
0.6Zn	Bal.	0.3	0.6	Bal.	0.5	1.6
1.0Zn	Bal.	0.3	1.0	Bal.	0.5	2.6
1.6Zn	Bal.	0.3	1.6	Bal.	0.5	4.2

Sc and Y are considered REEs because they tend to occur in the same ore deposits as the lanthanides elements and exhibit similar chemical properties [47]. They are referred to as ‘rare’ because it is not common to find them in commercially viable concentrations. REEs generally fall into one of two categories: light rare earth elements (LREE) and heavy rare earth elements (HREE). The definition of LREE and HREE are based on the electronic configuration of each rare earth element. The LREE are defined as lanthanum (La), with an atomic number of 57, through gadolinium (Gd), with an atomic number of 64. The HREE are defined as terbium (Tb), with an atomic number of 65, through lutetium (Lu) with an atomic number of 71, plus Y and Sc with atomic numbers of 39 and 21 respectively. All of the HREE are different from the LREE in that they have paired electrons. The LREE have no paired electrons, more specifically, increasing unpaired electrons from 0 to 7 [47, 48]. Additionally, there are two groups: rare elements with (a) high solid solubilities (Y, Gd, Tb, Dy, Ho, Er, Tm, Yb and Lu) and (b) limited solubility (Nd, La, Ce, Pr, Sm and Eu) [49].

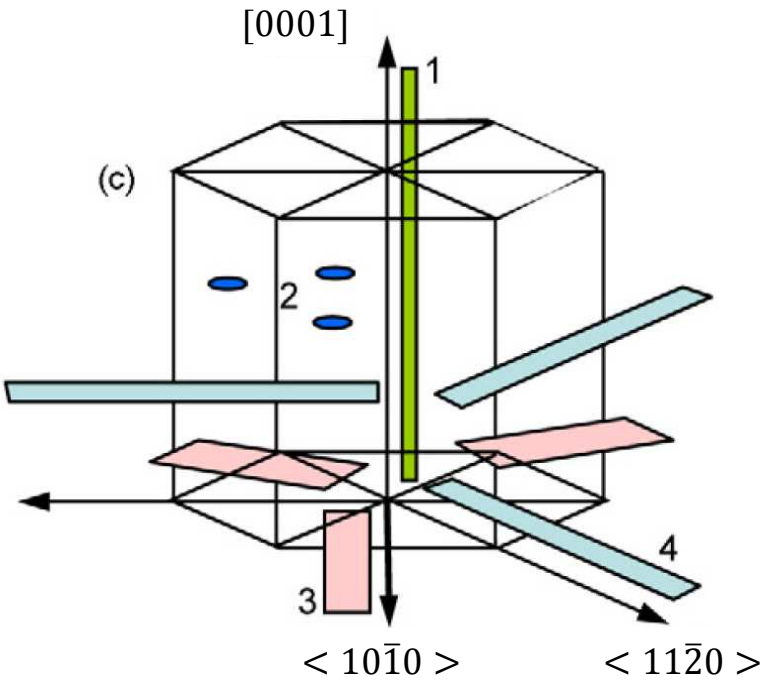

Figure 4. A schematic illustrating four different types of precipitates [46].

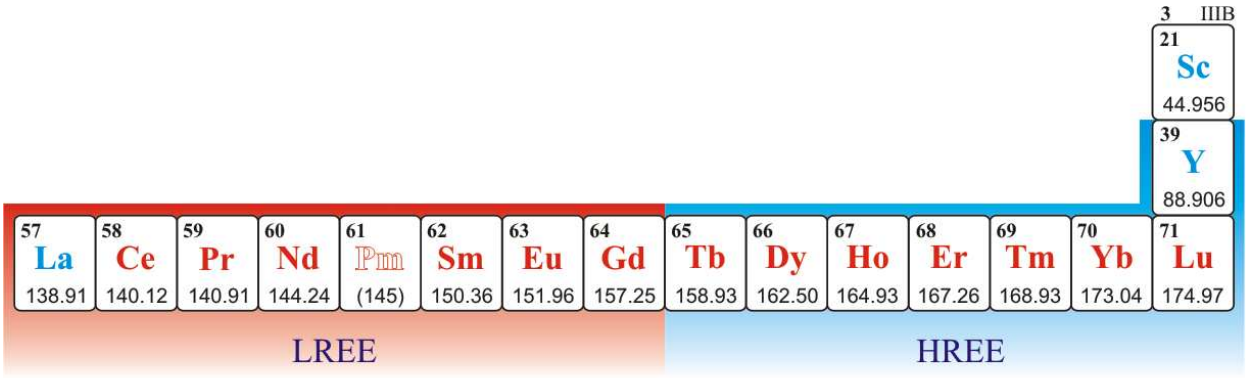

Figure 5. Rare earth elements (metals) are often subdivided into light rare earth elements (LREE) and heavy rare earth elements (HREE) [47].

Hort *et al.* [50] used Mg−2 wt.%Gd, Mg−5 wt.%Gd, Mg−10 wt.%Gd, and Mg−15 wt.%Gd alloys in their investigation. According to the Mg−Gd phase diagram (Figure 6), during solidification the concentration of Gd in the solid is in accordance with the concentration as the solidus line at a given temperature, and is in equilibrium with the concentration in the melt at the

liquidus line. The material solidifies completely at the eutectic temperature of 548°C. The solidified material cools slowly allowing the precipitation of Mg_5Gd which dictates that an amount of Mg_5Gd should exist in all experimental alloys. However, XRD measurements could not prove the presence of pure Gd, Mg_5Gd, or oxides in the Mg−2Gd, Mg−5Gd, and Mg−10Gd alloys, but the Mg_5Gd phase could be confirmed in the Mg−15Gd samples. In the as-cast Mg−Gd alloys, the grain size decreases with increasing Gd content illustrated in Figure 7. This effect is common in terms of the alloying element Gd contributing to grain refinement to some extent. The grains in all alloys, under all conditions are course. Hort *et al.* explains that the reason behind this phenomenon is a relatively slow cooling rate during casting due to the high melt temperature and mold temperature, and a 30 mm in thickness cast plate.

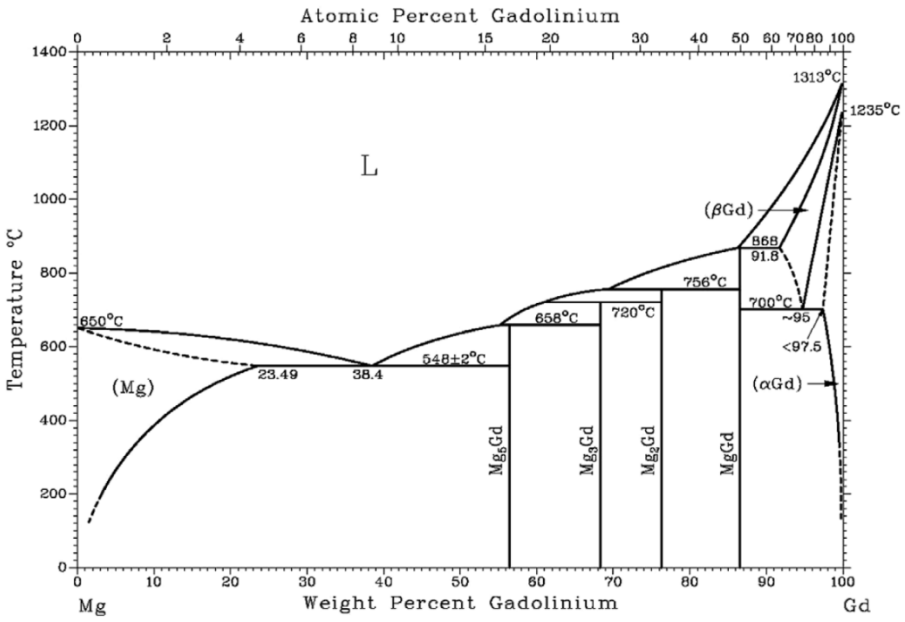

Figure 6. Mg−Gd phase diagram [50].

Most of the successful reports on *in vivo* application of Mg implants have investigated Mg alloys that contain REEs [49]. REEs in Mg alloying are predominantly used for strengthening and to improve corrosion resistance [51]. Some impurity elements in Mg, such as

iron, severely deteriorates its corrosion resistance, and REEs can cancel their influence by the formation of intermetallic compounds with the impurities [52]. Additionally, the corrosion resistance of Mg mainly contingent upon the surface oxide film, the incorporation of REEs in $Mg(OH)_2$ lattice is responsible for the improved corrosion behavior of Mg alloy.

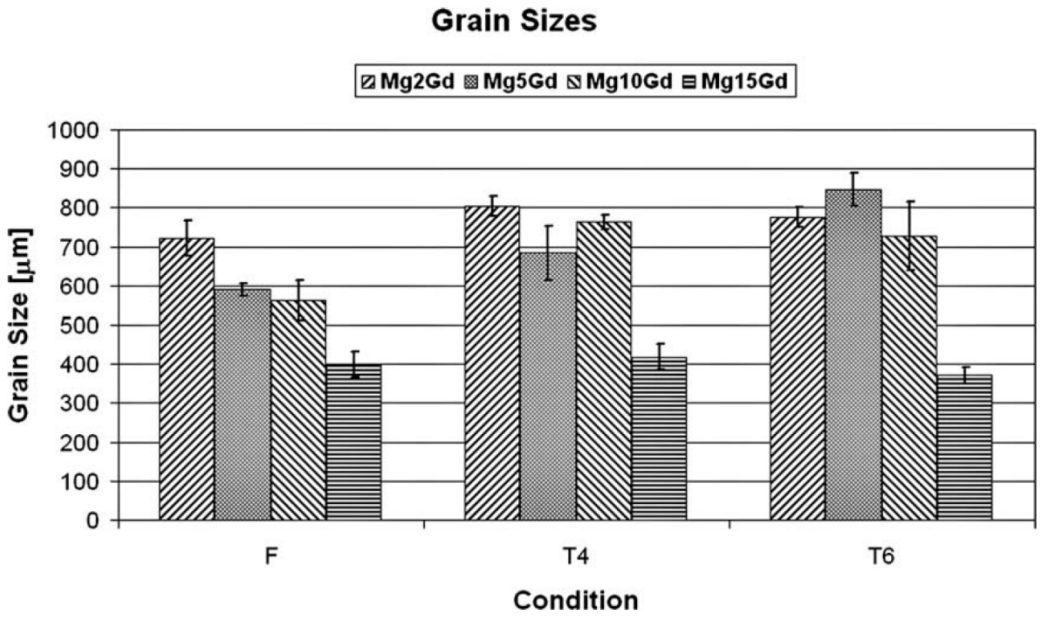

Figure 7. Grain sizes of the Mg−Gd alloys in the different heat-treated conditions [50].

2.4 Alloy Processing

2.4.1 Filtration. The filtration of molten metals through foam filters is a proven method in order to remove or reduce harmful inclusions which can decrease the melt fluidity and increase the possibility of gas porosity formation [53-55]. These defects that are produced by harmful inclusions reduce mechanical properties, corrosion resistance, and machinability of the metallic material [56]. During the filtration process, three stages occur. The first stage is the initial stage which is usually short compared to the next two stages. In this initial stage, the melt enters into some or all of the filter pores and consequently heats the filter if it is not already preheated [57]. The next stage is the normal filtration stage where the flow of molten metal

through the filter is found to be constant. The last stage is the filter blockage stage in which the molten metal flow decreases to near zero due to the formation of inclusions at the filter inlet and the cooling of the melt [57].

There are several types of filters presently in the market which include strainer cores, woven cloth or mesh, and ceramic filters. Pressed cellular, extruded cellular, and foam filters are categorized as ceramic filters. Metallic filtration of a nickel based super alloy using a Al_2O_3-based foam ceramic filter was found to be an effective means of controlling the level and particle size of inclusions [58]. This type of filter was able to separate coarse particles from the melt, intercept inclusions based on particle size, and entrap small blocky particles on the interior surface of the filter.

There have also been studies done on the use of metallic filtration of molten metal. Nazari *et al.* [57] used Al foam filters with 200 ppi pore size to filter molten Mg−Al−Zn alloy to study the effects on the mechanical properties compared to the non-filtered alloy. It was discovered that the utilization of Al filters resulted in a homogenized molten metal with smaller and less porosity. As a result the bending strength values of the samples with filtered Mg were higher than that of the samples that were not filtered. Wang *et al.* [59] utilized SS nets to determine the effects on the mechanical and corrosion property for Mg−Gd−Y−Zr alloys. The SS filtration was shown to not only remove the inclusions but also to better distribute finer inclusions within the alloy. The mechanical properties greatly improved and the corrosion rate decreased by the filtration treatment.

2.4.2 Heat treatment. Heat treatment is a metalworking process which includes a combination of heating and cooling operations applied to a metal or alloy in the solid state to obtain desired alloy properties [60]. For example, Zhou *et al.* [61] discovered that heat treatment

significantly changed the corrosion resistance of an AZ91D alloy in simulated body fluid. Compared to the as-cast condition, there was a reduction of the corrosion rate by 30-60%. Furthermore, the mechanical properties of Mg containing Al-silicon alloys can be enhance by heat treatment [21].

There are several techniques included under heat treatment processing. Solution heat treatment is a process that alters the microstructure within an alloy through dissolving all solute atoms to form a single-phase solid solution. This occurs as either a substitutional solution, where the new atoms occupy sites in the host crystal lattice, or as an interstitial solution, where the new atoms squeeze into “holes” between the atoms of the base lattice [62]. The amount of strengthening depends on the amount of dissolved solute and the size difference of the atoms involved. Since distortion of the host structure makes dislocation movement more difficult, the greater the size difference, the more effective the addition [62].

The solution heat treatment process is a technique in which an alloy is heated to a suitable temperature and held at this temperature for a sufficient length of time to allow a desired alloying element to enter into the solid solution. This is followed by rapid quenching or cooling in a suitable liquid to obtain certain material properties. Quenching prevents components that normally form the secondary phase through low temperature processing from occurring by trapping the secondary phase within the parent lattice which produces a supersaturated solid solution single phase [60, 62].

T4 heat treatment is the combination of solution heat treatment and natural aging. Aging describes a time-temperature dependent change in the properties of an alloy. As a result of aging, there is a precipitation from the solid solution of one or more alloying elements whose solubility decreases with decreasing temperature [60]. This technique works by adding atoms of one

element (alloying element) to the crystalline lattice of the base metal. The alloying element diffuses into the matrix forming a solid solution [63, 64]. T4 heat treatment is reasonably cheap and easy to perform and provides a microstructural modification resulting in improvements of mechanical properties [20, 23]. Liu *et al.* [65] found that T4 heat treatment has the ability to increase corrosion resistance in the Mg−3 wt.%Zn alloy.

Ohishi *et al.* [46] conducted additional heat treatment processing of the Mg−*x*Zn−0.3Ca alloys by solution treatment at 500°C for 2 h and then quench into water. Aging was done in an oil bath at 200°C. In terms of the age-hardening response of the Mg−*x*Zn−0.3Ca alloys investigated by Ohishi *et al.*, the Mg−0.3Ca binary sample exhibits little age-hardening where its hardness peak is 50 HV at ~30 h according to the 500g Vickers hardness test (Figure 8). Ohishi discovered that the peak hardness of the Mg−0.3Ca alloy can be increased with the addition of Zn, and the peak aging time becomes shorter. The peak hardness of the Mg−0.3Zn−0.3Ca and Mg−0.6Zn−0.3Ca samples are 66 and 69 HV which is achieved in ~2 h, respectively. As the Zn content increases beyond 0.6 at.%, the age-hardening response lowers. The peak hardness of the Mg−1.6Zn−0.3Ca sample is 62 HV at ~70 h, which is still higher than that of the binary alloy. It was concluded that the Mg−0.6Zn−0.3Ca alloy shows the best age-hardening response in the alloys investigated in this work. The ordered monolayer Guiner-Preston (G.P.) zones were formed during aging until the peak-aged condition suggesting an excellent thermal stability. The G.P. zone is the first stage of precipitation as the precipitates comes out of the solid solution and is usually accompanied by a change in properties of the solid solution. Ohishi observed that the G.P. zones were detected in the Mg−0.3Zn−0.3Ca and Mg−0.6Zn−0.3Ca alloys, but not in the Mg−1.6Zn−0.3Ca alloy. Ohishi ultimately concluded that the monolayer ordered G.P. zones contributed to the enhanced age-hardening response.

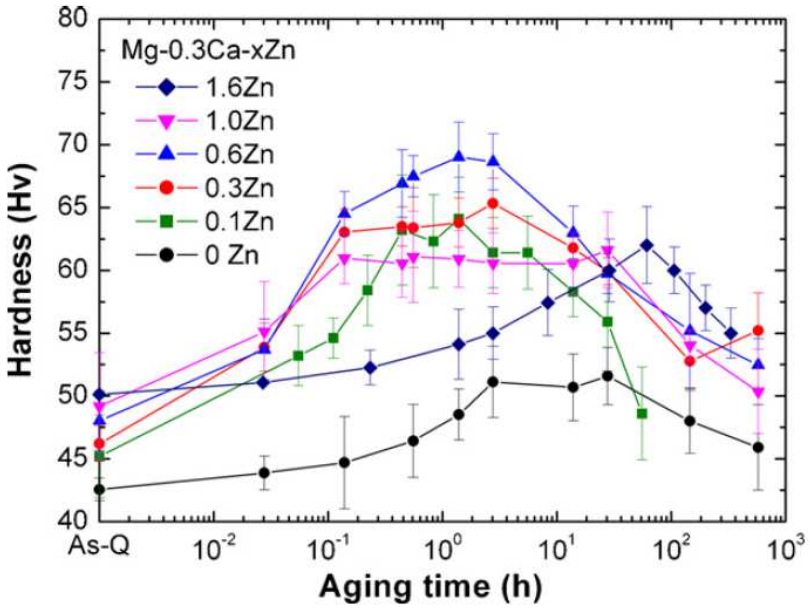

Figure 8. Age-hardening curves of Mg−0.3Ca with different Zn contents at 200°C [46].

Hort *et al.* [50] applied T4 treatment to the Mg−Gd alloys developed in their study. For the T4 treatment, a temperature of 525°C was chosen and the samples were annealed for 24 h. Specimens were water quenched immediately after heat treatment. T6 treatment was also conducted which include aging at 250°C for 6 h. The eutectic phase Mg_5Gd can be observed at the grain boundaries in all the as-cast samples. After T4 treatments most of these particles dissolve, though some still remain. The subsequent T6 treatment leads to the precipitation of very fine particles in all alloys except for the Mg−2.0 wt.%Gd sample. Selected area diffractions indicate that these fine precipitates are the metastable phases β', which is homogeneously distributed over the matrix, and β'', which can be observed in limited areas, after aging.

2.5 Mechanical Property Assessment

Assessing the mechanical properties of biomaterials is crucial in the development of orthopaedic biomaterials. Biomaterials designed for orthopaedic medical devices must be able to provide maintain the mechanical integrity of an injured site throughout the entire healing

process. Several studies on the mechanical capabilities of Mg alloys have been done. The mechanical properties of the as-cast Mg−*x*Ca system conducted by Li *et al.* [40] revealed that the yield strength, ultimate tensile strength and the elongation for the as-cast Mg−*x*Ca samples decreased with increasing Ca content (Figure 9). It can be seen that the as-cast Mg−*x*Ca samples have yield strengths and ultimate tensile strengths that are lower than the acceptable values (200−400 MPa) for biomedical applications [40]. Therefore there is a need for further alloying or processing techniques to modify the as-cast Mg−*x*Ca alloy to obtain the appropriate mechanical integrity.

Sun *et al.* [44] carried out tensile tests on the Mg−4.0Zn−0.2Ca alloy at a constant crosshead speed of 1.0 mm/min at room temperature. Table 2 summaries the grain size and mechanical properties of the Mg−4.0Zn−0.2Ca alloy produced this study. The alloying effect of Zn and Ca contributes to the modification of mechanical properties.

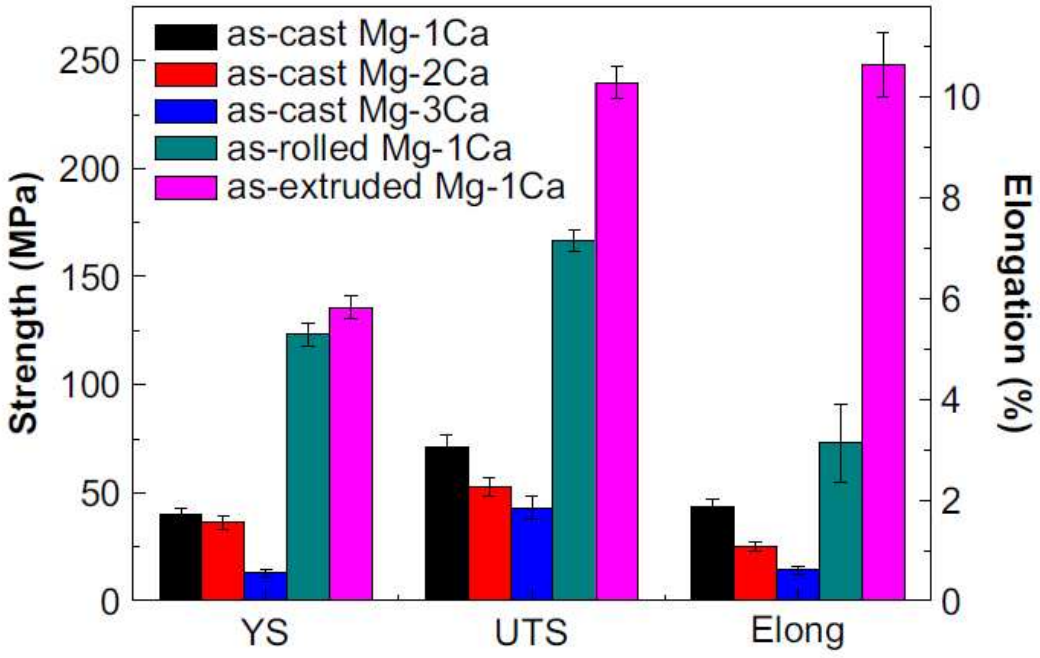

Figure 9. Tensile properties of as-cast Mg−Ca alloy samples at room temperature [40].

Zn was found to have a solution hardening effect on Mg and therefore the precipitation of $Ca_2Mg_6Zn_3$, and $Ca_2Mg_5Zn_{13}$ could enhance the strength and toughness of the alloy. The as-cast the Mg−4.0Zn−0.2Ca alloy mainly consists of α-Mg and particle phases. Sun explains that the stacking fault energy of Mg alloys decreased with high content of solid solution Zn. Consequently, the extended dislocations were broadened which resulted in higher difficulty in the initiation of non-basal slip. As a result, twin nucleation, which can be promoted by the precipitation of particles, becomes an important plastic deformation mode. Therefore, the as-cast Mg−4.0Zn−0.2Ca alloys had high ductility.

In terms of the effects of the REE on Mg, tension and compression studies, conducted by Hort *et al.* [50], were performed on the Mg−Gd alloy. From Figure 57 (Appendix), it can be seen that increasing the amount of Gd in Mg improves the ultimate tensile strength (UTS) as well as the tensile yield strength (TYS), while the elongation to fracture (El) is reduced. Hort concluded that the increase in TYS and UTS with increasing amounts of Gd is mainly attributed to the increase in Gd in solid solution in the α-matrix.

With respects to the heat treatment effects on the tensile properties, the solutionizing temperature (525°C) and time (24 h) allowed the precipitates of Mg_5Gd to dissolve during the T4 treatments. For the alloys with a Gd content of 10 wt.% or less, grain growth could be observed, and consequently both the dissolution of precipitates and the grain growth contributes to the loss in strength after the T4 treatments. In terms of the compression strengths, an increase in Gd leads to increases in the compressive yield strength (CYS) and the ultimate compressive strength (UCS) and a decrease in the deformation in compression. These results follow a similar trend to the results obtained in tension except that the absolute values are higher compared to the tensile results. It is clear to see that the alloying and heat treating processes are a key component in

developing Mg biomaterials that will be able to handle the mechanical requirements of an orthopaedic implantable medical device.

2.6 Corrosion Assessment

The degradation behavior is important characteristic of orthopaedic biomaterials because this can have an effect on the mechanical integrity and biocompatibility of the material. Biodegradable materials are designed to provide temporary support during the healing process of injured tissue and then degrade afterwards [66]. Thus, several studies have been conducted on Mg alloys to develop a biomaterial with suitable corrosion resistance for medical implant applications.

Li *et al.* [40] conducted an immersion degradation test on Mg−*x*Ca (*x* = 1−3 wt.%) samples in simulated body fluid (SBF) according to the ASTM-G31-72 standard. SEM micrographs (Figure 10) show the corrosion surface of Mg−*x*Ca samples immersed in SBF after 5 h.

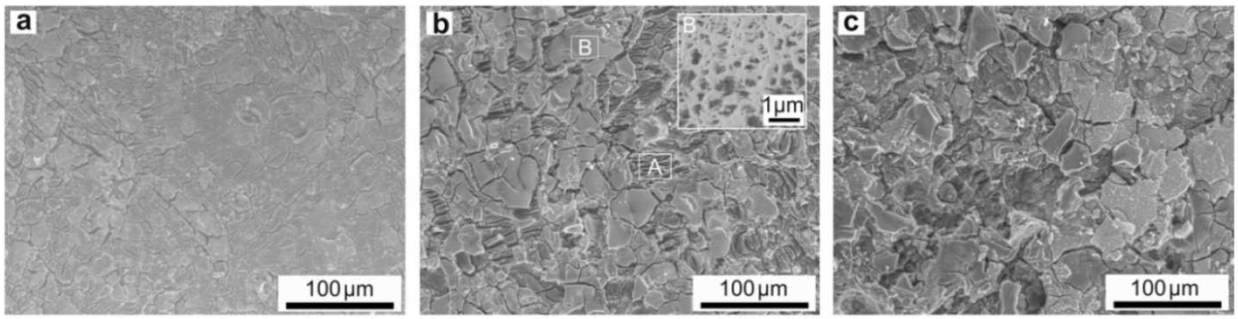

Figure 10. SEM micrographs of as-cast Mg−Ca alloys after immersion in SBF for 5 h: (a) as-cast Mg−1Ca alloy, (b) as-cast Mg−2Ca alloy, and (c) as-cast Mg−3Ca alloy [40].

As seen in Figure 10a, the Mg−1Ca sample maintained the integrity of the corrosion film. For the Mg−2Ca sample, some areas exhibited the peeled-off surface feature whereas other areas were still covered with integrated surface film. After a 250 h immersion time, the Mg−1Ca and

Mg−2Ca samples were found to be covered entirely with white precipitates and the square geometry of the samples were severely destroyed. For the Mg−3Ca sample, the plate degraded too fast and disintegrated into fragments after 24 h exposure.

In terms of electrochemical corrosion testing, according to the ASTM-G102-89 standard, the corrosion rates derived from the corrosion current densities for the as-cast Mg−1Ca, as-cast Mg−2Ca, and as-cast Mg−3Ca samples were calculated to be 12.56, 12.98, and 25.00 mm/year, respectively. A model of the alloy and aqueous solution interaction was created to describe the corrosion processes and the subsequent hydroxyapatite formation (Figure 11). Li explained that when the Mg−Ca alloy surface was exposed to the aqueous solution, the Mg_2Ca secondary phase acted as a cathode for hydrogen evolution because the potential of Mg_2Ca precipitate was more positive than that of the α-Mg matrix. The anodic dissolution of Mg occurred, and the Mg hydroxide film was expected to form on the surface of Mg−Ca alloy due to the significant alkalization near the surface. Since an increase in Mg_2Ca amount would lead to an increase in cathode-to-anode area, it could explain why the corrosion rate obtained from electrochemical tests increased with increasing Ca content. Li suggests that to meet the requirement of the harmonization between implant biodegradation and new bone formation, the addition of other elements and heat treatment processing could retard biocorrosion and improve corrosion resistance, respectively.

Sun *et al.* [44] conducted a 30-day immersion degradation test on the Mg−4.0Zn−0.2Ca alloy in c-SBF. The Mg−4.0Zn−0.2Ca samples degraded quickly, accompanied by the release of hydrogen and form of an insoluble corrosion layer during the early stage of the immersion test. After the formation of the corrosion layer, the degraded rate began to slow down as a result of the insoluble corrosion layer retarding the degradation.

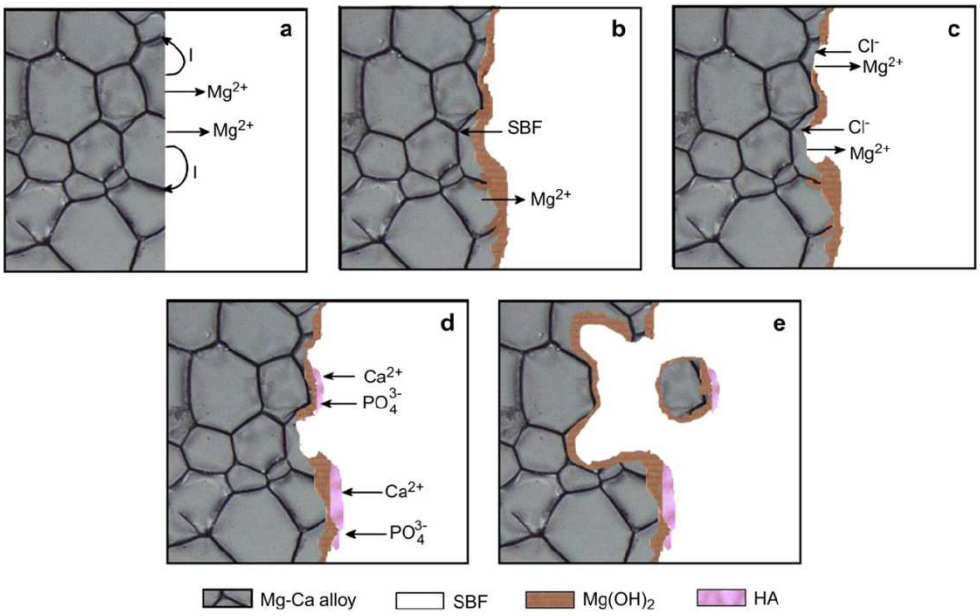

Figure 11. Schematic diagram of the alloy/solution biocorrosion interface: (a) the galvanic corrosion between Mg and Mg_2Ca phase, (b) the partially protective film covering the surface of Mg−Ca alloys, (c) the absorption of chloride ions to transform $Mg(OH)_2$ into $MgCl_2$, (d) the hydroxyapatite formation by consuming Ca^{2+} and PO_4^{3-}, and (e) the disintegrated particle-shape residues falling out of the bulk substrate [40].

The degradation rates, which were obtained according to the ASTM-G31-72 standard, after 30-day immersion are listed in Table 4. The degradation rates of the Mg−4.0Zn−0.2Ca samples were slower than the pure Mg (> 99.99%) control group. Sun explains that with the increasing time of immersion, more Mg^{2+}, Zn^{2+} and Ca^{2+} ions were dissolved into the SBF solution. As a result, an Mg-containing Ca phosphate precipitated from the SBF solution and deposited on the surface of the samples. Previous studies [67] conclude that this corrosion layer has the ability to promote osteo-inductivity and osteo-conductivity, predicting good biocompatibility and retarded degradation. Therefore the degradation of Mg−4.0Zn−0.2Ca in Sun *et al.* study is concluded to be harmless and to have good biocompatibility.

Table 4

Corrosion potential, corrosion current, and corrosion rate of Mg and Mg−4.0Zn−0.2Ca alloys [44].

Materials	*E* (V)	Current (A/cm^2)	*V* (mm/year)
Pure Mg	−1.906	3.715×10^{-4}	2.13
As-cast Mg−4.0Zn−0.2Ca	−1.70	2.67×10^{-4}	2.05
Extruded Mg−4.0Zn−0.2Ca	−1.677	2.43×10^{-4}	1.98

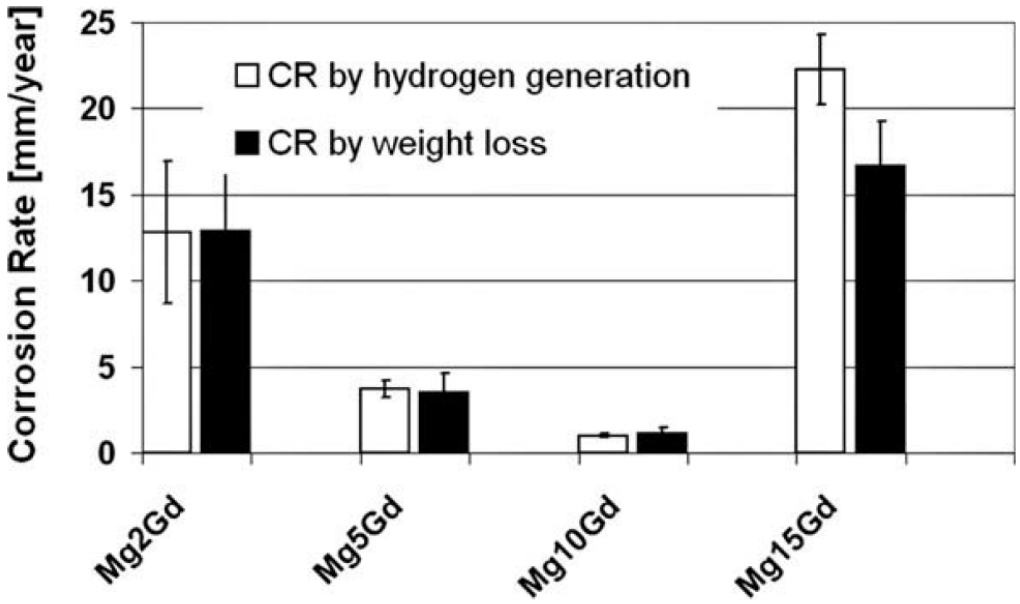

Figure 12. Corrosion rates determined by hydrogen generation and weight loss measurements [50].

The corrosion resistance of the Mg−RE alloys investigated by Hort *et al.* [50] was conducted through immersion tests in aerated 1% sodium chloride (NaCl) solution. The corrosion rates were determined by calculations based on the hydrogen formation and weight loss shown in Figure 12. It can be seen that with increasing Gd up to 10 wt.% for the as-cast

condition, the corrosion rate decreases. The Mg−15Gd values, which have a higher Gd amount, lead to a drastic increase in the corrosion rate. Hort explains that compared to the other binary alloys, the fraction of the grain boundaries is larger for the 15 wt.% Gd alloy. They also note that the Ni content in the Mg−15Gd was the highest observed.

2.7 Cytocompatibility Assessment

Several studies have been conducted on the cytocompatibility of Mg alloys. In the cytocompatibility studies presented by Li *et al.* [40], the Mg−1Ca alloy underwent cell viability examination. Figure 13 describes the cell viability of L-929 cells cultured in 100%, 50%, and 10% Mg−1Ca alloy extraction medium for 2, 4, and 7 days.

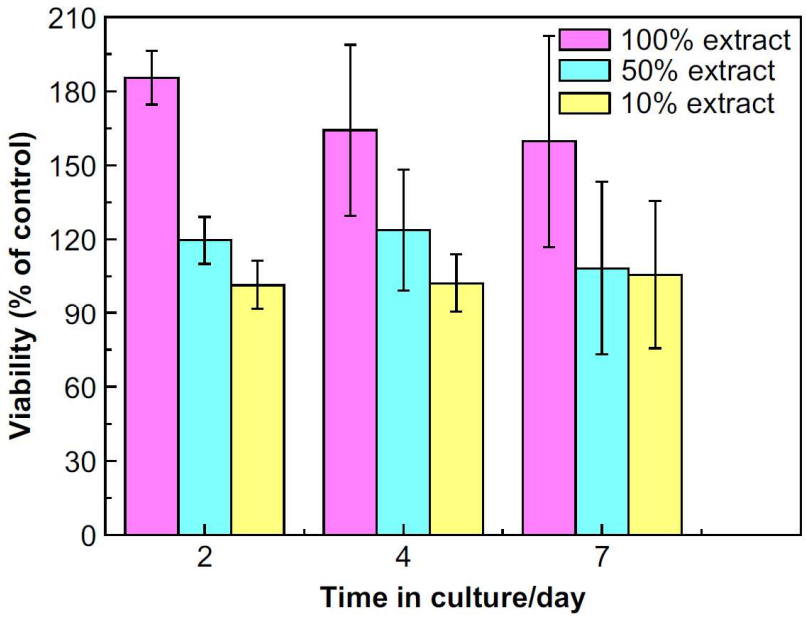

Figure 13. L-929 cell viability expressed as a percentage of the viability of cells in the control after 2, 4 and 7 days of culture in Mg−1Ca alloy extraction media with 100%, 50%, and 10% concentrations, respectively [40].

There was a significantly higher absorbance in the Mg−1Ca alloy extracts than that of the control. In addition, the cell viability was positively influenced by the extract concentration. Li

explains that the abundant Mg ions released into the culture medium by the corrosion of Mg−1Ca alloy might contribute to the increased cell viability. Mg ions were found to simulate the integrin-mediated osteoblast response by facilitating the interaction of integrins with their cognate ligands [40].

Sun *et al.* adopted L-929 cells to evaluate the cytocompatibility of Mg−4.0Zn−0.2Ca alloys as well. Cells were incubated with Mg−4.0Zn−0.2Ca extract for 1, 2, 4, and 7 days (Figure 14). Sun determined that the Mg−4.0Zn−0.2Ca alloy has a level of biosafety suitable for in cellular applications according to the ISO 10993-5: 1999 standard [68].

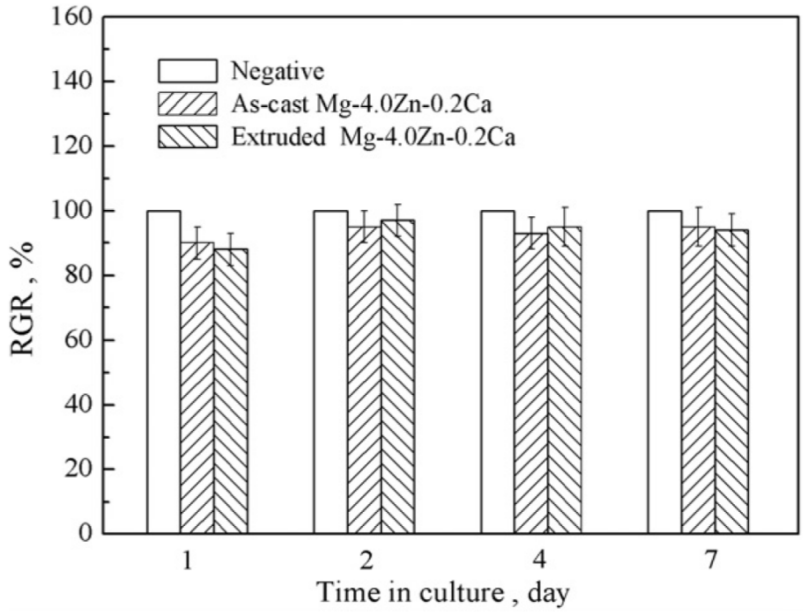

Figure 14. Cell viability cultured in 100% extraction medium for 1, 2, 4, and 7 days [44].

2.8 Commercial Patents

Xiaonong Zhang received a patent entitled, *Bio-absorbable Mg-Zn-Ca three-elements magnesium alloy material* in 2006 [69]. This invention deals with the development of an absorbable Mg−Zn−Ca ternary alloy system to be used for biomedical applications. The alloy system in this invention comprises of the following components by weight percentage: 1-8% Zn,

0.1-2% Ca, and a balance Mg. Zhang claims that for optimum mechanical property and biological corrosion performance, the ideal weight percentage for Zn and Ca are 6±0.5% and 0.5±0.1% respectively. For this composition, Zhang claims that the tensile strength (300 MPa) and ductility (8-10%) can guarantee excellent performance in medical applications. The Mg−Zn−Ca alloy in this invention consists of high purity raw materials and high cleanliness of smelting technology to manufacture. The purity of the raw material should not be less than 99.99% Mg, 99.999% Zn, and 99.75% Ca. Melting and casting procedures require the use of high purity argon inert gas, the use of special graphite or titanium melting crucible, and a melting temperature of about 750°C.

Additionally, the United States patent entitled *Implant with a base body of a biocorrodible magnesium alloy* by Bodo Gerold presents an invention that has improved corrosion behavior and mechanical properties for implants made of a biodegradable Mg alloy [70]. The Mg alloy claimed in this patent has the composition of:

- Gd: 2.7-15 wt.%
- Zn: 0-0.5 wt.%
- Zr: 0.2-1.0 wt.%
- Nd: 0-4.5 wt.%
- Y: 0-2.0 wt.%

Mg and the impurities due to the manufacturing process account for the remainder up to a total of 100 wt.%. The alloy can be produced and processed according to the procedures for manufacturing common Mg alloys. Gerold explains that the preferred amount of Gd is 7.0-13.0 wt.% to ensure the pharmacological effects of the Gd ions released on degradation of the

material in the body. The preferred Zn concentration is 0.1-0.5 wt.% and the preferred addition of Zr to improve the corrosion properties is 0.2-0.7 wt.%. The preferred Nd content of the alloy is 2.0-2.5 wt.% which can improve the mechanical properties. If the Nd content exceeds 4.5 wt.%, then the ductility of the alloy is worsened because of the limited solubility of Nd. The alloy in this invention is characterized in that complete or almost complete dissolution of all the precipitated intermetallic phases is achieved by heat treatment. Consequently, the required plastic deformability and desired mechanical properties of the material are preserved over the entire manufacturing process. The inventive alloy exhibits improved strength. For example the range between the onset of plastic deformation and reaching the tensile strength and/or compressive strength is optimized according to the uniform elongation. The elongation range is large and shows a uniform increase in the stress, strength and deformability required for further deformation. For stents, the patent claims that the material allows an improvement in the supporting force and the diameter of the struts in the stent can be kept small. Additionally, the alloy is claimed to have a reduced corrosion tendency in a physiological environment. In terms of *in vivo* degradation, the claim is that the alloy evidently also has a positive pharmacological effect on the surrounding tissue, according to preliminary experiments, in particular in the case of a stent used as intended. The preferred implant for the alloy claimed in this patent to be implemented is a stent.

CHAPTER 3

Experimental Methods and Concepts

In this chapter, the materials preparation, microstructure assessment, mechanical tests, corrosion test, and cytocompatibility assessment used for the experiments are described and discussed. The statistical analysis of all quantitative data produced by scientific experiments is also explained in this chapter.

3.1 Materials Preparation

3.1.1 Design strategy. Design strategy is one of the more critical steps to the success of creating a viable biomaterial. The two alloy systems selected to be studied for this research work were the magnesium-zinc-calcium system and the magnesium-zinc-calcium-rare earth system based on their intriguing alloying characteristics (Table 5) which was discussed in more detail in Chapter 2.

Table 5

Elements alloyed with the based magnesium and reasoning behind the usage of these alloys in this research project.

Name	Elements	Attractive Characteristics
MgZnCa	Zinc	Elevates corrosion potential and improves corrosion resistance; improves hardening capabilities; refinement of precipitates
	Calcium	Major component in human bone and can accelerate bone growth; grain refinement and creep resistance
MgZnCa-RE	Rare Earth	High strength and ductility; improve mechanical properties; corrosion and creep resistance
	Zirconium	Grain refinement; increase strength

3.1.1.1 Magnesium-zinc-calcium system. The effects of Zn content on the as-cast Mg−Ca system was investigated in this study. The Zn concentrations started at 0.5 wt.% and

were increased systematically to 10.0 wt.% and are designated as M-46 to M-53, respectively (Table 6). All samples of the Mg−*x*Zn−Ca system were produced with the Ca concentration of 0.3 wt.%. Ca has low solubility in magnesium which come to only 0.2 wt.% at room temperature and 1.2 wt.% at high temperature in the equilibrium state and consequently is maintained at a lower level [71].

3.1.1.2 Magnesium-zinc-calcium-rare earth system. All samples of the MgZnCa−RE system were produced with 1.0 wt.% Zn, 0.3 wt.% Ca, and 1.3 wt.% rare earth alloys.

3.1.2 Alloy processing. The innovative aspect of this research was based on the alloy processing which dictates the uniqueness of each alloy. The processing, characterization, and screening of each alloy was done with the following fundamental questions in mind [72]:

1. What are the most critical steps during Mg processing and/or Mg implant production to imprint harmful impurities into the Mg material?
2. What are the most important parameters that are mandatory to be included in a bench test (materials screening test) to determine whether a biodegradable Mg material is suitable as a biomaterial?
3. What are the most relevant environmental factors to replicate in a bench method to ensure that the intermediate and ultimate byproducts are consistent with those generated throughout *in vivo* use?

3.1.2.1 Melting and casting. All alloys fabricated in this study were produced through common metal casting techniques. Melting and alloying operations were performed in a low carbon steel crucible in an inert UHP grade argon environment, which prevents the oxidation reactions of molten Mg. High purity Mg (99.97%) was heated at 710°C for 10 minutes or until the slug was completely melted.

Table 6

Nominal composition of as-cast Mg−xZn−Ca system in weight percentage and the Mg concentration is in balance.

Alloy Name	Elemental composition (wt.%)	
	Zn	Ca
M-46	0.50	0.30
M-47	1.00	0.30
M-48	2.00	0.30
M-49	3.00	0.30
M-50	4.00	0.30
M-51	5.00	0.30
M-52	6.00	0.30
M-53	10.00	0.30

Each alloying element was then added separately and kept for 10 minutes before adding an additional alloy to ensure all alloying elements were completely dissolved into the melt. Automated stirring was applied for 15 minutes to help provide a homogeneous distribution of elements throughout the melt. The melt was then raised to 730°C (Mg−*x*Zn−0.3Ca alloys) or 750°C (MgZnCa−RE alloys) for 15 minutes and then poured into a steel book mold.

3.1.2.2 Heat treatment. Levi *et al.* [73] discovered that at 465°C for the Mg-1.6 wt.% Ca-3.2 wt.% Zn alloy, more than 2% of the microstructure at equilibrium is liquid. In order to prevent or minimize the grain boundary melting, Levi followed a four-step heating procedure which consisted of: (1) holding at 300°C for 48 h; (2) quasi-stationary heating (1°C/h) to the holding temperature; (3) holding at 465°C for 96 h; followed by (4) water quenching.

Therefore, a double stage heat treatment process was implemented for this study in an effort to prevent the melting of the grain boundary during the solution treatment process. To

optimize this double stage solution treatment process for the Mg−*x*Zn−0.3Ca alloys, several different time and temperature parameters were explored for this study.

The first stage of the T4 solution heat treatment process was conducted at a low temperature (300°C or 320°C) for a specific amount of time (20−48 hours). The second stage includes additional solution treatment at a higher temperature (400−480°C) for a specific amount of time (2−144 hours). Quenching was done in hydraulic oil. The temperature of the first stage was chosen based on the structural studies on the Mg−4.0Zn−0.4Ca alloys conducted by Hradilová *et al.* [74]. From the results of their differential scanning calorimetry (DSC), the DSC curves indicated that there were two endothermal peaks at 340°C and 390°C for the as-cast alloy which was determined to be the presence of the α-Mg+MgZn eutectic phase at 340°C and the $Ca_2Mg_6Zn_3$ phase at 390°C. For the T4 heat treated Mg−4Zn−0.4Ca alloy, the DSC curve indicated that the 340°C peak found in the as-cast curve was suppressed by the T4 treatment. However, the peak at 390°C which indicates the presence of the $Ca_2Mg_6Zn_3$ phase remained unchanged. As a result, the temperature of the first stage in the solution treatment process in this study was held under 340°C. According to the binary phase diagram of Mg−Zn, the solidus line is at about 510ºC. Therefore, at 480ºC, the alloy should not start to melt. Nevertheless, if the alloy was directly heated to 480ºC at a quick ramp rate, the secondary phase preferably at the grain boundaries would melt, which would lead to heat treatment defects. To avoid this phenomenon, a slow ramp rate of 1°C/min was used to reach the treatment temperature in the first stage and a ramp rate of 0.1°C/min was used for the second stage. This allowed part of the secondary phase to dissolve into the Mg-matrix in solid phase.

The MgZnCa−RE alloys were also introduced to heat treatment processing. Hort *et al.* determined that introducing T4 treatment at 525°C for 24 h to the Mg−Gd system was effective

in dissolving eutectic particles into the primary matrix. Consequently, a double stage T4 treatment process was conducted in which the first stage consisted of a temperature of 400°C for 20 h and then an additional treatment of the second stage at 500°C for 2, 4, 6, and 8 h. The double stage treatment was done with the same ramp rates as described above.

3.2 Microstructure Assessment

3.2.1 Polishing and etching. Careful and meticulous surface preparation must be made to reveal the important details of a microstructure. The specimen must first be polished to a smooth and mirror-like finish [64]. Polishing is often used to enhance the look of a component, prevent contamination of instruments, remove oxidation, or prevent corrosion in pipes. For this study, in order to observe the grain structure of the samples, a metal polishing technique was applied. All samples were polished initially using a 600 grit silicon carbide polishing paper. Each subsequent polishing stage used a finer grit paper which included 800, 1000, and 1200 grit silicon carbide polishing paper. Additional polishing was performed using 3 µm, 1 µm and 0.05 µm diamond suspension solution until a mirror finish was achieved.

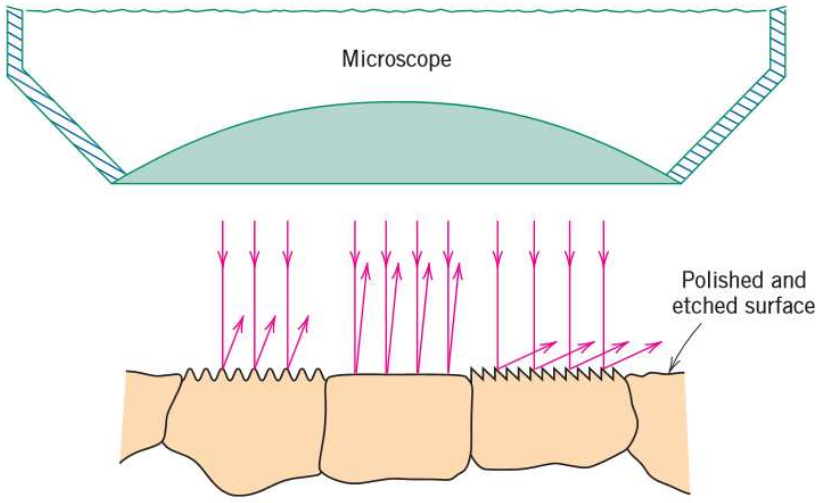

Figure 15. Schematic of a section view of grains showing how the etching characteristics and resulting surface texture can vary from grain to grain [64].

After polishing, etching was introduced to each sample. Chemical etching is the process of revealing microstructural details that would not be evident on an as-polished sample. The etchant corrodes the microstructural features making it more concise and clear to define. The chemical reactivity of the grains of some single-phase materials depends on crystallographic orientation. Consequently, in a polycrystalline specimen, etching characteristics vary from grain to grain. Figure 15 illustrates how normally incident light is reflected by three etched surface grains, each having a different orientation. The surface structure of an alloy as it might appear when viewed with the microscope; the luster or texture of each grain depends on its reflectance properties [64]. All samples were etched with a 5% nital solution. Additional etching was performed with picric acid solution on certain samples to achieve better grain contrast.

3.2.2 Grain size evaluation. The Heyn Lineal Intercept procedure was used to estimate the average grain sizes of all alloys [75]. After polishing and etching, images of the microstructure of each sample were taken using the Zeiss Axio Imager 2 optical microscope. Optical microscopy (OM) is a type of microscope that uses light and a system of lenses to magnify images of samples. Fifteen identical in length test lines were used for each alloy. The number of intercepts within each test line is counted at a 5x magnification. An intercept is a segment of test line overlaying one grain. Since a 5x magnification was used, the intercept numbers and the lineal length of each test line were converted based on a 1x magnification using the equations below:

$$N_i = N_{i0}\left(\frac{M}{M_b}\right) \qquad \text{Equation 1}$$

N_i is the number of intercepts within a test line; N_{i0} is the number of grains intercepted by the test line at magnification M_b which is the basic magnification at 1x. M is the observed magnification.

$$L = L_0\left(\frac{M_b}{M}\right) \qquad \text{Equation 2}$$

L is the length of the test line and L_0 is the test line at magnification M_b. When counting intercepts, segments at the end and the beginning of a test line which infiltrate into a grain were counted as half intercepts. The number of intercepts per unit length of each individual test line (N_L) was calculated using,

$$N_L = \frac{N_i}{L} \qquad \text{Equation 3}$$

The average N_L for each sample was then calculated. The ASTM grain size number (G) was subsequently determined using,

$$G = -3.2877 + 6.6439 \log_{10} N_L \qquad \text{Equation 4}$$

The average grain diameter is then ascertained from the ASTM grain size number utilizing the "Grain Size Relationships Computed for Uniform, Randomly Oriented, Equiaxed Grains" information found in the ASTM standard E 112-10 [75].

3.2.3 Elemental mapping and spectroscopy. Elemental mapping at the microstructure level by scanning electron microscopy (SEM) with energy dispersive X-ray spectrometry (EDS) has been widely applied in science and engineering. Combining the EDS system with the SEM allows the identification of compositional gradients at grain boundaries, second phases, impurities, inclusions, and small amounts of material. In the scanning mode, the SEM-EDS can be used to produce maps of element location, concentration, and distribution. Figure 16 depicts a schematic of a typical scanning electron microscope. Generally, the quality and resolution of SEM images are a function of three major parameters: instrument performance, selection of imaging parameters, and the nature of the specimen [76]. The main components of a traditional SEM are electron column, scanning system, detectors, display, vacuum system, and electronic controls. The electron column of the SEM consists of an electron gun and two or more electromagnetic lenses operating in vacuum.

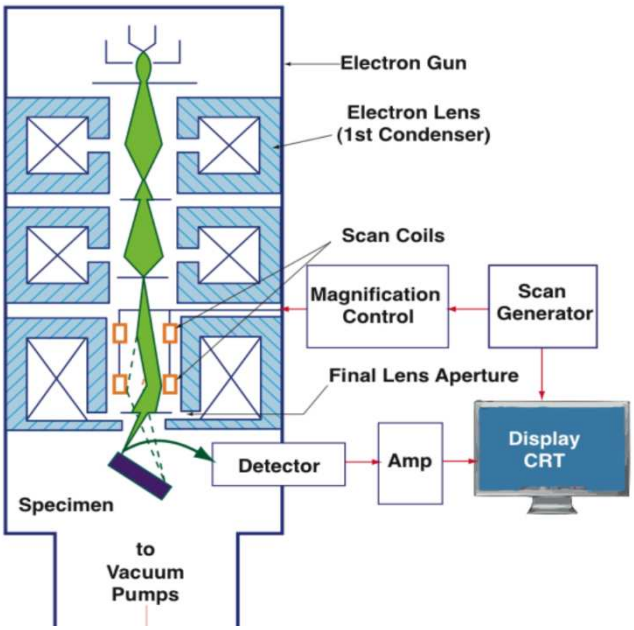

Figure 16. Schematic of a conventional scanning electron microscope [76].

The electron gun generates and accelerates free electrons to energies in the range of 0.2 keV to 40 keV, which are focused or condensed by the electron lenses to create a small stable electron beam on the specimen [76, 77]. Most SEMs, with the help of the scanning coils, can create an electron beam at the specimen surface with a size less than 10 nm in diameter while still carrying a sufficient current to form an acceptable image. Each point on the specimen that is struck by the accelerated electrons emits a radiated electromagnetic signal. Selected portions of this radiation, usually secondary (SE) and/or backscattered electrons (BSE), are collected by a detector and the resulting signal is amplified and displayed on the computer monitor [76]. The interaction of an electron beam with the surface of a specimen and the size and characteristics of that interaction volume is important for both the physical foundation for imaging and the chemical or X-ray analysis of the sample. The interaction of an electron with a specimen provides a wide variety of signals that can provide a signature of the specimen, specifically information on its structure and chemical composition [78]. The schematic representation of the

various signals generated as a result of electron beam interaction with a specimen is shown in Figure 17.

The EDS system utilizes the X-ray spectrum emitted by a specimen that is bombarded with the electron beam to obtain a localized chemical analysis. All elements from Beryllium (atomic number 4) to Uranium (atomic number 92) can be detected in principle [79]. Qualitative analysis involves the identification of the lines in the spectrum and is fairly straightforward owing to the simplicity of X-ray spectra. Quantitative analysis or the determination of the concentrations of the elements present entails measuring line intensities for each element in the sample and for the same elements in calibration standards of known compositions [79].

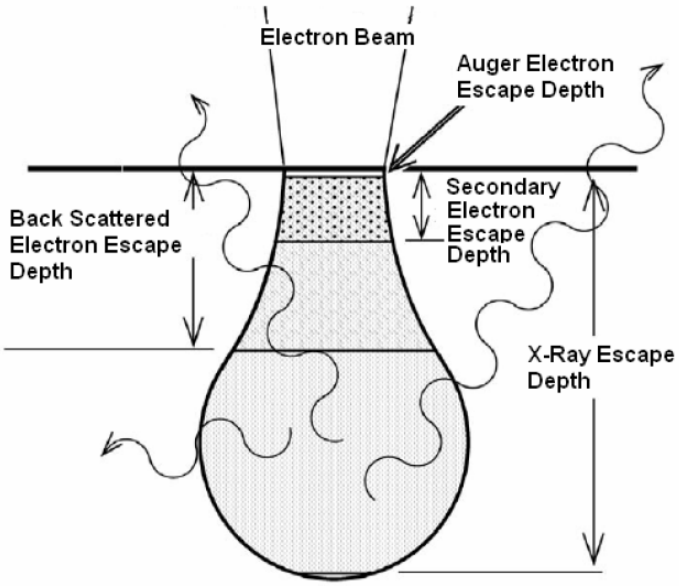

Figure 17. Schematic drawing of the tear-drop model of the electron interaction volume and the volume/depth from which the different signals originate [77].

The Hitachi® SEM SU800 was used to capture high quality images of mapping areas. Elemental compositions of the primary and secondary phases of the grain structures were

mapped using the attached EDS mapping feature. Almost all EDS mapping was conducted using a working distance of 15.5 mm, and a voltage and current of10kV and 20µA respectively.

3.3 Mechanical Tests

Ascertaining the mechanical properties of fabricated materials is critical to alloy developers, as well as to medical device designers. The objective of this testing was to characterize the compressive and tensile behavior (Figure 18) at static conditions for the series of magnesium alloys produced for this study to assess the mechanical integrity for each formulation. When forces that are applied to a material are constant they are said to be static. Material characteristics and mechanical strength were quantified and assessed for the potential use as biomaterials in medical devices. All mechanical testing conducting on the Mg-based alloys in this study were either outsourced to Orthokinetics Testing Technologies LLC, an ISO 17025 certified, A2LA accredited test facility or done in-house in accordance with ASTM E9-09, “Standard Test Methods of Compression Testing of Metallic Materials at Room Temperature" [80] and ASTM E8/E8M-11 “Standard Test Methods for Tension Testing of Metallic Materials” [81] at North Carolina A&T State University Mechanical Testing Facility.

3.3.1 Compression testing. The properties of a material are determined from the dimensions of the sample and the stress-strain diagram produced by the compression test. Samples dedicated for the compression tests were cut into cylinders with dimensions of 10 mm in diameter and 20 mm in height (Figure 19a). In static compression testing, the actuator of the MTS electro-mechanical test machine was connected to the superior compression fixture which held a stainless steel adaptor plate to the load cell. The test apparatus was assembled such that the Z-axis of the device was collinear with the axis of the actuator and load cell of the testing machine.

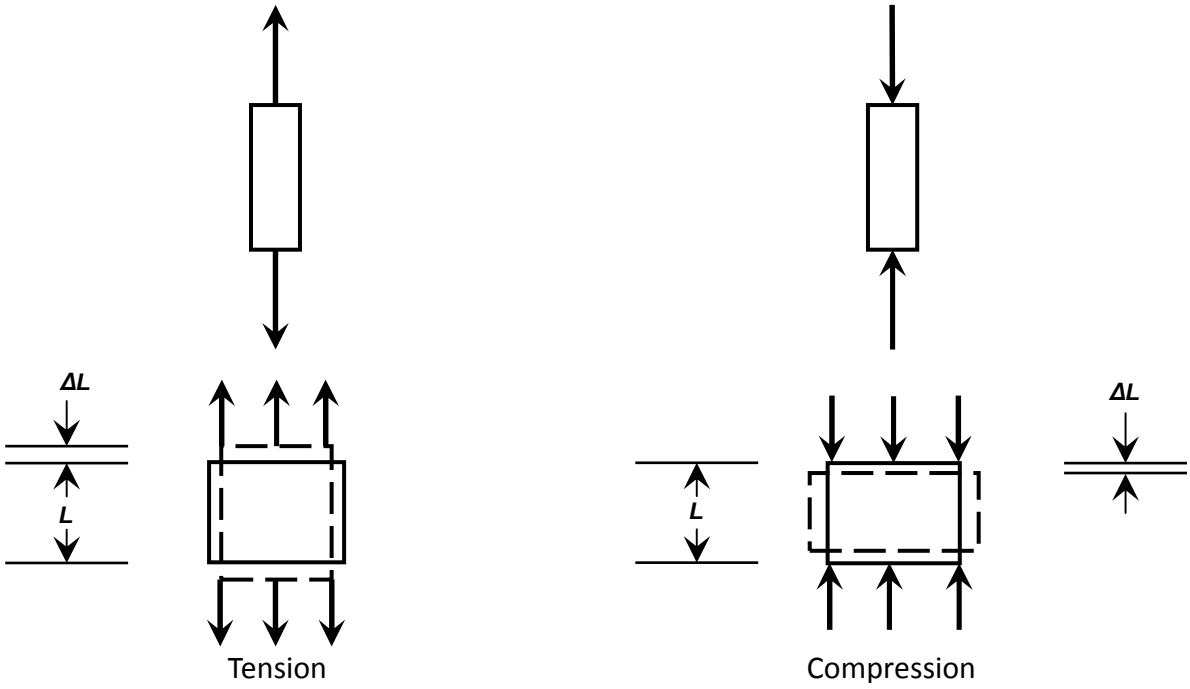

Figure 18. Examples of tension and compression loading and their shear response [62].

When loaded, the actuator applied a resultant force to the specimen directed along the longitudinal axis, which was aligned along the center of the circular cross-section plane of the test specimen. After each compressive failure test, the test fixture was inspected to ensure the test platen and components were not compromised or adversely affected by the previous test.

A compressive load was applied to each specimen mounted to the test machine at a rate of 2.0 mm/minute under displacement control until a failure was achieved. The test was stopped after the onset of a failure mode, where a failure was defined as plastic deformation that rendered the device ineffective or unable to adequately resist load, or permanent deformation resulting from fracture. Such failure was designated as a reduction in the compressive force, or when the superior and inferior fixtures made contact. All testing was conducted in ambient air at room temperature. Load and displacement data were recorded throughout the test at a relevant sampling rate. A laser extensometer was used to accurately track specimen deformation at

precise markings on the test samples, as mechanical losses in the test system (crosshead and fixtures) made crosshead displacements inconsistent. Figure 19b is a representative setup configuration photo of the static compression test apparatus.

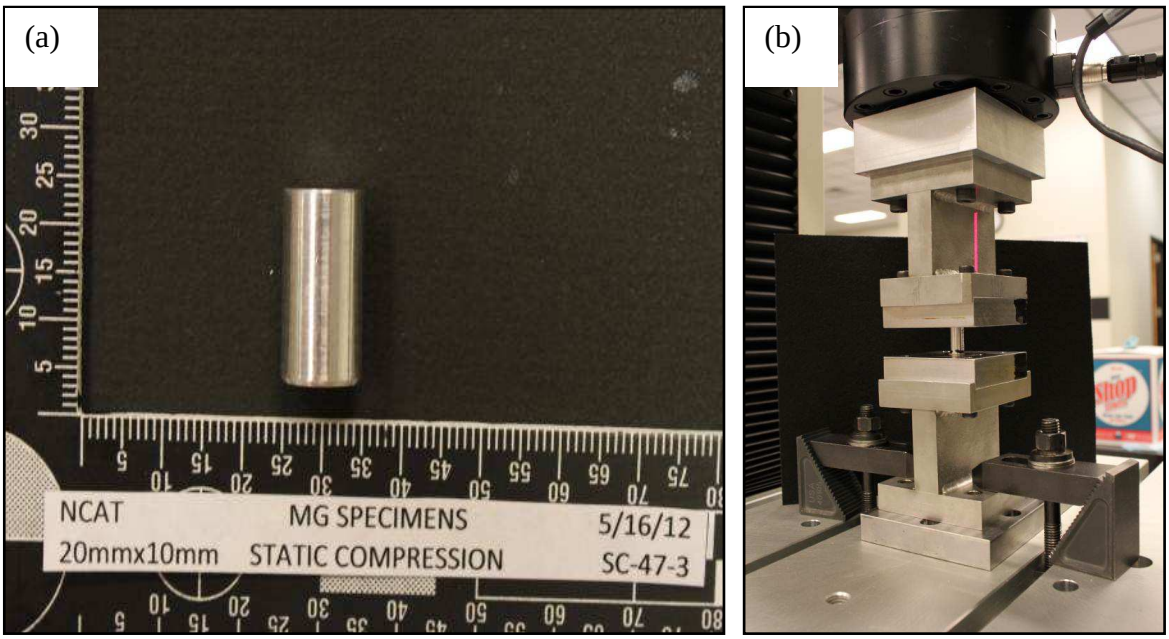

Figure 19. (a) Compression test sample and (b) static compression apparatus.

3.3.1.1 Modulus of elasticity. The modulus of elasticity is a material property that quantifiably describes the tendency of a material to deform elastically when a stress is applied to it. A uniaxial force is applied to the test specimen and the stress and strain were measured. The engineering stress (σ) is determined by dividing the indicated force by the sample's original cross-sectional area (Equation 5). The engineering strain (□) is defined as the difference between the instantaneous length and the original length divide by the original (Equation 6). By convention, a compressive force is taken to be negative, which yields a negative stress. Furthermore, since l_o is greater than l_i, compressive strains computed from equation 13 are also negative.

$$\sigma = \frac{F}{A_o} \qquad \text{Equation 5}$$

$$\epsilon = \frac{l_i - l_o}{l_o} = \frac{\Delta l}{l_o}$$ Equation 6

The appropriate slope is then calculated from the stress-strain curve (Figure 20) which is derived from the test data [82]. For most metals, the strain is proportional to the applied stress which is known as Hooke's law (Equation 7), and the constant of proportionality *E* is the modulus of elasticity.

$$\sigma = E\epsilon$$ Equation 7

For this study, after the test data was imported into the processing software, the engineering strain is set up as the *x*-axis (%) and the engineering strain is set up as the *y*-axis (MPa). Once the stress-strain curve was constructed from the test data, the initial linear portion of the curve is isolated and a linear line was fitted to the curve. The slope from the equation derived from said linear line is determined which is the elastic modulus of the alloy.

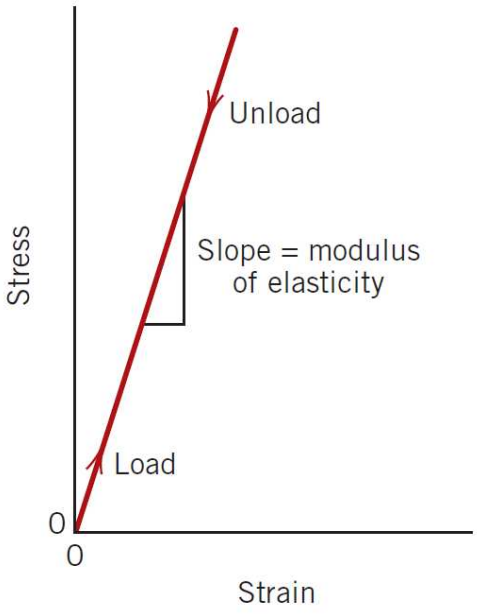

Figure 20. Schematic stress-strain diagram showing linear elastic deformation for loading and unloading cycles [64].

3.3.1.2 Yield strength. In materials development, the design for the application of a material usually ensures that only elastic deformation will result when a stress is applied. Consequently, it is important to know the stress at which plastic deformation or yielding occurs. For metals that experience this gradual elastic-plastic transition, the point of yielding may be determined as the initial departure from linearity of the stress-strain curve; this is sometimes called the proportional limit [64]. In most cases the position of this point may not be able to be determined precisely, therefore the offset method is applied. The offset method is where a straight line is constructed parallel to the elastic portion of the stress-strain curve at a specified value (conventional offset is 0.002.) [64, 80]. The yield strength is defined as the stress corresponding to the intersection of this parallel line and the stress-strain curve as it bends over in the plastic region (Figure 21). The line mn is constructed parallel to OA, and is positioned at a layoff position Om equal to the specified value of offset. Thus the intersection r between mn and the stress-strain curve is the yield strength for the specified offset [80].

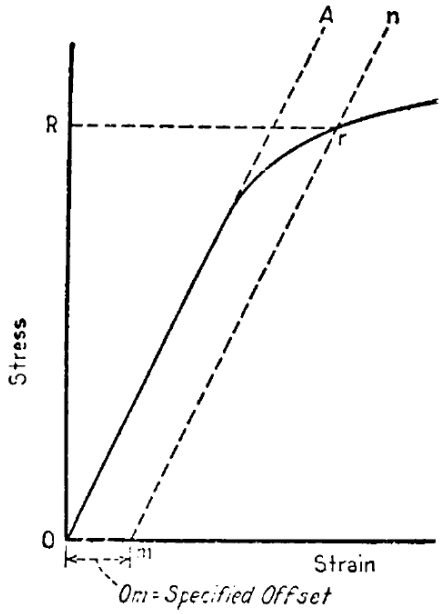

Figure 21. Stress-strain diagram for the determination of yield strength by the offset method.

3.3.1.3 Ultimate strengths. For materials that fail in compression, the ultimate compressive strength (UCS) and ultimate tensile strength (UTS) is the maximum stress that a material can withstand before fracture on the stress-strain curve [80]. It is determined by dividing the maximum load in compression (or tension) by the original cross-sectional area of the test specimen. The ultimate strength is a key value for design of structure purposes.

3.3.2 Tensile testing. The most common of the static tests is the uniaxial tensile test, which provides information about a variety of properties [62]. When a material is subjected to tensile loading, the relationships between stress and strain are similar to those for a compressive testing. Up to a certain value of stress, the material behaves elastically. Beyond this value, plastic flow occurs. Static tension testing was performed on standard tensile test samples (Figure 22a). The actuator of the electro-mechanical test machine was connected to calibrated high force MTS wedge style tension gripping fixtures. Each test sample was inserted into the fixtures and clamped securely. When loaded, the actuator applied a resultant force to the specimen directed along the long axis and located at the center of the cross section of the specimen. The test apparatus was assembled such that the *z*-axis of the device was collinear with the axis of the actuator and load cell of the testing machine. After each tensile failure test, the test fixture was inspected to ensure the grips and clamps were not compromised or adversely affected by the previous test.

A tensile load was applied to each specimen loaded in the test machine at a rate of 1.3 mm/minute under displacement control until a failure was achieved. The test was stopped after the onset of a failure mode, where a failure was defined as plastic deformation that rendered the device ineffective or unable to adequately resist load, or permanent deformation resulting from fracture. Such failure was designated as a sudden reduction in the tensile force, or when the

specimen fractured and separated. Load and displacement data were recorded throughout the test at a relevant sampling rate. A laser extensometer was used to accurately track specimen deformation at precise markings on the test samples, as mechanical losses in the test system (crosshead and fixtures) made crosshead displacements inconsistent.

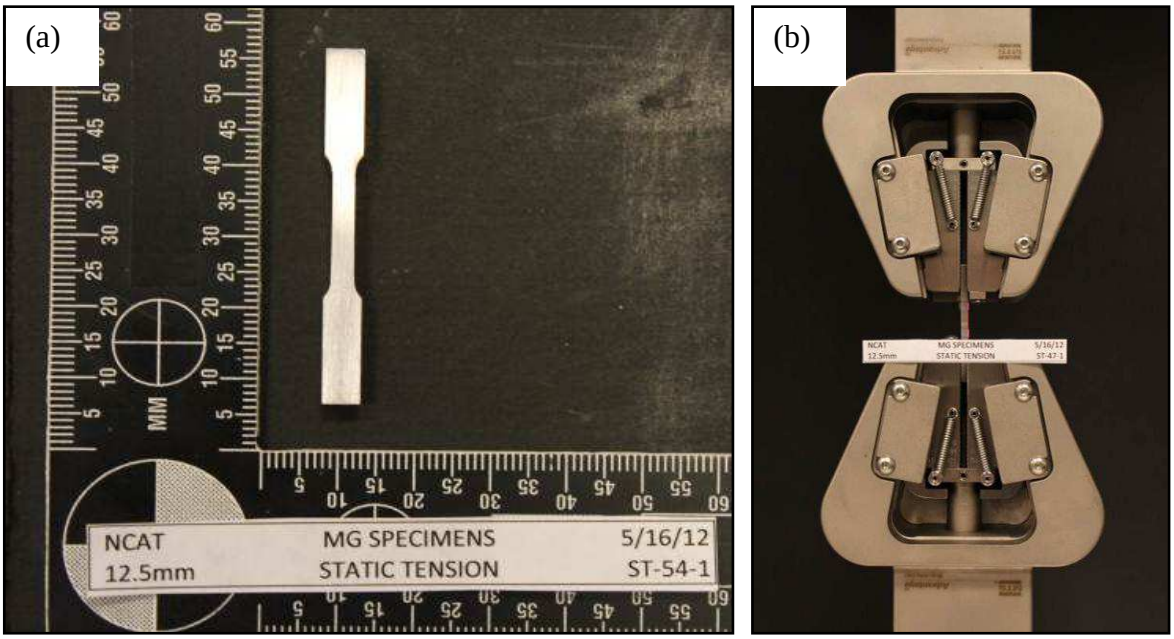

Figure 22. (a) Tensile test sample and (b) static tension apparatus.

All testing was conducted in ambient air at room temperature. Figure 22b is a representative setup configuration photo of the static tension test apparatus. The samples for tensile tests are reduced ASTM flat shape (Figure 23) of 3 mm x 3 mm in cross section and 12.5 mm in gauge length (Figure 22a). A tensile load was applied to each specimen loaded in the test machine at a rate of 1.3 mm/minute under displacement control until a failure was achieved. The test was stopped after the onset of a failure mode, where a failure was defined as plastic deformation that rendered the device ineffective or unable to adequately resist load, or permanent deformation resulting from fracture. Such failure was designated as a `sudden reduction in the tensile force, or when the specimen fractured and separated.

3.3.2.1 Elongation. Ductility, which is the degree of plastic deformation that has been sustained at fracture, is another important mechanical property that can be determined from a tensile test (Figure 24). Ductility can be expressed quantitatively as percent elongation [64]. The percent elongation (%ΔL) is the percentage of plastic strain at fracture,

$$\%\Delta L = \left(\frac{l_f - l_o}{l_o}\right) \times 100 \qquad \text{Equation 8}$$

where l_f is the fracture length and lo is the original gauge length. A significant proportion of the plastic deformation at fracture is confined to the neck region; the magnitude of %ΔL will depend on specimen gauge length. Since the elongation will vary with different gauge lengths, it is important to remove the size effect to produce data that is characteristic of the given material and not the particular specimen. The elongation is therefore divided by the original gage length to eliminate the size effects [62]. Elongation is inversely proportional to hardness, elastic modulus, and tensile strength. Meaning the greater a material's hardness, modulus, and tensile strength, the less it will elongate under stress.

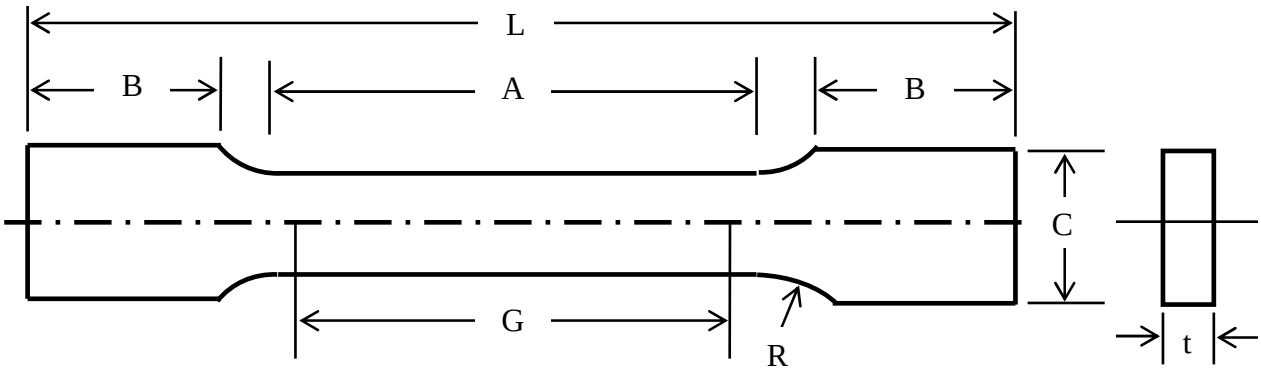

Figure 23. Rectangular tension test specimen where A is length of reduced section, B is length of grip section, C is width of grip section, G is gauge length, L is overall length, R is radius of filet, t is thickness, and W is width [81].

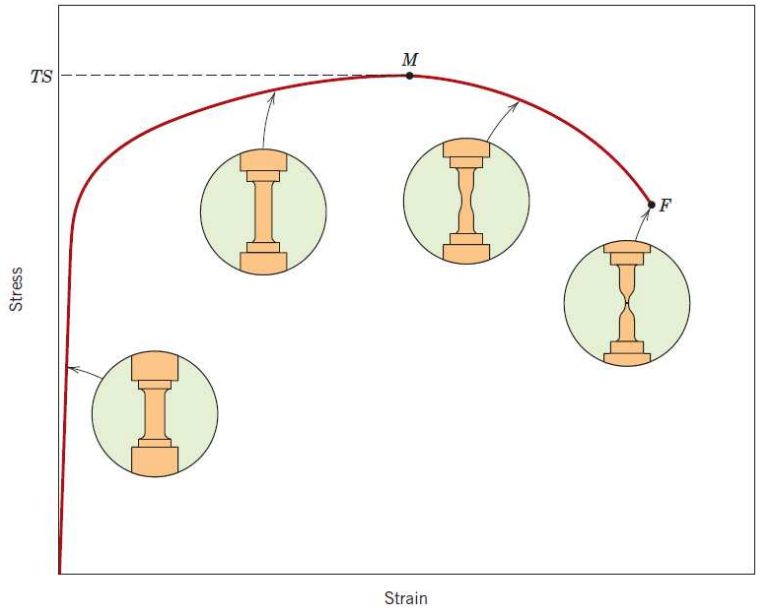

Figure 24. Schematic of a stress-strain diagram showing linear elastic deformation for loading and unloading cycles [64].

3.4 Corrosion Assessment

Mg alloys exhibit an attractive commodity for industrial applications like the automotive/transportation industries. Mg provides low weight, cost efficient solutions based on a fully recyclable material [83]. Poor corrosion resistance of Mg alloys has been a major obstacle to their widespread applications as structural materials [84]. The problem of metallic corrosion is one of significant proportions; in economic terms, it has been estimated that approximately 5% of an industrialized nation's income is spent on corrosion prevention and the maintenance or replacement of products lost or contaminated as a result of corrosion reactions [64]. However, there is a growing interest in the medical community to use corrodible alloys in a number of medical applications, due to their ability to degrade through corrosion reactions in the body fluid. *In vitro* corrosion tests are cost effective, simple to construct, and helpful in predicting the corrosion behavior of biodegradable materials.

3.4.1 Galvanic corrosion. Corrosion is defined as the destructive and unintentional attack of a metal. In terms of Mg, the most common form of corrosion that occurs in an aqueous environment is galvanic corrosion. This form of corrosion occurs when the two metals or alloys having different compositions are electrically coupled while exposed to an electrolyte [64]. During a galvanic reaction, the base metal or more reactive metal in the particular environment will experience corrosion; the more inert or noble metal, the cathode, will be protected from corrosion [64]. More specifically, one of the metals in the galvanic couple becomes the anode and corrodes faster than it would by itself, while the other becomes the cathode and corrodes slower than it would alone [85]. Metallic atoms characteristically lose or give up electrons in what is called an oxidation reaction; the site at which oxidation takes place is called the anode [64, 85]. For example, metal M with an *n* valance electron may undergo the following oxidation reaction where M becomes positively charged and loses its *n* valance electron (Figure 25):

$$\mathrm{M} \rightarrow \mathrm{M}^{n+} + ne^{-} \qquad \text{Equation 9}$$

By convention, the electrons generated from each metal atom under oxidation must transfer to and become a part of another element or compound which is said to undergo reduction. Some metals corrode in acid solutions which have high concentrations of hydrogen ions that are reduced and hydrogen gas is generated as follows (Figure 25):

$$2\mathrm{H}^{+} + 2e^{-} \rightarrow \mathrm{H}_2 \qquad \text{Equation 10}$$

The location at which this reduction occurs is called the cathode. For galvanic corrosion to occur, three conditions must be present [85]:

1. Electrochemically dissimilar metals must be present
2. These metals must be in electrical contact, and
3. The metals must be exposed to an electrolyte

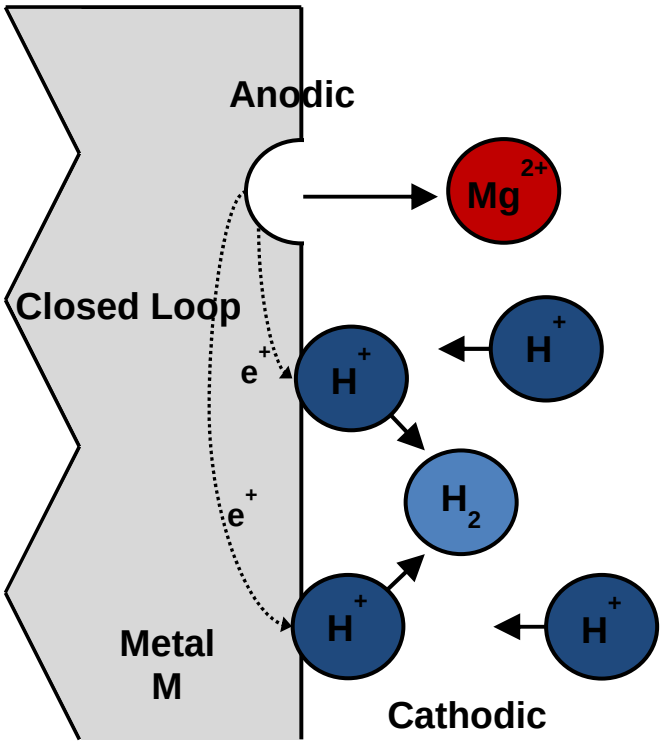

Figure 25. The electrochemical galvanic reactions associated with the corrosion of hypothetical metal M in an acid solution.

3.4.2 Immersion corrosion test. The two most common corrosion testing procedures used to determine the *in vitro* corrosion rate of a biodegradable material are the electrochemical method and the immersion corrosion test. However, the corrosion rate obtained from electrochemical methods may be unreliable due to the negative difference effect (NDE) which should be regarded as a common process in the corrosion of Mg [86]. The NDE effect is essentially the effect that the measured hydrogen evolution is greater than the expected hydrogen evolution. For most metals, the hydrogen evolution decreases with an increase of the applied potential or current density. However, for Mg, it is found experimentally that, with increasing potential, both the Mg corrosion rate and the hydrogen evolution rate increase [86]. This electrochemical phenomenon causes the weight loss calculated with Faraday's law is lower than

the weight loss determined experimentally. Consequently, for this study, immersion corrosion testing was utilized.

Immersion testing is one of the most frequently conducted experiments for evaluating the corrosion of metals in aqueous solutions. The foundation of an immersion test is that a test specimen is completely immersed in a corrosive solution for a set period of time and then the specimen is removed and analyzed. However, a number of factors must be considered to achieve specific goals and to ensure adequate reproducibility of test results. The actual conditions of the test are usually determined by the nature of the problem at hand, the ingenuity of the investigator, and the budget of the test program [87].

3.4.2.1 Test specimen preparation. Test specimens of each alloy were cut into 10 mm×10 mm×3 mm pieces and polished with 400, 600, 800, 1000, and 1200 grit carbide papers and ultrasonically cleaned with acetone. Initial measurements of each specimen where recorded which included the initial weight (g), thickness (mm), and surface area (cm^2).

3.4.2.2 Test conditions. Two types of test solutions were used for the immersion tests. The first type of solution was 0.9% NaCl physiological saline solution which consisted of 0.9% NaCl per 1000ml of deionized water. The second type of solution was a cell culture medium called Minimum Essential Medium Alpha (MEMα). Test specimens were individually placed into containers and were filled with test solution based on the "solution volume-to specimen area" ratio of 0.50 ml/mm^2 [88]. Each container was then incubated at 37°C in humidified atmosphere of 5% CO_2 for 10 days. Specimens were removed from the container and immersed in acetone to stop the corrosion process. Cleaning specimens post immersion testing is a vital step in the corrosion test procedure and if not done properly, can cause misleading results [88]. Chemical cleaning was utilized for this study which is the removal of material from the surface

of the test specimen by dissolution in a chemical solution. A chromic $AgNO_3$ acid solution was used to clean or remove all corrosion products from the test specimens. A “blank” specimen which was not subjected to the immersion testing procedures of was weighed before and after exposure to the cleaning procedure to establish and correct the mass loss created by the chromic solution.

3.4.2.3 Corrosion rate. The corrosion rate, or the rate of material removal as a consequence of the chemical reaction, is an important corrosion parameter in biomedical material development. For this study, calculating the corrosion rate (mm/y) is based on the following equation [88]:

$$\text{Corrosion rate} = (K \times \Delta W)/(A \times t \times D) \qquad \text{Equation 11}$$

where *K* is the constant 8.76×10^4, to yield a mm/y unit for the corrosion rate; *t* is the time of exposure in hours to the nearest 0.01 h; A is the total surface area in cm^2 to the nearest 0.01 cm^2; ΔW is the mass loss in g to the nearest mg (corrected for any loss during cleaning); and D is the density in g/cm^3.

3.5 Cytocompatibility Assessment

Alloying is used to alter the mechanical capabilities and corrosion behavior of Mg. However this technique is restricted in the case of designing Mg alloys for biomedical applications because the toxicity of alloying elements must be taken into account [89]. There are two broad categories commonly used to assess the toxicity of biomaterials: *in vitro* and *in vivo* toxicity testing.

In vivo (Latin for “within the living”) refers to experimentation using a whole living organism as opposed to a partial or dead organism [90]. Animal studies and clinical trials are two forms of *in vivo* testing. In terms of implant materials, *in vivo* testing is used to determine the

biocompatibility of a material. Animal studies are generally adopted by the Globally Harmonized System (GHS) classification and human health risk assessments [91]. FDA clearance of new products or devices to be used in clinical applications requires *in vivo* animal testing to provide information that demonstrates it is as safe and effective as predicated. Even though *in vivo* assessment is important to determining the biocompatibility of an alloy, increasing societal concerns about animal use and the high cost of conducting regulated animal tests have rendered the need of alternative *in vitro* test methods that can reduce the use of animal testing for acute systemic toxicity testing.

In vitro (Latin for "within the glass") refers to the technique of performing a given procedure in a controlled environment outside of a living organism [90]. Cellular biology utilizes this technique to conduct experiments using living cells grown outside of a living organism. In terms of implant materials, *in vitro* testing is used to determine the cytocompatibility of a material. Cytotoxicity is the quality of being toxic to cells [92]. Cells exposed to a cytotoxic compound can react in a variety of ways which include loss of membrane integrity, hindered cell proliferation, and apoptosis. *In vitro* cytotoxicity assays are a good tool for initial material screening. This type of testing has a great potential for reducing and refining traditional *in vivo* toxicology tests [91]. However, one major inherent limitation of *in vitro* testing is the inability to replicate precise cellular conditions of an organism which leads to results that do not correspond to *in vivo* results [72, 90]. As a result of this limitation and the restrictions applied by regulatory institutions, *in vivo* animal testing is still considered the gold standard in assessing the biocompatibility and safety of a material to be used in biological systems. The advantages of *in vitro* testing is the significant simplification of a complex biological system which a number of small components throughout the system can be focused upon, reduced costs through cost-

effective testing compared to *in vivo* studies, and an alternative method which can provide benefits in terms of ethical considerations that are seen which animal and human testing [90, 93].

Considering the information discussed above, Live/Dead and MTT *in vitro* cell viability assays were used to determine the cytocompatibility of the alloys produced in this study.

3.5.1 Cell culture procedure. The MC3T3-E1 pre-osteoblast cell line (American Type Culture Collection, Manassas, VA USA) was adopted for the cell viability assessment of this dissertation. MC3T3-E1cells are obtained by the cloning of cells isolated by collagenase digestion of newborn mouse calvarias [94]. Cloned MC3T3-E1 cells isolated from newborn mouse calvarias retains an ability to differentiate into osteoblastic cells *in vitro* which ultimately form bone-like ossicles [95]. The MC3T3-E1 cells were cultured in 75 cm^2 tissue culture flasks in a complete growth alpha minimum essential medium (MEMα) which consisted of 10% fetal bovine serum and 1% penicillin/streptomycin and incubated in a humidified atmosphere of 5% CO_2 at 37°C. The cells were sub-cultured every 4 to 5 days using 0.25% (w/v) trypsin – 0.53 mM EDTA solution and fresh medium was added every 2 to 3 days.

3.5.2 Live/dead assay. The Live/Dead assay is a two-color fluorescence viability assay that is based on the simultaneous determination of live and dead cells with two probes that measure intercellular esterase activity and plasma membrane integrity. This type of assay characterizes metabolically active cells from injured or dead cells. Live cells are distinguished by the presence of universal intracellular esterase activity. The colorless calcein acetomethoxy (calcein AM) dye is retained and metabolized by live cells, producing an intense uniform green fluorescence. The ethdium homodimer-1 (EthD-1) enters cells with damaged membranes and undergoes a 40-fold enhancement of fluorescence upon binding to nucleic acids, thereby producing a bright red fluorescence in dead cells.

For this study, Mg alloys were cut and polished with 400, 600, and 800 grit carbide papers and ultrasonically cleaned with acetone. Each individual Mg samples was sterilized on both sides with ultraviolet light (UV) for 15 minutes. The samples were placed in containers and immersed in MEMα, according to the extract ratio given in the "*Biological evaluation of medical devices: Sample preparation and reference materials*" ISO standard [96], and incubated in humidified 5% CO_2 atmosphere at 37°C for 72 h. The samples were removed from the solution and the extract MEMα solution was sterilized via 0.2 µm filtration. For exposures, the MC3T3-E1 cells were incubated with the extract solution at a concentration gradient of 100%, 50%, 25%, and 10% for 24 and 72 hours. The extract solutions were removed from the cells and the cell surfaces were washed with phosphate buffered saline (PBS) and the dye solution was seeded over the cells and placed in the dark for 30 minutes. Dye solution consists of 2 nM of calcein AM and 4 nM of EthD-1 in PBS. Fluorescence optical microscopy was used to take images of each well using the EVOS® FL Cell Imaging System.

3.5.3 MTT assay. MTT (3-(4,5-Dimethylthiazol-2-yl)-2,5-diphenyltetrazoliumbromide) is a water soluble membrane permeable dye which is metabolized to dark-purple crystals of formazan by mitochondrial dehydrogenases of living cells [97]. These crystals are impermeable to cell membranes and are accumulated in proliferating, undamaged cells. After lysis of the cell and solubilization of the formazan crystals, the optical density (OD) of the dye is quantified using a multi-well-spectrophotometer (SpectroMax M5 microplate reader) at around 550 nm. The number of proliferating cells is directly proportional to the development of dark-blue crystals and can be quantified by means of a standard calibration. Since the total mitochondrial activity is related to the number of viable cells, the MTT assay is broadly used to measure the *in vitro* cytotoxic effects of foreign compounds on cell lines or primary patient cells [97].

Each sample purposed for the MTT assay were prepared and sterilized, as discussed in section 3.5.2, immersed in MEMα according to the extract ratio given in the "*Biological evaluation of medical devices: Sample preparation and reference materials*" ISO standard [96] , and then incubated at 37°C in a humidified atmosphere of 5% CO_2 for 72 hours. Extract solutions were sterilized via 0.2 µm filtration. For exposures, the MC3T3-E1 cells were incubated with the extract solution at a concentration gradient of 100%, 50%, 25%, and 10% for 24 and 72 hours. The MTT reagent was dissolved at 5 mg/ml in PBS and then diluted at a 10 to 1 ratio with MEMα media. The extract was removed from cells and the cells were washed with fresh media. The MTT/media mix was transferred to each well to yield a final volume of 110µl/well. Plates were incubated for 4 hours at 37°C and 5% CO_2. A sodium dodecyl sulfate (SDS) solution mix, which consists of 1g of SDS and 10ml of 0.01M hydrochloric (HCL) acid, was added to each well at a volume of 100µl and incubated for 16 hours. Absorbance was read at 570 nm using a Spectromax M5 microplate reader. The evaluation of the MTT assay was based on the percent of metabolic activity (Equation 12) of cells after 24 and 72 hours of incubation.

$$\%\ \text{of Metabolic Activity} = \frac{\text{OD of extract treated wells}}{\text{OD of control wells}} \times 100 \qquad \text{Equation 12}$$

3.6 Statistical Analysis

For all quantitative outcomes of this study, the one-way or two-way analysis of variance (ANOVA) statistical analysis methods were applied to scrutinize the data. The analysis of variance is a statistical method used to test differences between two or more means. ANOVA is used to test general rather than specific differences among means [98].

3.6.1 One-way ANOVA. One-way ANOVA, also called one-factor ANOVA, compares three or more sets of measurements. For example, a study might assess the effect of one particular clinical drug on male and female rabbits. In this example, the one-way ANOVA allows

the study to be broken into groups according to the rabbits and then see if the effect of drug treatment is different across the rabbits. A one-way ANOVA test is chosen when [99]:

- A variable is measured in each subject several times, perhaps before, during, and after an intervention.
- A subject is recruited as matched groups, matched for variables such as age, ethnic group, and disease severity.
- An experiment is run several times, each time with several treatments handled in parallel.

Since experiment-to-experiment variability is anticipated, the data will be analyzed in such a way that each experiment is treated as a matched set. Matching should not be based on the variable you are comparing. If you are comparing blood pressures in three groups, it is OK to match based on age or zip code, but it is not OK to match based on blood pressure [99].

3.6.2 Two-way ANOVA. The two-way ANOVA, also called two-factor of variance, determines how a response is affected by two factors [99]. If an experiment has a quantitative outcome and two categorical explanatory variables that are defined in such a way that each experimental subject can be exposed to any combination of one level of one explanatory variable and one level of the other explanatory variable, then the most common analysis method used is two-way ANOVA [100]. For example, a study might assess the effect of three different types of clinical drugs in both male and female rabbits. In this example, the drug treatment is one factor and the gender of the rabbits is another. Two-way ANOVA simultaneously asks three questions:

1. Does the first factor systematically affect the results?
2. Does the second factor systematically affect the results?
3. Do the two factors interact?

When interpreting the results, the two-way ANOVA utilizes the p-value to answer the question: If the null hypothesis is true, what is the chance of randomly sampling subjects and ending up with as much of an interaction than you have observed [100]? When performing a hypothesis test in statistics, the p-value helps determine the significance of the results [101]. The p-value is a number between 0 and 1 and interpreted in the following way:

- A small p-value (typically ≤ 0.05) indicates strong evidence against the null hypothesis, so you reject the null hypothesis.
- A large p-value (> 0.05) indicates weak evidence against the null hypothesis, so you fail to reject the null hypothesis.
- p-values very close to the cutoff (0.05) are considered to be marginal (could go either way).

The two-way ANOVA reports three p-values:

1. Tests the null hypothesis that time has no effect on the outcome.
2. Tests the null hypothesis that the treatment makes no difference on average.
3. Tests for interactions.

CHAPTER 4

Results and Discussion

This chapter presents the collection of qualitative and quantitative results produced from the experimental methods and concepts described in the previous chapter and their interpretation. The results are categorized according to experiment type and alloy composition. The results will include microstructural assessment, mechanical testing analysis, corrosion assessment, and cytocompatibility evaluation.

4.1 Microstructure and Phase Constitutions

4.1.1 As-cast MgZnCa alloys. The composition of the alloying elements were measured by SEM-EDS analysis which was accomplished to provide detail about the alloy's actual composition after casting which is described in Table 7 (Appendix). In all cases the actual composition of the Zn and Ca elements were more compared to the nominal composition. Conversely there is a 1−2% loss of magnesium which could be a result of a common phenomenon called "melting loss". Depending on the volume of throughput and furnace design, high melt losses are often encountered in melting operations. As reported in the experimental methods and concepts section (Chapter 3), the Mg melt was stirred at a specified temperature above 700°C after the addition of alloying elements. This has to be regarded as critical for the protective Ar gas because its efficiency may be reduced at these temperatures [102]. As a result, a certain amount of Mg can react with the environment and the components of the protective gases. This leads to the formation of magnesium oxides and dross which can be incorporated into the casting.

4.1.1.1 Grain structure analysis. The as-cast Mg−*x*Zn−0.3Ca alloy grain structures are illustrated in Figure 26. The grain morphology is observed to be typically hexagonal globular in

nature. It can be observed that the level of zinc content has an influence on the grain structure because the intermetallic phase observed along the grain boundaries and within the grains become more potent and the eutectics are thickened as the zinc concentration increases. The intermetallic secondary phase is found to be rich in both Zn and Ca which is supported by the SEM-EDS elemental mapping images in Figure 27.

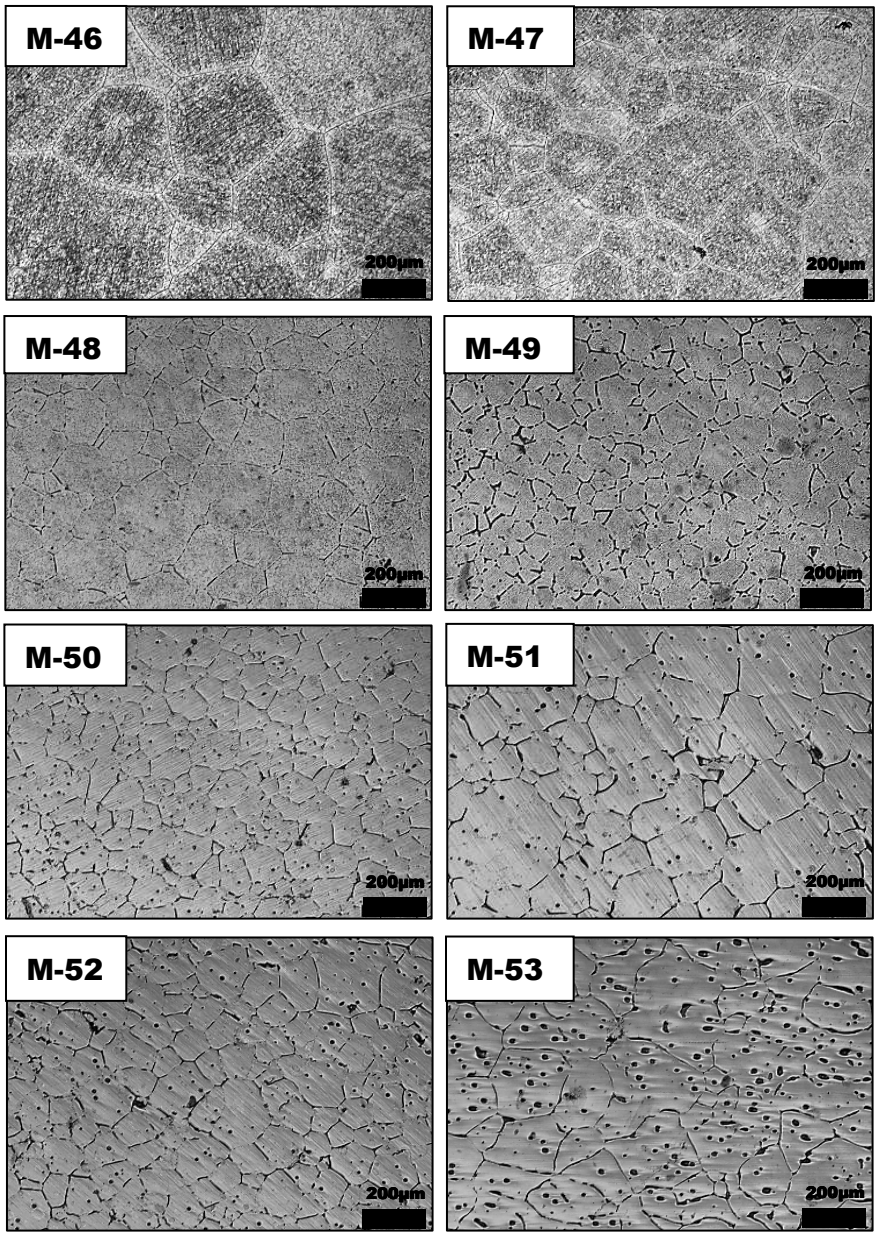

Figure 26. Optical micrographs of as-cast Mg−*x*Zn−0.3Ca alloy grain structures.

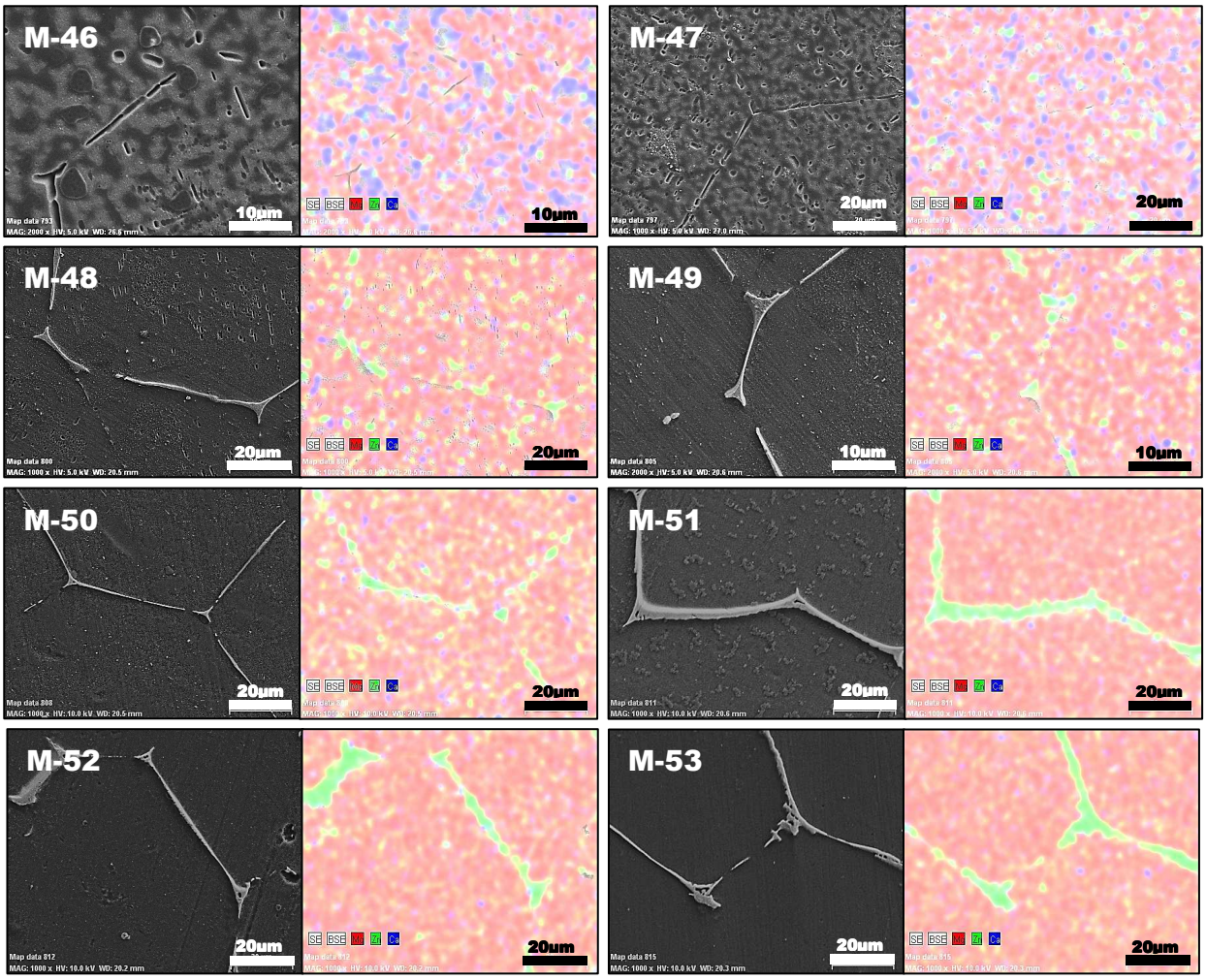

Figure 27. SEM images and EDS elemental mapping images along the grain boundaries of the as-cast Mg−*x*Zn−0.3Ca alloys.

4.1.1.2 Phase constitution. Through EDS compositional analysis, the intermetallic secondary phases are identified and presented in Figure 28. For the M-46 and M-47 samples, the dominate phase detected was the α−Mg matrix. The solute elements are all dissolved into the Mg matrix and no intermetallic precipitates appear in grain boundaries.

Based on the cooling curves developed by Bakhsheshi-Rad *et al.* [103], during solidification the primary α−Mg phase is initially formed. As the temperature of the molten metal decreases, there is a rejection of alloying elements from the α−Mg dendrite at the liquid-solid

interface which causes an increase in the Ca concentration in the solid formed from residual liquid among the Mg dendrite network. $CaMg_2$ secondary phase starts to precipitate along the grain boundaries as the temperature decreases. The last stage of the solidification process caused the appearance of the $Ca_2Mg_6Zn_3$ intermetallic phase [103].

Both the $CaMg_2$ and $Ca_2Mg_6Zn_3$ phases were detected in the M-48 alloy. This is in agreement with the ternary phase diagram presented in Figure 29. For the M-49 thru M-52 alloys, the main phase detected was the $Ca_2Mg_6Zn_3$ phase which similar to what Hradilová *et al.* and Kubok *et al.* found in their investigation of the Mg−4.0Zn−0.4Ca and Mg−3.0Zn−0.5Ca (wt.%) systems, respectively [74, 104]. Additionally, Sun *et al.* [44] prepared an Mg−4.0Zn−0.2Ca alloy for their investigation which underwent XRD scans to examine the phase of the as-cast alloy from 20 to 90° with a step size of 0.05. Peaks from the α-Mg and the $Ca_2Mg_6Zn_3$ phase was detected, as well as peaks from the $Ca_2Mg_5Zn_{13}$ phase. There is no indication of the $CaMg_2$ phase within M-49 thru M-52 alloys. The higher concentration of Zn (3−6 wt.%) caused the suppression of the $CaMg_2$ phase suggesting the following solidification process [103]:

$$L \rightarrow \alpha{-}Mg + Ca_2Mg_6Zn_3 \qquad \text{Equation 13}$$

The MgZn phase was also detected within these alloys starting at the M-50 sample. For the M-53 alloy, a new phase was discovered ($Mg_{12}Zn_{13}$) in addition to the α−Mg and $Ca_2Mg_6Zn_3$ phase. This phase differs from the $Mg_{51}Zn_{20}$ phase in which Bakhsheshi-Rad *et al.* discovered for their alloy with Zn content of 9 wt.%. It is also noticed that with the increase of Zn, the predominant phase of the intermetallic region shifts from $Ca_2Mg_6Zn_3$ to $MgZn/Mg_{12}Zn_{13}$ which is in agreement with previous studies [103] and the solidification process described in Equation

13. It is also observed that a lamellar eutectic structure starts to develop at the 4.0 wt.% Zn concentration.

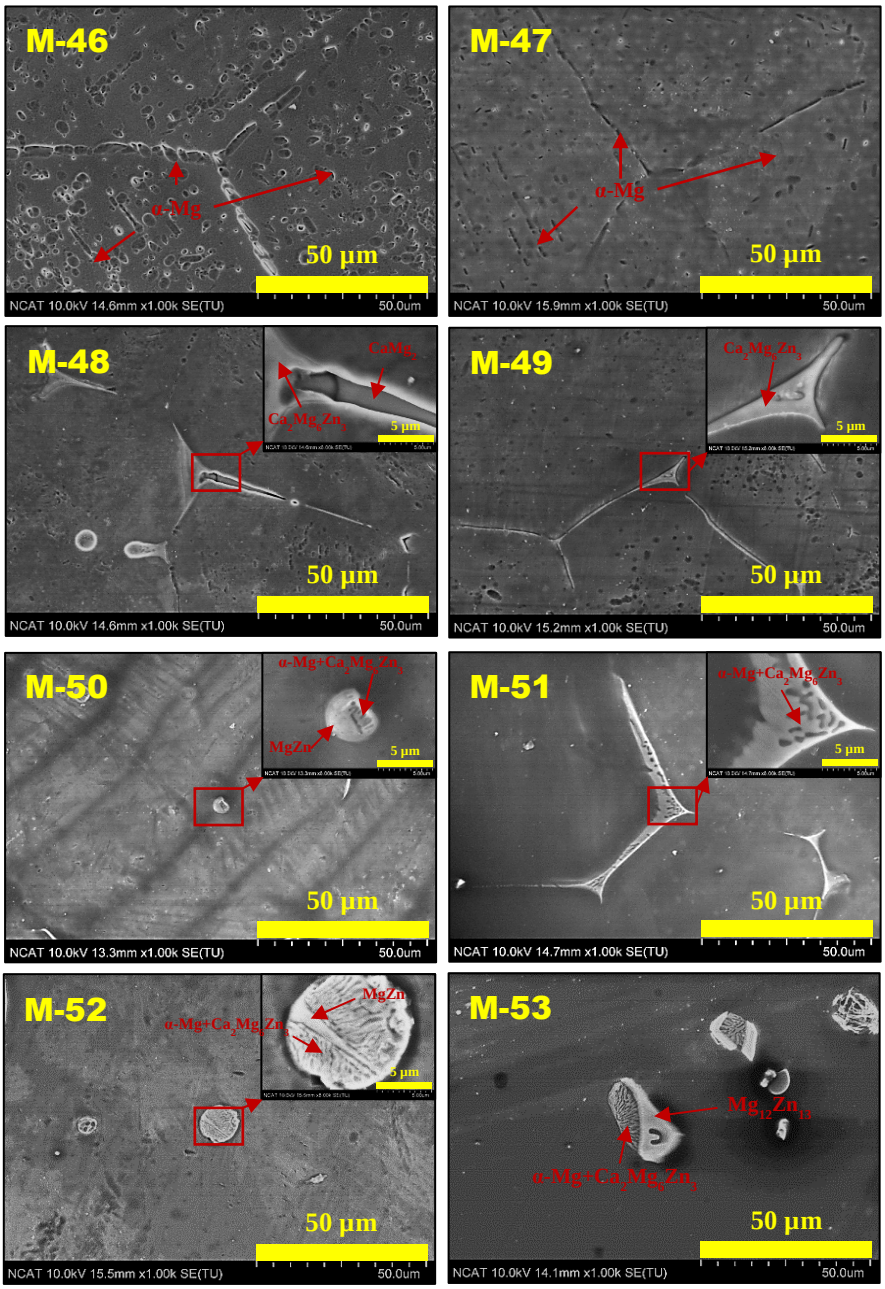

Figure 28. SEM micrographs of as-cast Mg−*x*Zn−0.3Ca alloys detailing the specific phases along the grain boundary and within the Mg matrix.

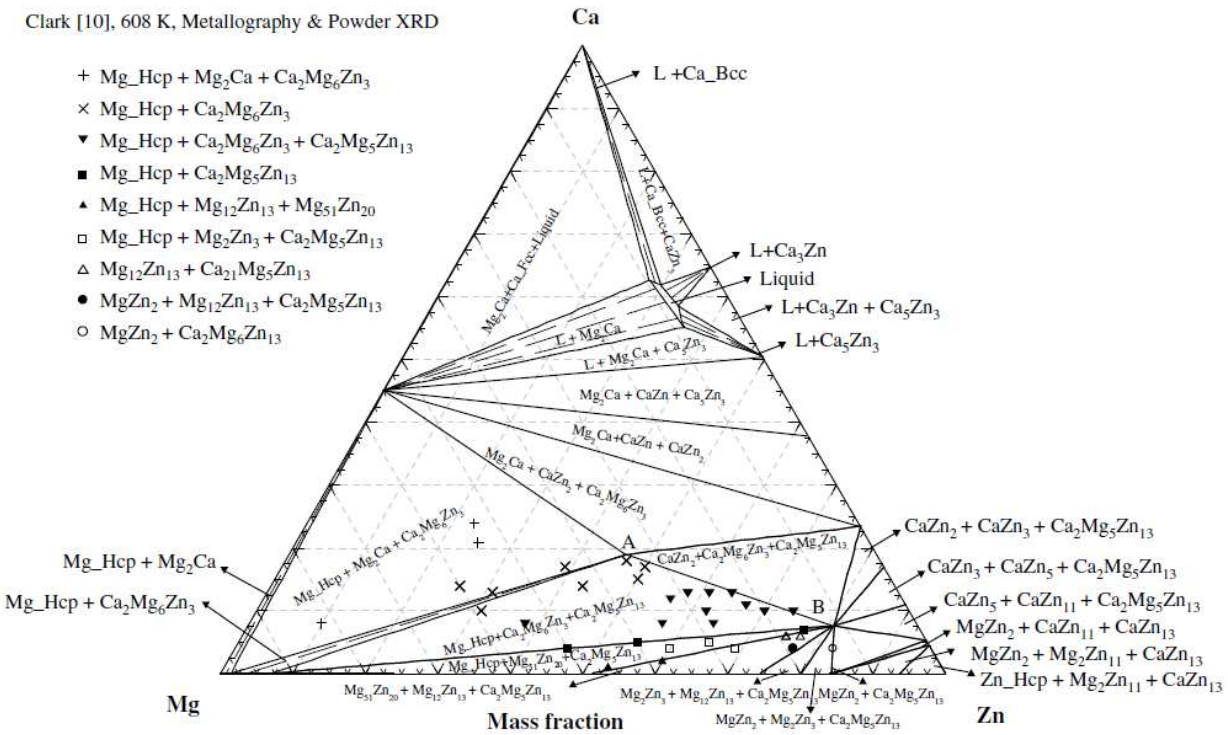

Figure 29. Calculated isothermal section of the Mg−Ca−Zn system at 335°C with two ternary compounds compared with experimental data of [105] where A denotes: $Ca_2Mg_6Zn_3$ and B denotes: $Ca_2Mg_5Zn_{13}$ [106].

4.1.1.3 Grain size analysis. The average grain diameter (μm) of the as-cast Mg−*x*Zn−0.3Ca samples, which were counted from the OM images utilizing the ASTM line intercept method [75], are described in Figure 30. The samples were compared to an Mg−0.3 wt.%Ca sample with no Zn addition to get a better understanding of the effects of adding Zn to the Mg−Ca system in terms of the grain size. Ca is commonly known to provide grain refinement to Mg alloys, but for this study all alloys have the same weight percentage of Ca (0.3 wt.%). Consequently the amount of Zn is the underline factor in the grain size difference between the alloys.

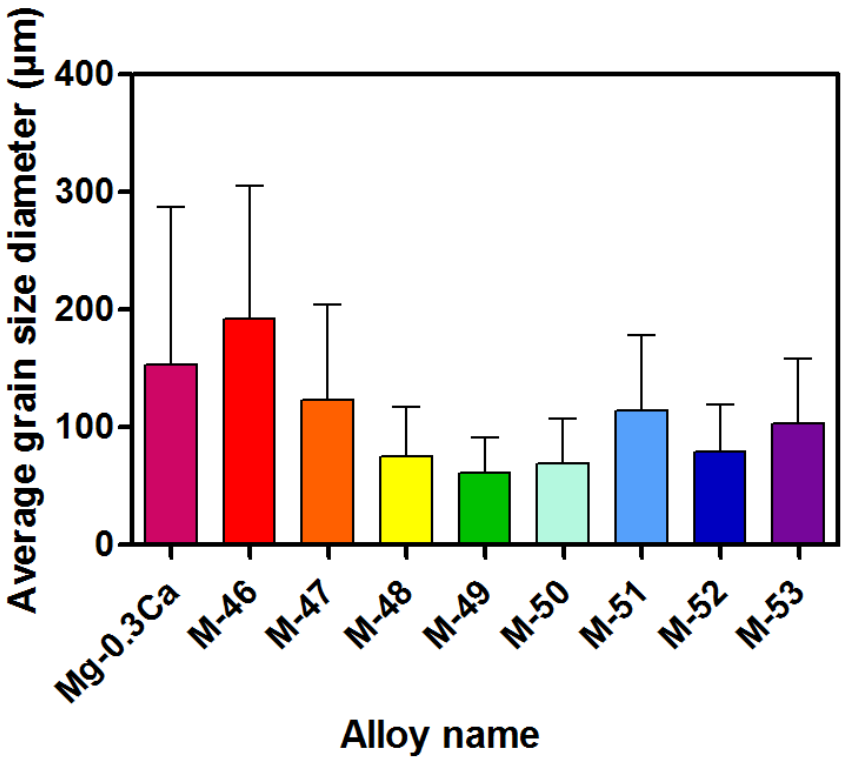

Figure 30. Average grain diameter in µm of as-cast Mg−*x*Zn−0.3Ca samples compared with the Mg−0.3Ca system determined from the ASTM line intercept method.

The one-way ANOVA statistical analysis was conducted to compare the significance between the average grain diameters of the as-cast Mg−*x*Zn−0.3Ca samples. From the one-way ANOVA analysis, it was determined that there was a significant difference in the average means of the grain diameters at the $p < 0.05$ level [$F(8, 495) = 18.45$, $p < 0.0001$]. From this information it can be concluded that the effects of the level of Zn concentration on the average grain diameter were substantial and not created by chance. There is no significant difference found between the average grain size of the Mg−0.3Ca sample (152.8 ± 134.8 µm) and the M-46 (192.3 ± 113.1 µm) and M-47 (123.0 ± 81.0 µm) samples. The grain size reduction doesn't significantly occur until the Zn level reaches 2.0 wt.% in which the grain diameter average starts reduce to the lowest points at M-49 and M-50 in which the grain size is 60.97 ± 30.4 µm and

69.2 ± 38.4 µm respectively. The grain size reduction as a function of the Zn level increase is in agreement with Bakhsheshi-Rad *et al.* [103] who found that the addition of Zn from 1 to 3 wt.% in the ternary Mg−*x*Zn−Ca alloy caused grain refinement.

When examining the reason behind the reduction of grain size diameter as a function of the increase in Zn concentration, it is pertinent to understand the solidification process. The solidification of a solid transpires by nucleation and growth. The key solidification processes that control the final microstructure are the initial nucleation events, the growth of these nuclei into primary dendrites and finally eutectic solidification [107]. When a metal solidifies, small particles of solid forms from the molten liquid which act as a nucleus site and grow as other atoms attach themselves to this solid nucleus site to create a crystal or grain. The size of the grains in a metal vary with the rate of nucleation and the rate of growth [62]. The greater the nucleation rate, the smaller the resulting grains and inversely the greater the rate of growth, the larger the grains. For the Mg−Zn system, Huan *et al.* [89] explained that Zn content closer to the maximum solubility in Mg (6.2 wt.% at 635°C) leads to more MgZn precipitates under the equilibrium conditions and Wasiur *et al.* [106] discovered that the addition of Zn in a Mg−Ca alloy system creates the refinement of precipitates as well. Therefore, it is believed that there is higher precipitation of Zn from 0.5 to 4 wt.% which provides more nucleation sites which can cause an increase in the number of grains resulting in smaller grains. Therefore, the addition of Zn can refine the grains and introduce more secondary phases which is in agreement with Du *et al.* [25]. The average grain diameter fluctuates from M-51 to M-53. The one-way ANOVA has the ability to compare each individual mean with one another and it was determined that from M-50 to M-53 there were no significant difference excluding M-51 as an outlier.

These grain size results are based on one sample extracted from the bulk of each individual as-cast alloy. Each grain measurement was acquired along the surface of the sample cut in one direction. To determine reproducibility, more samples must be taken at from the bulk of each alloy and grain size measurements must be determined from the surface of each sample cut in many directions. The same limitation is found in the grain size analysis throughout this study.

4.1.2 Heat treated MgZnCa alloys. After determining the grain size of the as-cast Mg−*x*Zn−Ca alloys, the next step was to perform additional processing techniques in the way of heat treatment processing to analyze its effect upon the as-cast alloys. The M-49 and M-50 samples were selected for undergoing additional T4 heat treatment processing.

4.1.2.1 Grain structure analysis. The nominal compositions of the M-49 and M-50 samples were Mg−3.0wt%Zn−0.3%Ca and Mg−4.0wt%Zn−0.3%Ca respectively. To determine the optimum temperature and time combination to have successful heat treatment outcomes, several different treatment parameters were explored. The first double stage heat treatment combination of parameters considered was at 300°C for 20 h and then 400°C for 2, 4, 6, and 8 h which was performed on the M-50 sample. OM images were taken of the T4 heat treated M-50 alloy which is illustrated in Figure 31. No strong oxidation or heat treatment defects were observed after heat treatment. Descriptive evidence suggests that when heat treatment is applied, the secondary phase along the grain boundary and within the inner grains is more refined than the as-cast counterpart. This is supported by the average area of the secondary phase of the as-cast M-50 sample compared to the heat treated samples (Figure 32). The average area of the secondary phase was determined from OM images of the heat treated M-50 samples (n = 3) taken at 5x magnification.

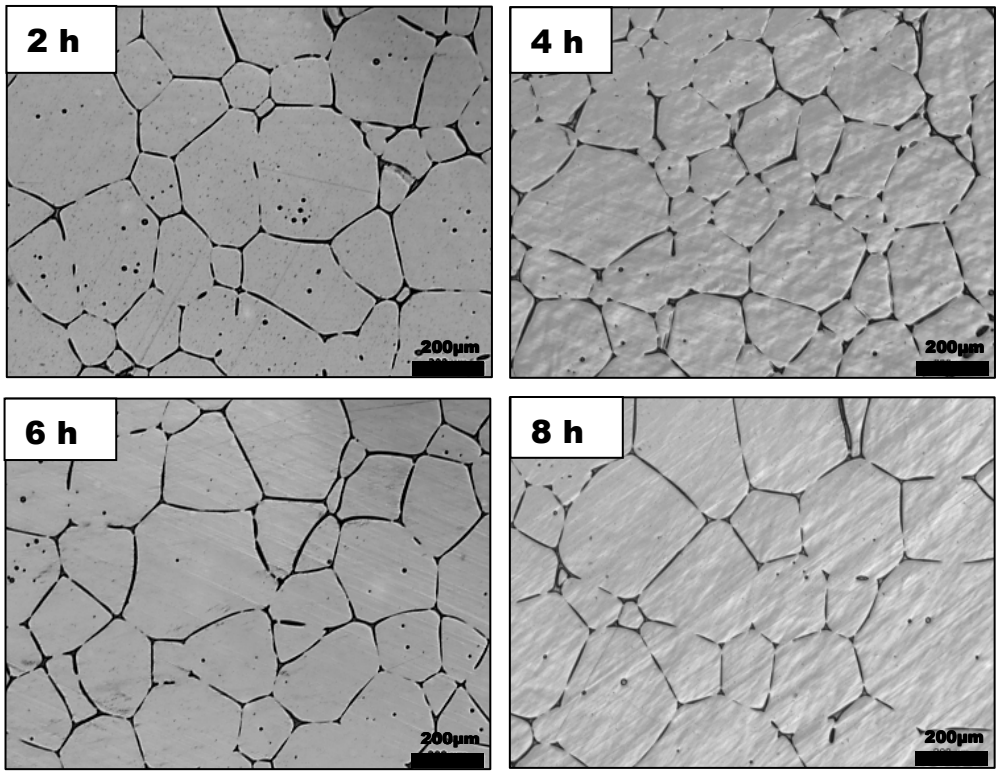

Figure 31. Optical micrographs of the grain structures of the M-50 samples that were T4 heat treated at 300°C for 20 h and then 480°C for 2, 4, 6, and 8 h.

The one-way ANOVA determined that there was a significant reduction of the secondary phase after heat treatment compared to the as-cast sample [$F(4,10) = 17.15$, $p = 0.0002$]. The purpose of the solution heat treatment process is to dissolve constituent atoms into the base metal. This process is accomplished by diffusion, which is the phenomenon of material transport by atomic motion [64]. Diffusion requires enough energy to overcome the energy barrier needed for atoms to migrate from lattice site to lattice site. Based on the atomic radii of Mg (141pm), Zn (122pm), and Ca (176pm), the type of diffusion occurring in the Mg−*x*Zn−0.3Ca system of this study is substitutional diffusion. In substitutional diffusion, there must be an empty adjacent lattice site for atomic motion to occur. The simplest case of substitutional diffusion is self-diffusion which occurs for pure metals.

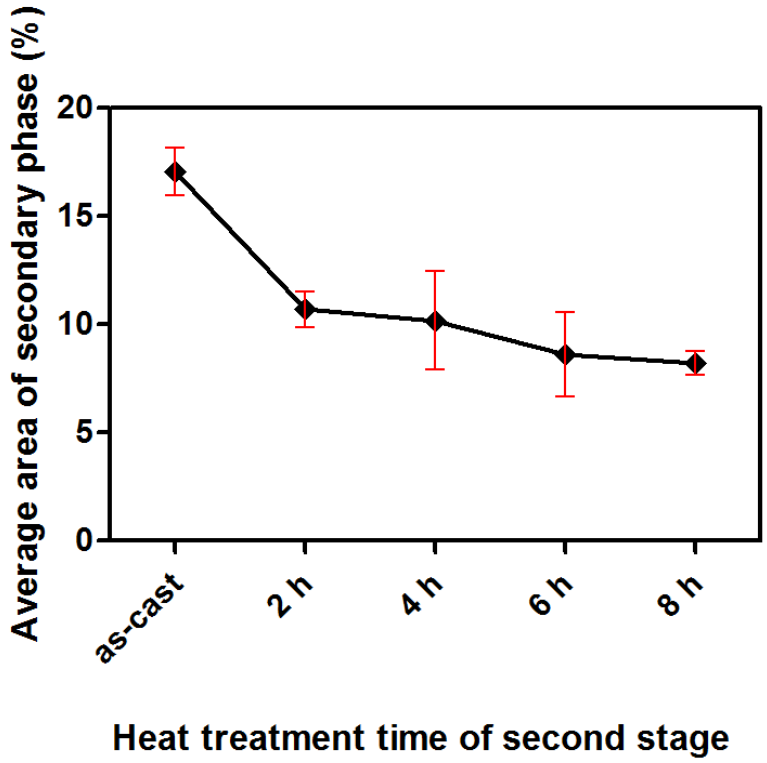

Figure 32. Average area of intermetallic phase of as-cast and heat treated (300°C 20 h + 480°C *x*h) M-50 samples taken from OM images at 5x (n = 3).

During self-diffusion all atoms are chemical identical and this leads to a simple relationship between jump frequency and diffusion coefficient. In binary alloys, this relationship is more complex. The rate at which solvent and solute atoms can move into a vacant site is not equal and each atomic species must be given its own diffusion coefficient [108]. At a specific temperature, however, some small fraction of the total number of atoms is capable of diffusion based on their vibrational energies which increase with rising temperature [108]. The addition of a third diffusing component, i.e. ternary alloys, to a solid solution produces even more complexities because the behavior of two solutes must now be consider. When comparing the HCP structure of Mg and Zn to other various materials, the activation energy needed for diffusion to occur is lower than most atomic structures (Figure 58b, Appendix). Therefore the

heat treatment temperature coupled with the relatively low treatment time was able to activate the solute atoms enough for diffusion to occur which explains the significant decrease in secondary area compared to as-cast M-50 samples.

In terms of the effect of the treatment time on the efficiency of diffusion of the secondary phase, there is no statistical significant difference between each heat treated samples. This suggest that an extended solution treatment time must be studied further to get a better understanding of the effects of treatment on the dissolution of the secondary phase trend.

4.1.2.2 Grain size analysis. Figure 33 describes the average grain diameter in µm of the heat treated M-50 samples compared to the as-cast M-50 samples which were counted from the OM images. The one-way ANOVA statistical analysis was conducted to compare the effects of the heat treatment on the average grain size. From the one-way ANOVA analysis, there was a significant difference in the average means of the grain diameters at the $p < 0.05$ level [$F(4, 217) = 19.71$, $p < 0.0001$]. From this statistical information it can be concluded that the effects of the heat treatment on the average grain diameter were substantial. More specifically, there is an increase in the average grain diameter once heat treatment is introduced to the M-50 samples. The average grain size of as-cast M-50 is 69.2 ± 38.4 µm. All heat treated M-50 samples show an increase in average grain size than that of the as-cast M-50 sample, suggesting that the introduction of this solution treatment increases the average grain size. Due to the relatively high temperatures used for the heat treatment processing, most of the secondary phase at the grain boundaries dissolved into the Mg matrix and as a result the grains grew. It can be seen that there was an initial increase in average grain size diameter as the treatment time increased until the grain size reached its apex of 170.4 ± 81.7 µm at a treatment time of 4 h. There is a slight reduction of grain size thereafter as the heat treatment time increases from 4 hours to 8 hours.

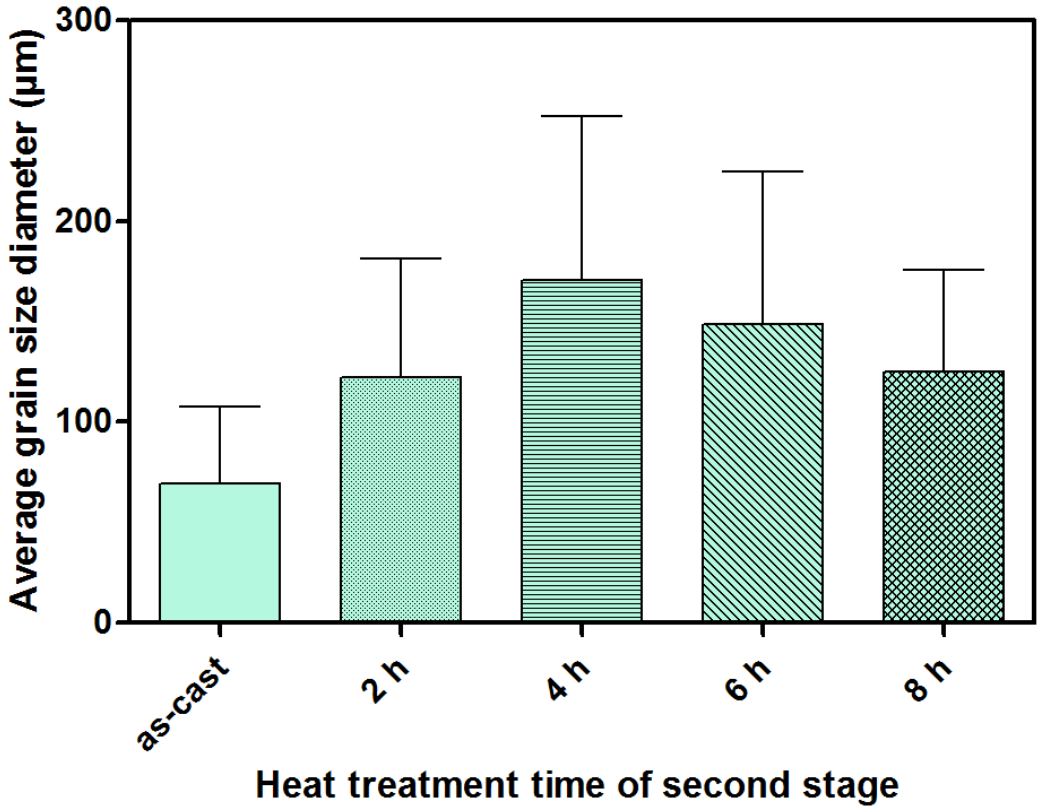

Figure 33. Average grain diameter in µm of heat treated (300°C 20 h + 480°C *x*h) M-50 samples compared with as-cast M-50 samples determined from the ASTM line intercept method.

However, the one-way ANOVA also compared each heat treated sample to one another and determined that there is no significant difference in the means. This suggests that the treatment time used for this experiment does not have a significant effect on the average grain size. Therefore an extended solution treatment time must be considered.

4.1.2.2.1 Knowledge gained through literature review. Alvarez-Lopez *et al.* [109] discovered that the best corrosion behavior of the AZ31 alloy corresponds with finer grain size in PBS. This is accredited to a more negative corrosion potential and the formation of a layer of corrosion products which offers more protection from the diffusion of ions to the electrode surface. Similarly, Estrin *et al.* [110] concluded from open circuit and potentiodynamic

polarization tests in 0.1M NaCl solution, that pure Mg experiences a decrease in the corrosion current with decreasing grain size which indicates better corrosion resistance. Even though there is successful integration of the secondary phase within the Mg matrix of the heat treated M-50 samples in this study, it can be seen that either the heat treatment temperature or the insufficient length of time causes a coalescence in grains which creates larger grain size that could be detrimental to its corrosion resistance. Mg alloys tend to corrode rapidly in physiological environment which creates a loss of mechanical integrity before the required time needed for bone tissue healing, which makes this first set of M-50 heat treated alloys unattractive to be used as implantable biomaterials. Therefore it was determined that there is a need to alter the heat treatment parameters to create a microstructure that will yield more favorable results.

4.1.2.2.2 Heat treatment trial II. Therefore a second trial run of T4 heat treatment conditioning was conducted. The double stage heat treatment temperature and time for this trial was altered from the first trial to 320°C for 24 h and then 400°C for 24 h, 48 h, 72 h, and 96 h. This process was conducted on both the M-49 (Zn = 3.0%) and M-50 (Zn = 4.0%) alloys.

In terms of the effect of this treatment parameter on the M-49 samples, it can be seen that the grain microstructure is altered as the treatment time increases (Figure 34a-d). For the M-50 samples, it is not as visually profound to discern the alteration of the grain structure by the heat treatment processing (Figure 34e-h). These two observations are supported by the reduction of secondary phase's graphs shown in Figure 35. It was determined that for the M-49 alloy, there was a significant reduction of intermetallic phases as the treatment time increased from 24 h to 96 h. More specifically, once this heat treatment procedure is introduced to the M-49 alloy, the secondary phase does not start to significantly reduce until the heat treatment time of the second stage extends to 48 h.

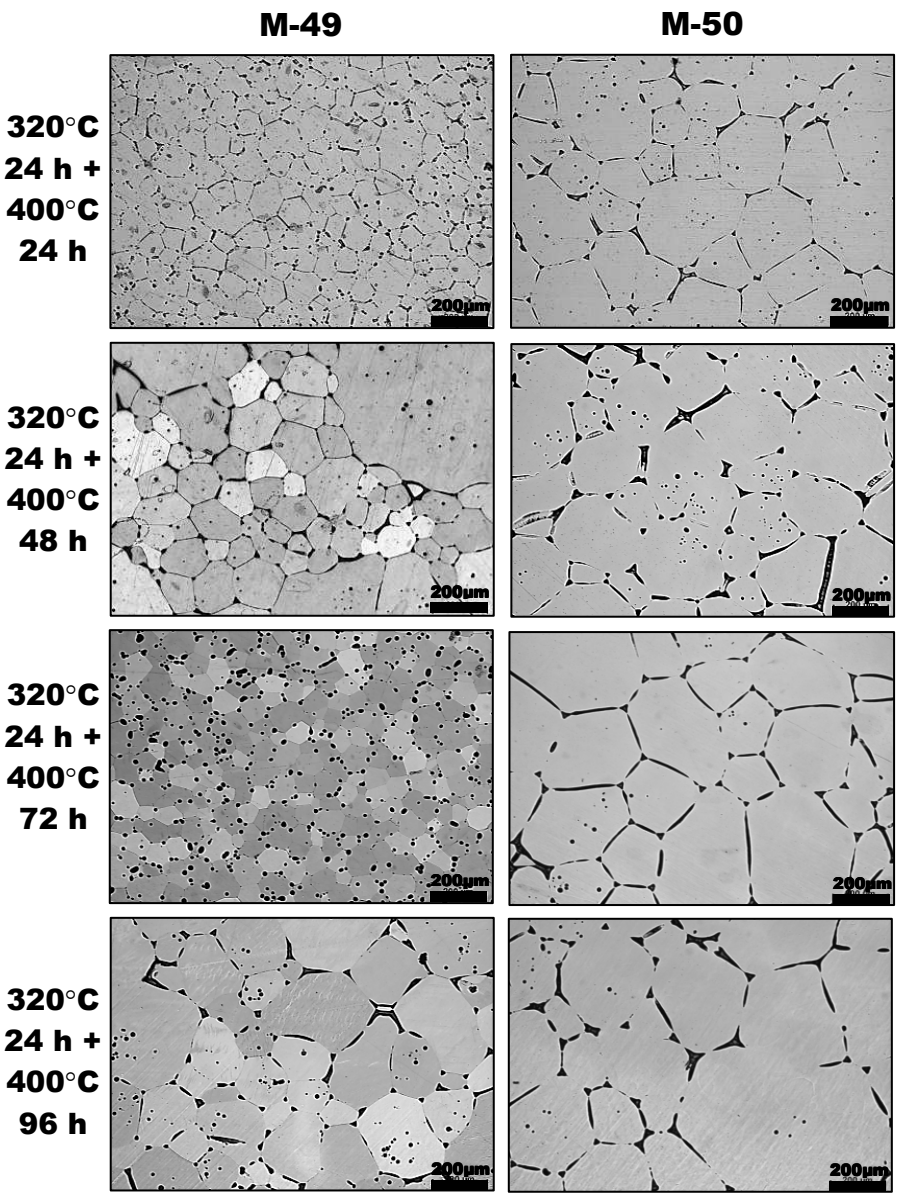

Figure 34. Optical micrographs of T4 heat treated M-49 and M-50 grain structures conducted at 320°C for 24 h and then at 400°C for 24, 48, 72, and 96 h.

Since the temperature of the second stage was reduced from 480°C to 400°C, the time needed for atom diffusion extends from just 2 h to 48 h. This holds true when analyzing the average grain diameter (Figure 36a).

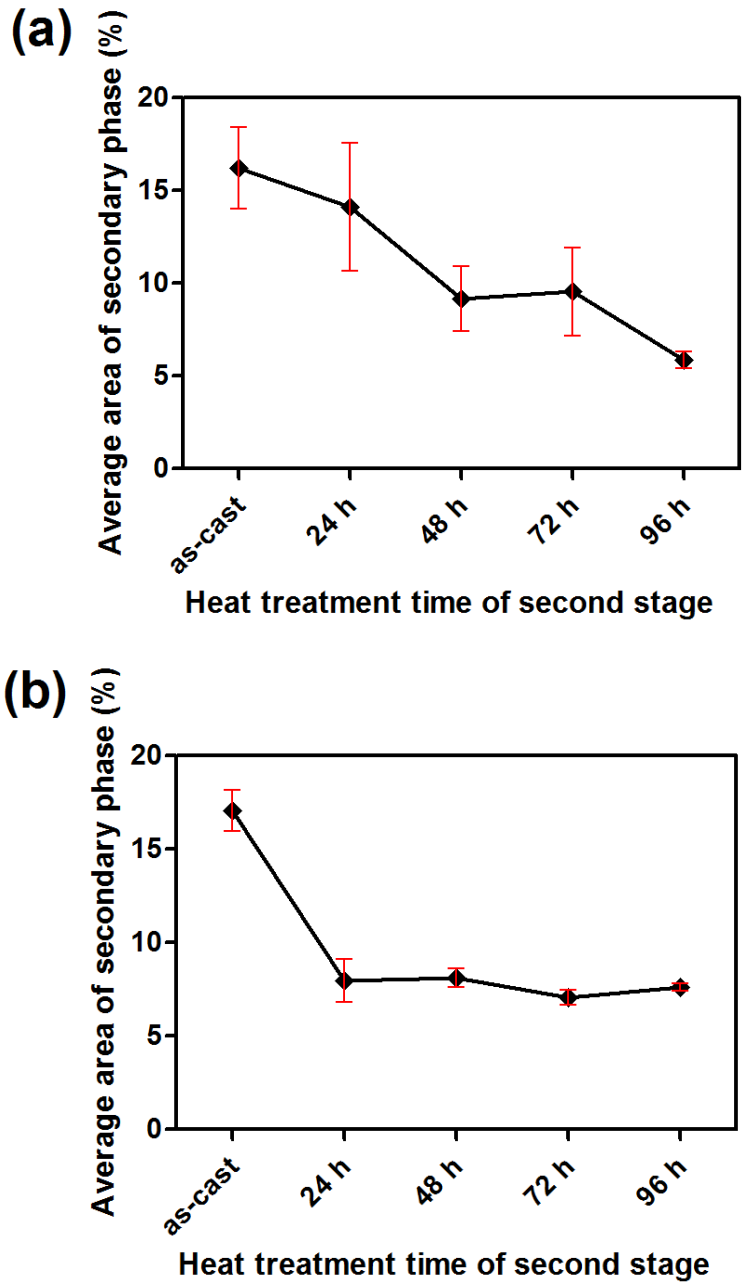

Figure 35. Average area of intermetallic phase of heat treated (320°C 24 h + 400°C *x*h) samples compared to the as-cast counterpart taken from OM images at 5x (n = 3): a) M-49 and b) M-50.

The as-cast M-49 samples and the 24 h heat treated samples has an average grain size of 61.0 ± 30.5 µm and 72.55 ± 34.2 µm, respectively. It is not until the treatment time reaches 48 h you see a significant increase in the average grain size (165.1 ± 95.6 µm). Regardless, the

extended treatment time of 48 h at 400°C is effective in dissolving the constituent phases into the primary matrix, but it also promotes grain growth. When studying the effect of the heat treatment times on the area of the secondary phase, statistical analysis discovers that between the 24 h and 48 h treatment, there is no significant change. This holds true for 24 h compared to the 72 h treatment as well. It is not until you compare the 24 h to the 96 h treatment time there is a significant difference in the reduction of secondary phase.

The effect of treatment time on the average grain size of the M-49 alloy does not show a consistent trend. At the 72 h treatment time mark, there is a significant reduction of the average grain diameter compared to the 48 h samples to 70.6 ± 35.4 µm, which is close to that of the as-cast M-49 samples. It can be seen that even though there isn't a significant change in the amount of secondary phase between the 48 h and 72 h samples, from the OM images you can see a significant morphological change in that the secondary phase along the grain boundaries have a fine and consistent in size type of quality in their appearance suggesting grain refinement. Yet, this refinement continues as the treatment time increases to 96 h where the diffusion of the secondary phase causes grain assimilation which explains the increase in grain size and secondary phase area reduction of the 96 h heat treated samples. This inconsistent grain size trend may be attributed to error in sampling. More specifically the specimen used for microstructural analysis of the bulk M-49 alloy could have been extracted from an area within the bulk alloy that was inconsistent with specimens taken from other alloys. Therefore sampling needs to be more standardized in the future to promote consistency and reduce error.

For the M-50 alloy, the heat treatment process reduces the area of intermetallic phase 10 percentage points compared to the as-cast samples (Figure 35b).

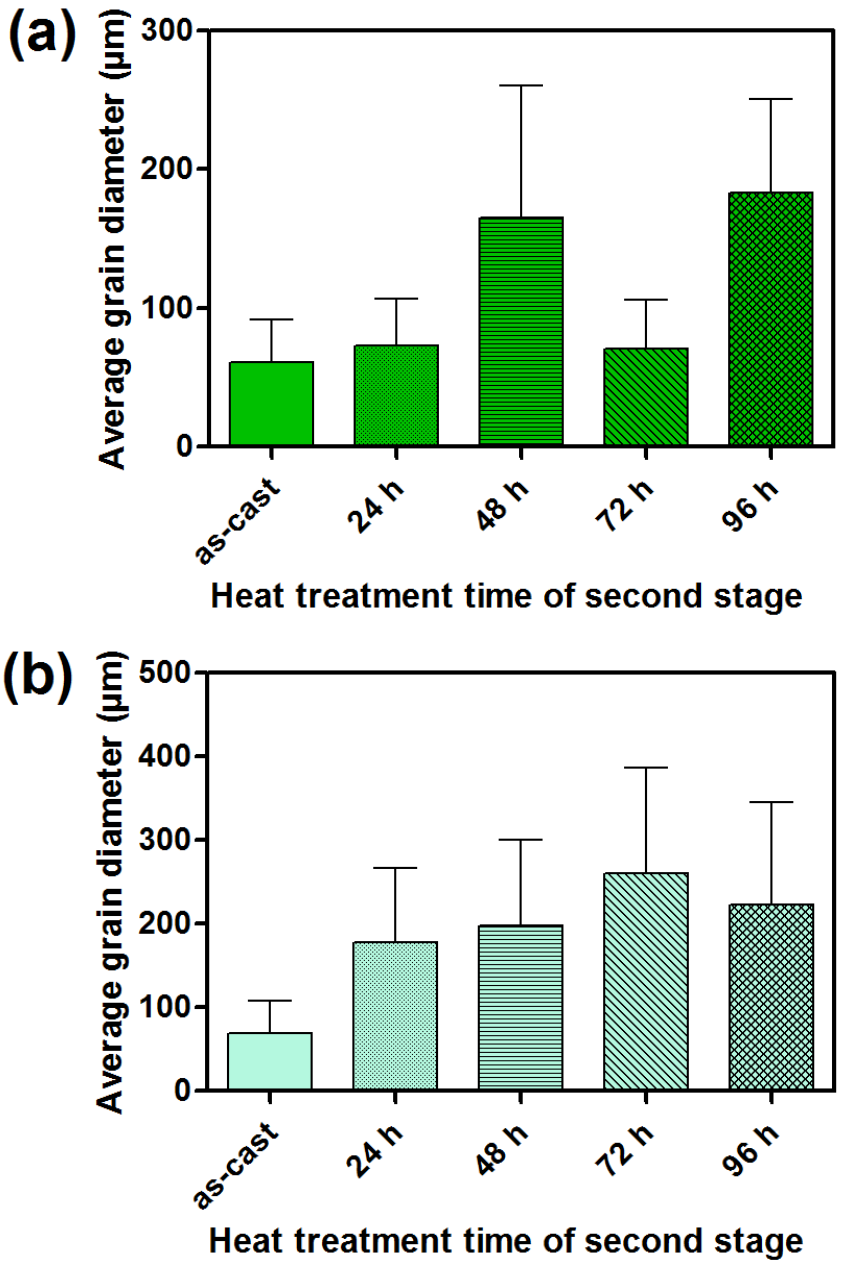

Figure 36. Average grain diameter in µm of heat treated (320°C 24 h + 400°C *x*h) samples compared with as-cast samples determined from the ASTM line intercept method: a) M-49 and b) M-50.

After the initial reduction of intermetallic phases, the reduction levels off with no significant variation between the heat-treated means following an extended heat treatment time.

Additionally, as the secondary phase diffuse into the Mg matrix once heat treatment is applied, the grain size consequently increases as the grain boundaries disappear which cause grain assimilation as seen in the M-49 heat treated samples (Figure 36b).

4.1.2.2.3 Comparison between heat treatment trial I and II. To get a better understanding of how the first heat treatment trial (300°C 20 h + 480°C *x*h) compares with the second heat treatment trial (320°C 24 h + 400°C *x*h), the secondary area and grain diameter of each trial was compared by their consecutive time points for the M-50 alloy (Figure 37). The two-way ANOVA analysis for the average area of secondary phase determined that there is a no significant difference between the two trials [$F(3, 16) = 0.83$, $p = 0.4947$]. The means for last time point for each trial only had a difference of 0.59 percentage point. Additionally, the average grain diameter for each trial shows an increase in grain size compared to the as-cast samples. The two-way ANOVA also discovered that the difference between the means of the grain diameter for both trials are not significant [$F(3, 32) = 0.44$, $p = 0.7249$].

For the M-50 alloy, the lack of significant statistical difference between both treatment trials indicates that the treatment parameters did not create a meaningfully different alloy in terms of the microstructure which will ultimately create different corrosion and mechanical properties. There is a need for further optimization of the treatment parameters.

4.1.2.2.4 Heat treatment trial III. Consequently, a third T4 solution treatment trial was considered for both the M-49 and M-50 alloys. The first stage of the treatment process consisted of a temperature and time of 300°C for 48 h. The time of the first stage was increased from 24 h to 48 h to further bolster the grain boundaries to prevent melting during the higher temperature parameters experienced during the second stage which will help maintain grain size. The second stage consisted of a temperature of 450°C for 72, 96, 120, and 144 h. The second stage

temperature was increased from 400°C to 450°C because of the need to create more refined grain structure among secondary phase.

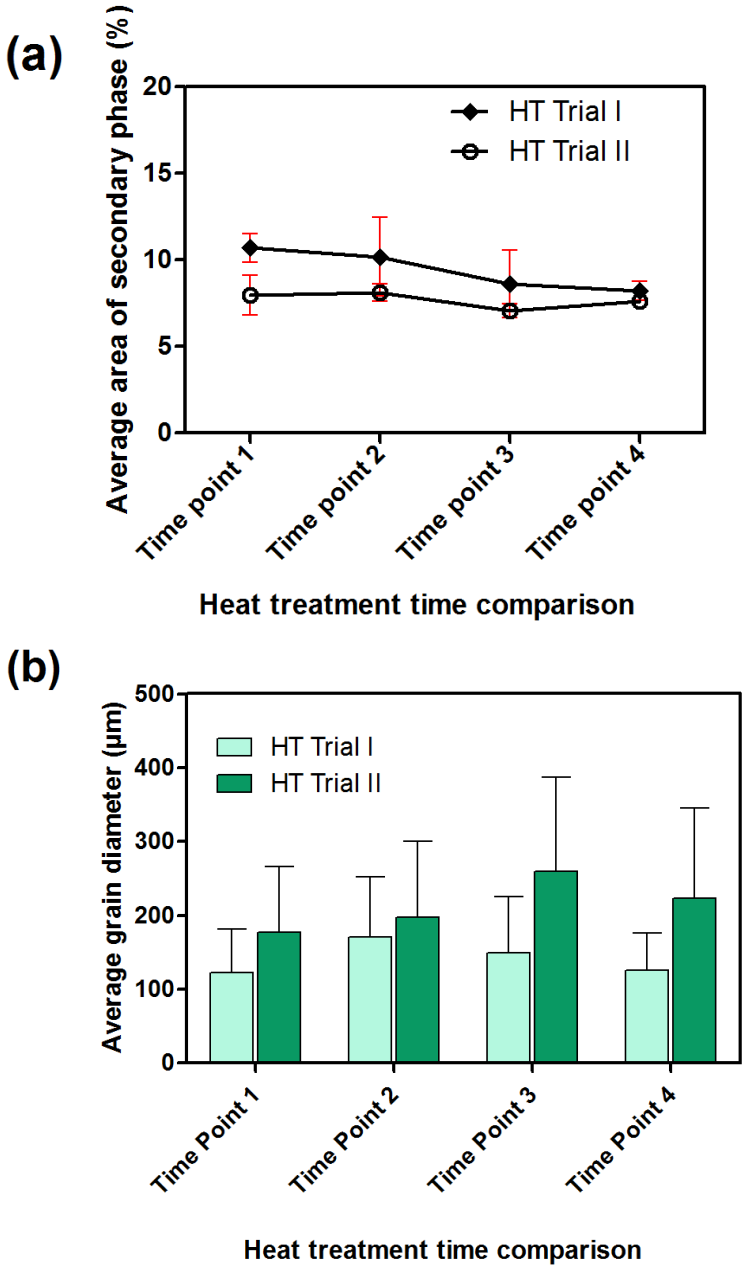

Figure 37. Comparison between heat treatment trial I (300°C 20 h + 480°C *x*h) vs. heat treatment trial II (320°C 20 h + 400°C *x*h) which were conducted on the M-50 alloy.

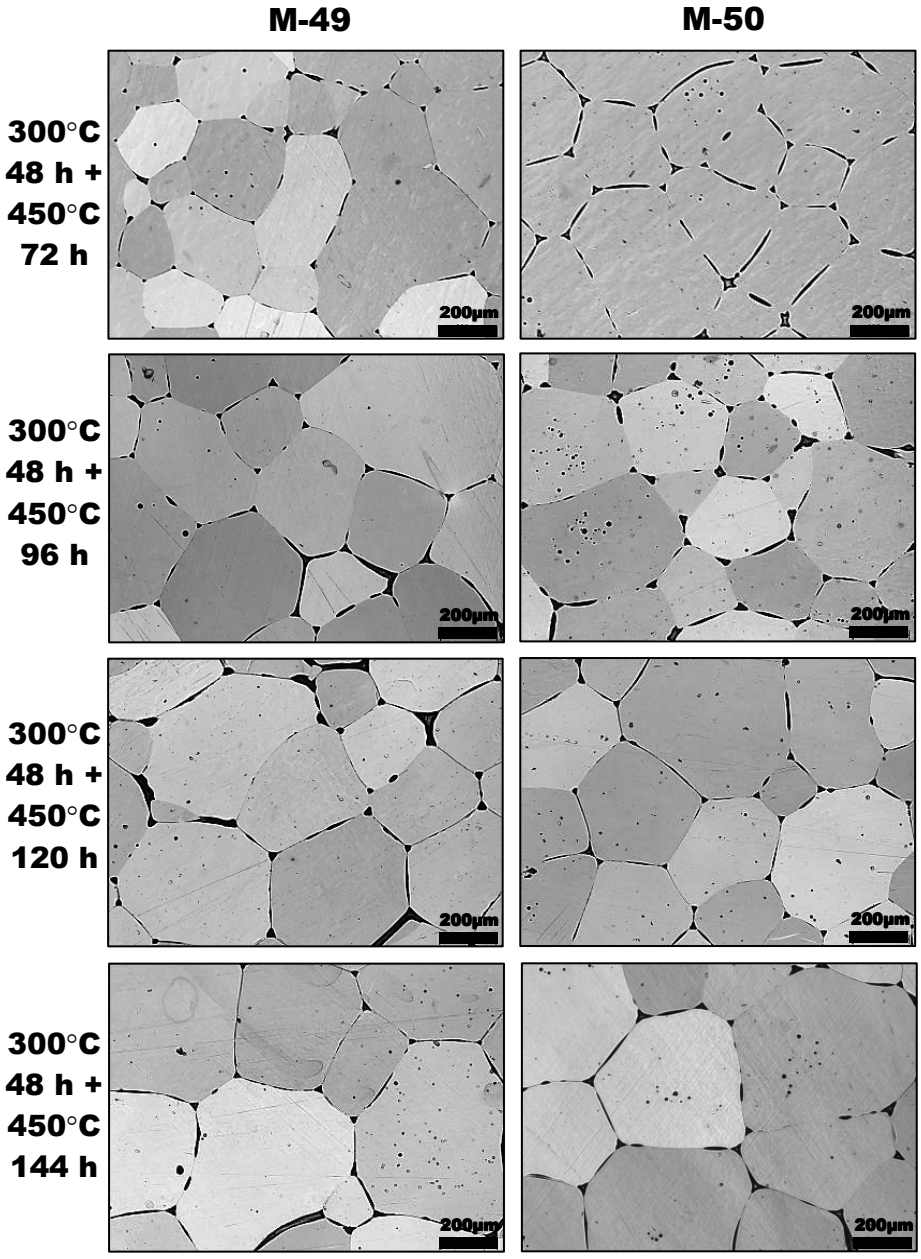

Figure 38. Optical micrographs of T4 heat treated M-49 and M-50 grain structures conducted at 300°C for 48 h and then at 450°C for 72, 96, 120, and 144 h.

Figure 38 shows the optical micrographs of the grain structures of the M-49 and M-50 samples subjected to the third T4 solution treatment trial. As seen in the as-cast and heat treated alloys previous discussed in this study, the grain morphology of both alloys is observed to be

typically hexagonal globular in nature. Furthermore, the treatment conditions were effective in reducing the secondary phase through diffusion for both alloys into the Mg matrix but there is still no significant difference in the means when comparing the treatment times (Figure 39).

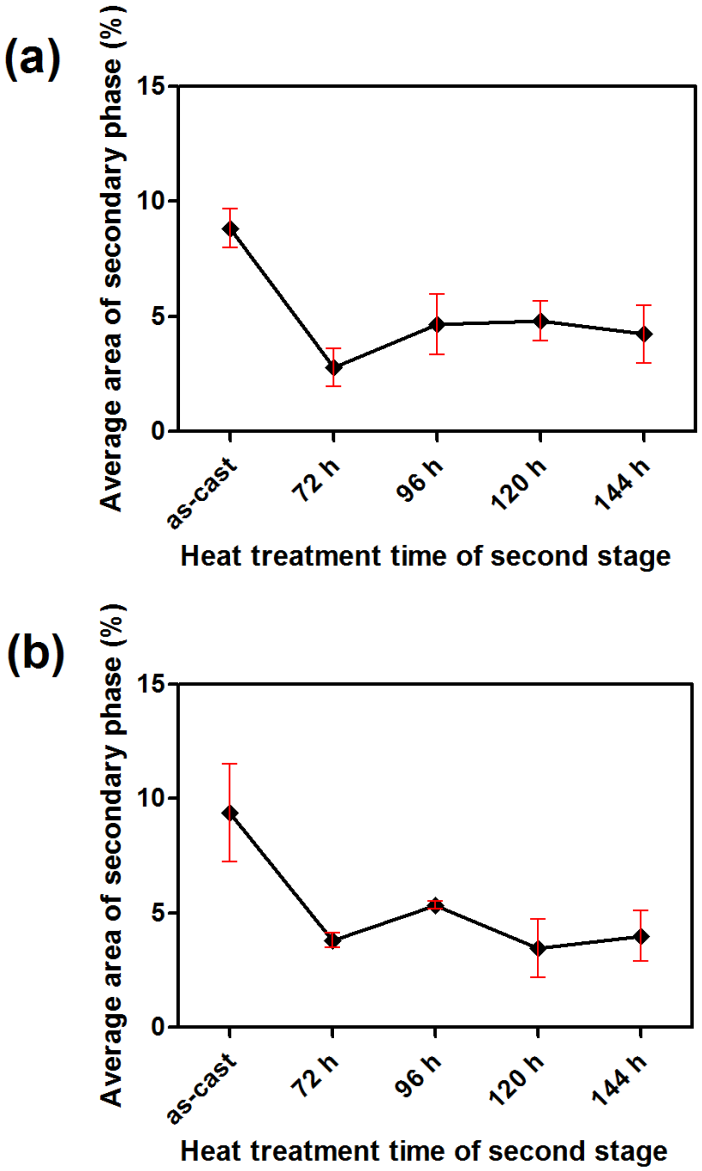

Figure 39. Average area of intermetallic phase of as-cast and heat treated (300°C 48 h + 450°C *x*h) samples taken from OM images at 10x (n = 3): a) M-49 and b) M-50.

Again, the extended heat treatment time significantly increased the average grain size for both alloys compared to the as-cast samples (Figure 40). There is no difference in grain diameter between the treatment times as well.

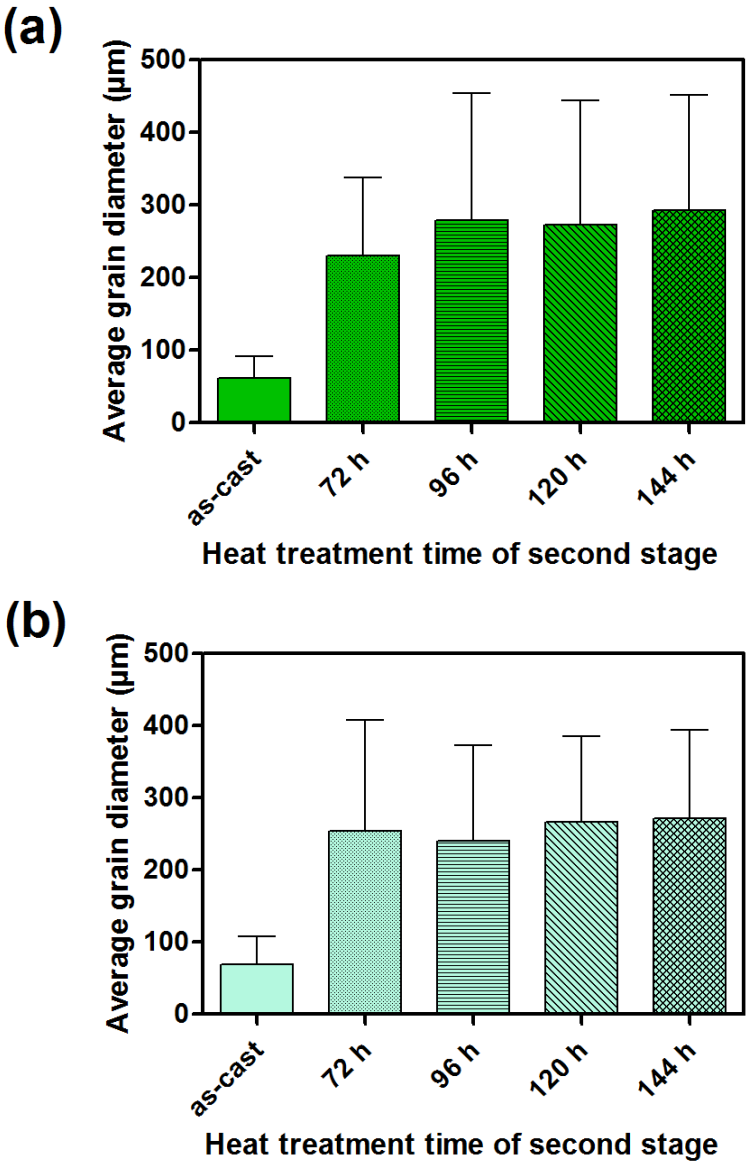

Figure 40. Average grain diameter of heat treated (300°C 48 h + 450°C *x*h) samples compared with as-cast samples determined from the ASTM line intercept method: a) M-49 and b) M-50.

Ultimately all three heat treatment trials were effective in diffusing the solute atoms into the primary matrix based on the area of secondary phases observed on the OM micrographs.

However, this diffusion caused grain integration which increased grain size. The larger grain size is considered to be harmful to the corrosion resistance of metallic alloys. Lower corrosion resistance can have an effect on the mechanical integrity of biomaterials designed for medical applications. Only two heat treatment conditions were able to maintain grain size compared to its as-cast counterparts which were the 320°C 24 h + 400°C 24 h and the 320°C 24 h + 400°C 72 h M-49 samples.

4.1.3 As-cast and heat treated MgZnCa−RE alloys. The microstructures of the as-cast and heat treated Mg−2.0Zn−0.3Ca−2.0RE alloys are summarized in Figure 41. The as-cast grain morphology consisted of a rosette-like structure composed of dendrites of α-Mg matrix separated by interdendritic phases. By EDS spectra analysis, the typical composition of secondary phase for the as-cast alloy is determined to be approximately (mass fraction, %) 45.2Mg24.8Zn15.5Nd9.6Gd corresponding to the molar composition of $Mg_{74.8}Zn_{15.2}Nd_{4.3}Gd_{4.2}$.

The double stage heat treatment process was conducted at 400°C for 20 h and then 500°C for 2, 4, 6, 8 h. The heat treatment process changed the grain morphology to a more refined hexagonal globular structure. It can be observed that there is no change in the grain morphology between the different heat treatment conditions. The secondary phases significantly dissolve into the Mg matrix as a result of the heat treatment conditioning. Consequently, the heat treatment created a single phase type of microstructure.

There is a significant 5 point percentage reduction in the average area of secondary phase between the as-cast and the 400°C 20 h + 500°C 2 h condition (Figure 42a). The final heat treatment condition at 8 h dissolves the secondary phase down to 1.3% of the area. The heat treatment conditions were considerably effective in dissolving the solute elements as seen by the

immediate effect of the lower treatment time on the reduction of the amount of secondary phase along the grain boundaries and within the Mg matrix.

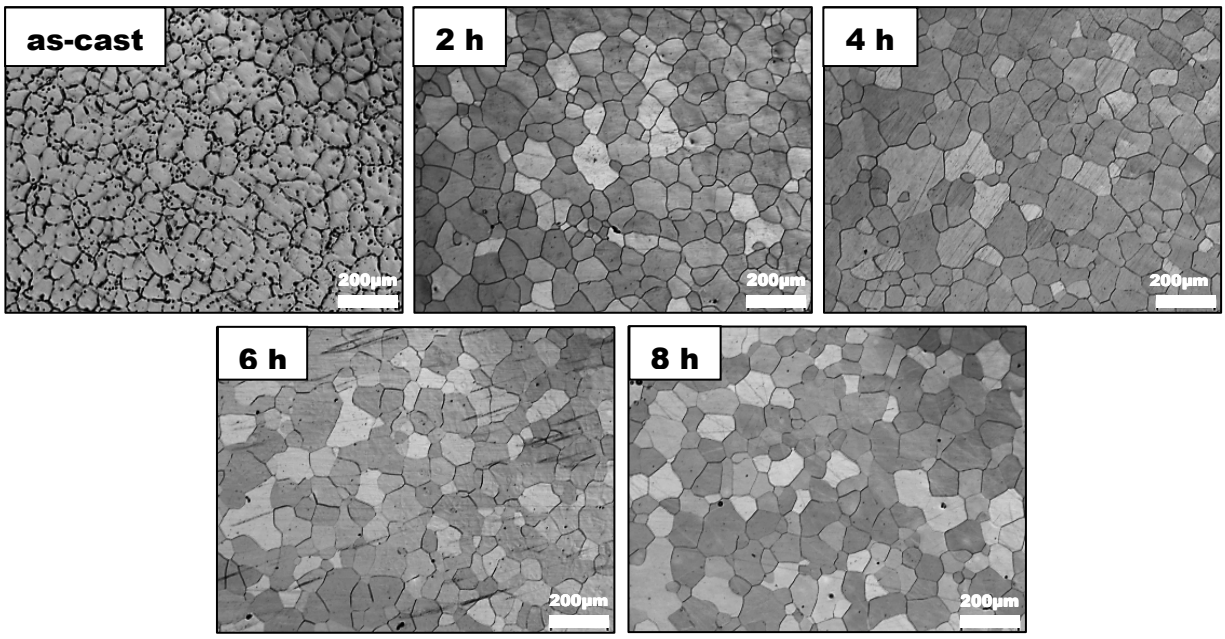

Figure 41. Optical micrographs of MgZnCa−RE alloy grain structures in the as-cast condition and the heat treated conditions at 400°C for 20 h and then 500°C for 2, 4, 6, and 8 h.

This is due to the normalized activation energy required for material diffusion. The activation energy of rare earth metals is even lower than that of the HCP and FCC type structures (Figure 58b, Appendix). Consequently, the dissolution of solute atoms within the Mg matrix of the MgZnCa−RE alloy in this study was able to be fulfilled at the relatively short solution time and solution temperature.

It can be seen that the REEs have a grain refining effect on the Mg−2.0Zn−0.3Ca alloy since average grain diameter of the as-cast MgZnCa−RE alloy (32.6±13.9 µm) in this study is considerably lower than the as-cast M-48 samples (75.1±42.4 µm) with no REEs. This is in agreement with other studies which have shown that increasing the concentration of Nd and Gd in Mg alloys reduces the grain size significantly [50, 111]. Additionally, REEs plays an

important role in restricting grain growth during solution treatment which is seen in the results of this study (Figure 42b).

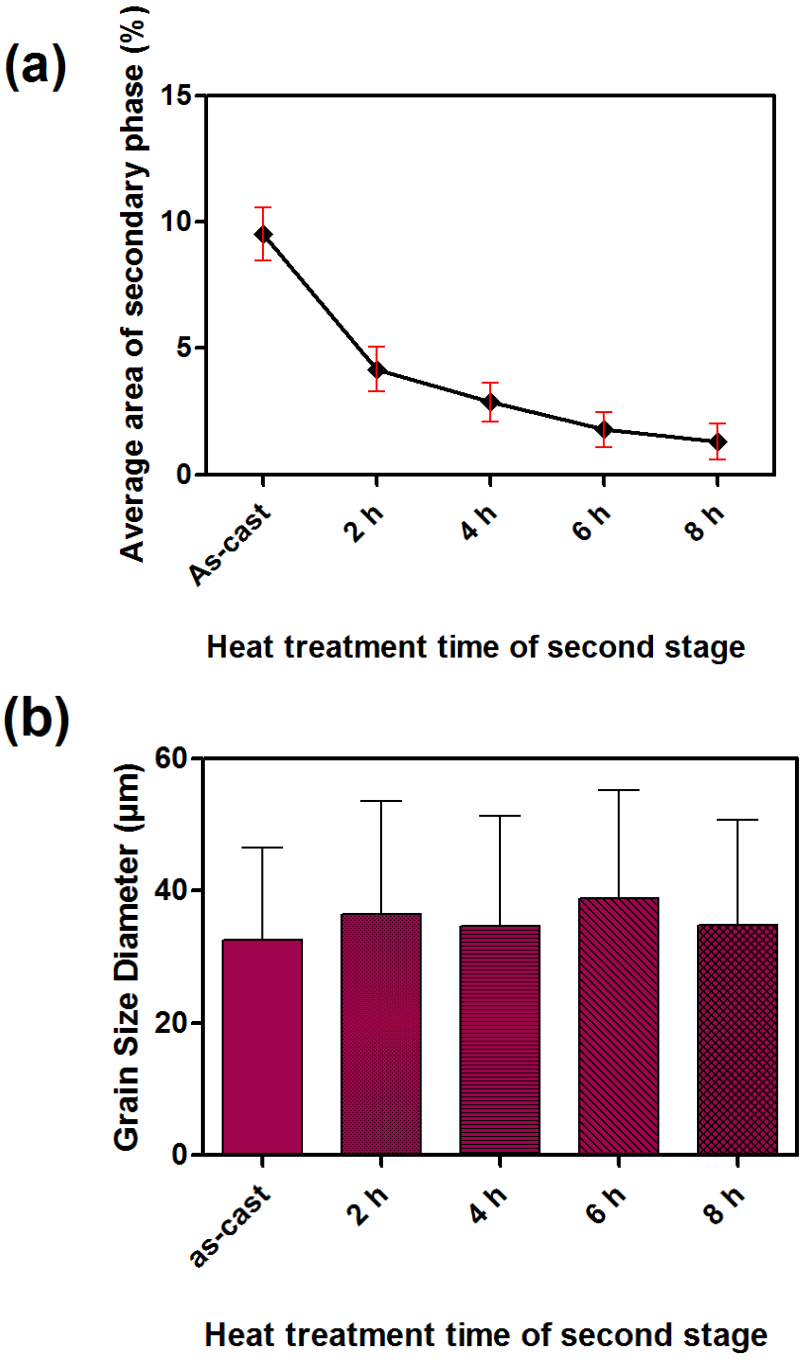

Figure 42. Average area of secondary phase (a) and average grain size diameter (b) of the as-cast and heat treated MgZnCa−RE alloy.

It is determined in this study that there is no significant difference in the average grain size means of the heat treated MgZnCa−RE alloys compared to the as-cast samples. Ning *et al.* [111] explains that the precipitation of Nd from the Mg matrix during solution treatment is distributed within and along the grain boundaries which act as an effective barrier for grain integration during heat treatment. Furthermore, it is explained that grain growth occurs at low Nd additions (0.21%) after heat treatment, while higher Nd addition alloys only had moderate increase in grain size. It can be concluded that the T4 solution treatment conducted on the MgZnCa−RE alloy was successful based on the grain restriction behavior exhibited in the heat treated MgZnCa−RE alloys in this study coupled with the successful dissolution of solute atoms in the Mg matrix. According to the microstructure and grain structure assessment in this study, the MgZnCa−RE has great potential of being a successful biomaterial.

4.2 Mechanical Properties

For bone implant, mechanical integrity is a vital component of the implant material. Figure 43 shows the tensile test results at room temperature of selected investigated alloys. The alloys chosen to investigate the mechanical properties, based on tensile stress, of the as-cast Mg−*x*Zn−0.3Ca system in tension were the M-46 (Zn = 0.5%), M-48 (Zn = 2.0%), M-50 (Zn = 4.0%), and M-52 (Zn = 6.0%) samples. The as-cast MgZnCa−RE alloy was studied in tension as well.

4.2.1 Mechanical property assessment in tension. It can be seen in Figure 43a, that there is a slight increase in the elastic modulus of the Mg−*x*Zn−0.3Ca samples as the Zn content increased. However, for all samples, including the MgZnCa−RE sample, it was determined that the moduli, which ranged from 37-47 GPa, showed no significant difference. This range in modulus values is in agreement with previous studies that determined that in general, the elastic

modulus of Mg alloys range from 41-45 GPa, which is close to that of human femur bone [12]. As a result, it can be concluded that the experimental alloys in this study will be able to minimize or reduce the stress-shield phenomena, in tension, as Mg bone implants, which exists in current metallic implants made of SS or Ti alloys.

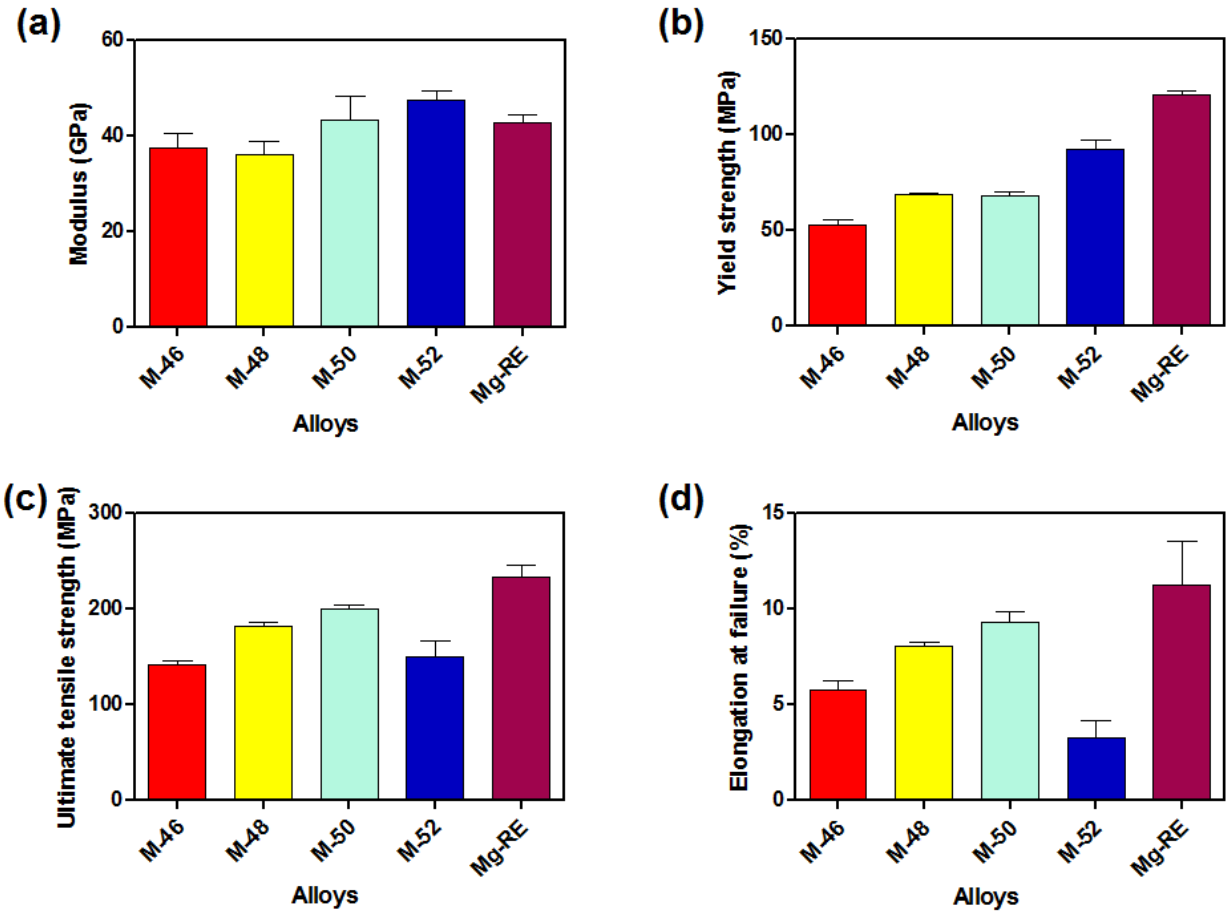

Figure 43. Mechanical properties of Mg-based alloys produced in the study in tension: a) modulus (GPa), b) yield strength (MPa), c) ultimate tensile strength (MPa), d) elongation at failure (%).

In terms of the yield strength, a similar trend is seen in which the yield strength of the Mg−*x*Zn−0.3Ca system increases from 52.8 MPa (M-46) to 92.0 MPa (M-52) as Zn content increases. This trend in yield strength behavior is also seen in the ultimate tensile strength (UTS)

and the elongation at failure (EL) values in terms of the increase in UTS and EL values as a function of the increase of Zn content. This occurrence is in agreement with other studies which concluded that the tensile mechanical integrity of the Mg−Zn−Ca system increased significantly by the addition of Zn element [25].

However, it can be observed for the Mg−*x*Zn−0.3Ca samples that when the Zn content reached 4.0 wt.%, the UTS and EL properties reached its peak values of 199.1 MPa and 9.3% respectively, which was similarly observed by other studies in terms of reaching a peak value. When Zn content exceeds more than 4.0 wt.%, in the solidification process, the Zn atom would be rejected by the α-Mg and enhanced in the residual liquid in which often cause the formation of eutectic structures and micro-porosity [71]. This may give insight into the reduction of UTS and EL values of the M-52 sample.

4.2.2 Mechanical property assessment in compression. Figure 44 shows the compressive test results at room temperature of selected investigated alloys compared with 99.97% pure Mg. The alloys chosen to investigate the mechanical properties of the Mg−*x*Zn−0.3Ca system in compression were the M-47 (Zn = 1.0%), M-49 (Zn = 3.0%), M-51 (Zn = 5.0%), and M-53 (Zn = 10.0%) samples. The results regarding the compressive mechanical properties follow a similar trend to the results obtained in tension.

4.2.3 Effects of Zn addition on the mechanical properties. In general, the experimental alloys have very good mechanical properties. Adding alloy elements to pure Mg changes the mechanical properties to more robust values. Good mechanical properties are achieved by solid solution strengthening based on the relatively high solid solubility of Zn in Mg at high temperatures. Additionally, in the Mg−Zn−Ca system, the presences of the $Ca_2Mg_6Zn_3$ and $Ca_2Mg_5Zn_{13}$ phases could enhance the strength and toughness of Mg [71, 112, 113]. Figure 28

describes the presences of the aforementioned $Ca_2Mg_6Zn_3$ phase, which increased in occurrence with the addition of Zn, which provided the increase in strength seen in the present study.

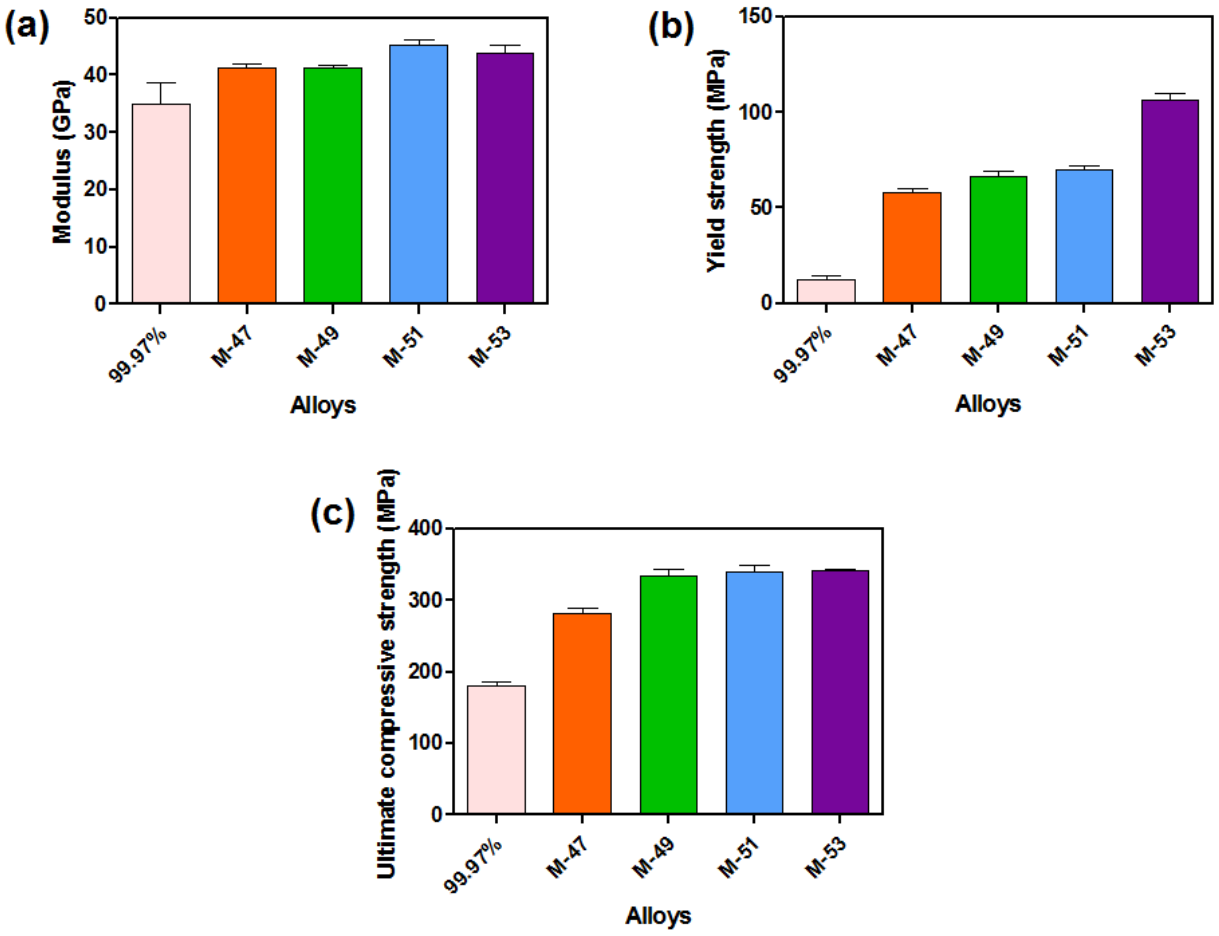

Figure 44. Mechanical properties of Mg-based alloys produced in this study in compression: a) modulus (GPa), b) yield strength (MPa), c) ultimate tensile strength (MPa).

As discussed in chapter 2, the stacking fault energy of Mg alloys decreased with high content of solid solution Zn [44]. Consequently, extended dislocations are broadened which can result in higher difficulty in the initiation of non-basal slip. As a result, better mechanical strengths including high ductility up to 4% Zn is observed which is seen in this study. Therefore, the present work showed that adding Zn to the Mg−0.3Ca alloy marked an increase of the

mechanical properties. But Zn content exceeding 4.0 wt.% compromised the microstructure causing a decline in the mechanical properties of the Mg−*x*Zn−0.3Ca alloy system.

4.2.4 Effects of REEs on the mechanical properties. The MgZnCa−RE sample has the highest yield strength, ultimate tensile strength, and elongation at failure values, compared to the Mg−*x*Zn−0.3Ca alloys, at 121.0 MPa, 232.7 MPa, and 11.3% respectively. This is in agreement with studies that found that RE-containing Mg alloys are stronger than AZ91 alloy [114]. More specifically, the addition of Gd and Nd in Mg improves the tensile and compression strengths [50, 111]. The secondary phase disperse inside the grains can effectively block dislocation slip within grains, combined with proper grain size, can improve the creep resistance and ultimately the mechanical properties of RE-containing Mg alloys. The secondary phase ($Mg_{74.8}Zn_{15.2}Nd_{4.3}Gd_{4.2}$) detected inside the grain boundaries in this study, which was effective in maintaining the grain size during heat treatment processing, could have an effect on hindering the slip dislocation in the MgZnCa−RE alloys.

4.3 Immersion Corrosion Assessment

4.3.1 MgZnCa alloys.

4.3.1.1 Corrosion rates of as-cast MgZnCa samples in 0.9% NaCl. The corrosion rates (mm/year) of the as-cast Mg−*x*Zn−0.3Ca alloys based on a 10 day immersion in 0.9% NaCl solution is described in Figure 45. A 99.97% pure Mg control alloy was used for all immersion tests reported in this study. When comparing the experimental alloys to the control, the M-46 (0.5 wt.% Zn) and M-47 (1.0 wt.%) samples had lower corrosion rates at 1.6 and 1.4 mm/year respectively than the pure Mg at 2.9 mm/year. As the Zn level goes from 2.0 wt.% to 4.0 wt.% (M-48 thru M-50), the corrosion rate increases to around 4.4 mm/year. However, the one-way ANOVA determined that the M-46, M-47, M-48, M-49 and M-50 samples did not show any

statistical differences in the mean corrosion rate values. It is not until the Zn level reaches to 5.0 wt.% (M-51) that there is a significant increase in the mean.

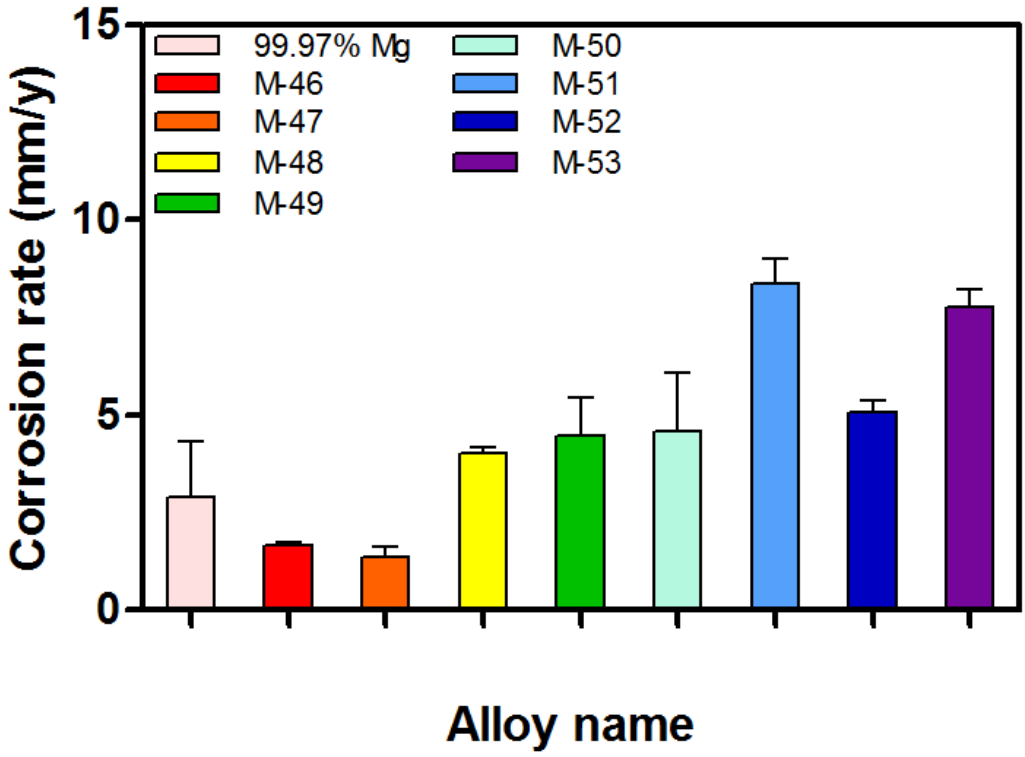

Figure 45. Average corrosion rate, in mm/year, of the as-cast Mg−*x*Zn−0.3Ca alloys in 0.9% NaCl solution after 10 days immersion.

The corrosion rate for the samples with 5.0-10 wt.% increase to around 7.1 mm/year. In terms of comparing the effects of increasing Zn content to the corrosion behavior of the Mg-0.3 wt.%Ca system, there was an initial reduction in the corrosion rate up to 1 wt.% of Zn, but the corrosion rate experienced an overall increase as the Zn content increased to 10.0 wt.%. These results are similar to Bakhsheshi-Rad *et al.* findings in which it was discovered that in the Mg−0.5Ca−xZn alloy, the addition of Zn content up to 1 wt.% increased the corrosion resistance whilst further addition of Zn up to 9% reversed the effect [103]. The reason for the reduction in corrosion behavior of the Mg−xZn−0.3Ca alloys as a function of the increased Zn content is the

formation of coarse secondary phase precipitates shown in Figure 28, which grew thicker and more profound during the solid solidification processes at higher Zn levels. This precipitation accelerated the corrosion rate due to the different electrochemical behaviors between the α-Mg and the precipitates. This difference in electrochemical behavior causes galvanic couples between the secondary phase and the Mg matrix. For the M-46 and M-47, only the primary Mg matrix could be detected which results in higher corrosion resistance and a lower corrosion rate because there are no significant galvanic coupling behaviors between different phases. As the Zn level continue to increase, the Mg_2Ca and the $Ca_2Mg_6Zn_3$ phases being to precipitate. It is suggested that the Mg_2Ca is more reactive than the $Ca_2Mg_6Zn_3$ phase and the α-Mg matrix while the $Ca_2Mg_6Zn_3$ phase is less active than the α-Mg [103]. As a result, the Mg_2Ca would corrode faster than the other two phases. Further addition of Zn results in the disappearance of the Mg_2Ca phase, therefore the $Ca_2Mg_6Zn_3$ phase acts as the cathode and α-Mg phase as the anode. The α-Mg phase cannot further support the $Ca_2Mg_6Zn_3$ phase as the Zn level increased generating higher corrosion rates.

The degradation process of Mg alloys is an electrochemical procedure, which describes the electron flow between the anode and cathode. Normally for Mg in an aqueous environment, the Mg alloy reacts with the fluids on the surface and gets dissolved in the surrounding environment. Ultimately, the local pH at the surface of the Mg increases above 10 and then an oxide layer of Mg hydroxide develops. The overall corrosion reaction is given below [115]:

$$Mg_{(s)} \rightarrow 2H_2O_{(aq)} \rightarrow Mg(OH)_{2\,(s)} + H_{2\,(g)} \qquad \text{Equation 14}$$

This overall reaction includes the following partial reactions:

$$Mg_{(s)} \rightarrow Mg^{2+}_{(aq)} + 2e^- \text{ (anodic reaction)} \qquad \text{Equation 15}$$

$$2\,H_2O_{(aq)} + 2e^- \rightarrow H_{2\,(g)} + 2OH^-_{(aq)} \text{ (cathodic reaction)} \qquad \text{Equation 16}$$

$$Mg^{2+}_{(aq)} + 2OH^{-}_{(aq)} \rightarrow Mg(OH)_{2\,(s)} \text{ (product formation)} \qquad \text{Equation 17}$$

In physiological environments, more severe corrosion occurs which forms Mg chloride and hydrogen gases that can be toxic to living cells. The following chemical equations summarize the corrosion reaction of Mg in an electrolytic physiological environment [12]:

$$Mg_{(s)} + 2H_2O \rightarrow Mg(OH)_{2\,(s)} + H_{2\,(g)} \qquad \text{Equation 18}$$

$$Mg_{(s)} + 2Cl^{-}_{(aq)} \rightarrow MgCl_2 \qquad \text{Equation 19}$$

Due to the formation of the porous $Mg(OH)_2$ layer, which attaches to the matrix, the corrosion of the specimen slows [103]. However, the presence of Cl^- in the physiological solution transforms the $Mg(OH)_2$ layer into a soluble $MgCl_2$. The breakdown of the $Mg(OH)_2$ layer promotes further dissolution of the specimen. The $MgCl_2$ dissolves into Mg^{2+} and $2Cl^-$ causing an increase in hydroxide ions near the surface of the specimen which increases the pH value of the solution.

Witte *et al.* [116] discovered that this corrosion layer promotes osteo-inductivity and osteo-conductivity and therefore the release of these ions during degradation is believed to be safe and has good biocompatibility. Bakhsheshi-Rad *et al.* [103] discovered this protective layer phenomena in their study, in which the formation of white particles in the form of closely packed needle-like crystal structures on the sample surface, was present. This was observed during the 10 day immersion test conducted in this study. Even though galvanic corrosion was observed post immersion test, a white protective film was also observed during the immersion test. The dissolution of Mg (Equation 15) and the cathodic reaction occurred at the same time due to the occurrence of galvanic corrosion accompanied by hydrogen evolution (Equation 16). The Cl^- concentration which is present in the 0.9% NaCl solution transformed the layer of $Mg(OH)_2$ into the soluble form of $MgCl_2$.

4.3.1.2 Corrosion rates of as-cast MgZnCa samples in MEMα. The same corrosion behavior was observed in the Mg−*x*Zn−0.3Ca alloys after a 10 day immersion test in Fetal Bovine Serum (FBS)-containing MEMα cell culture medium shown in Figure 46.

The main difference in the results of the MEMα cell culture solution and the 0.9% NaCl solution is that the pure Mg had a lower corrosion rate than the M-46 alloy but the one-way ANOVA determined that this difference was not significant. Additionally, the overall corrosion rates of the Mg−*x*Zn−0.3Ca alloys were reduced in the MEMα medium compared to the 0.9% NaCl results. This finding is in agreement with many publications that indicate that there is a tendency for corrosion to slow down when proteins are added to the corrosion medium irrespective of the composition of the medium [117].

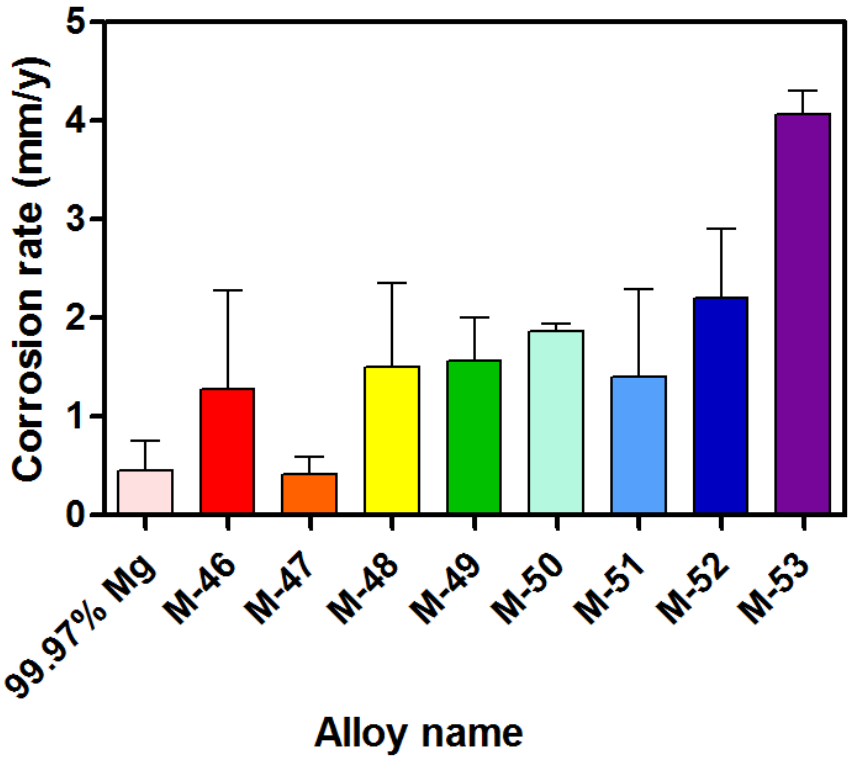

Figure 46. Average corrosion rate in mm/year of as-cast Mg−*x*Zn−0.3Ca alloys in MEMα cell culture solution.

Figure 47 shows the variation of pH values of the MEMα solution as a function of immersion duration for the Mg−*x*Zn−0.3Ca alloys. It can be observed that the pH variation for the Mg−*x*Zn−0.3Ca alloys and the pure Mg all followed a similar trend which is confirmed by the one-way ANOVA. The pH variation rate decreased as the immersion time increased. In the first 24 hours, both the pure Mg and Mg−*x*Zn−0.3Ca alloys reacted acutely with the MEMα solution. This is a function of the Mg and H_2O reacting in the MEMα solution generating OH^- and causing the pH values of the solutions to increase.

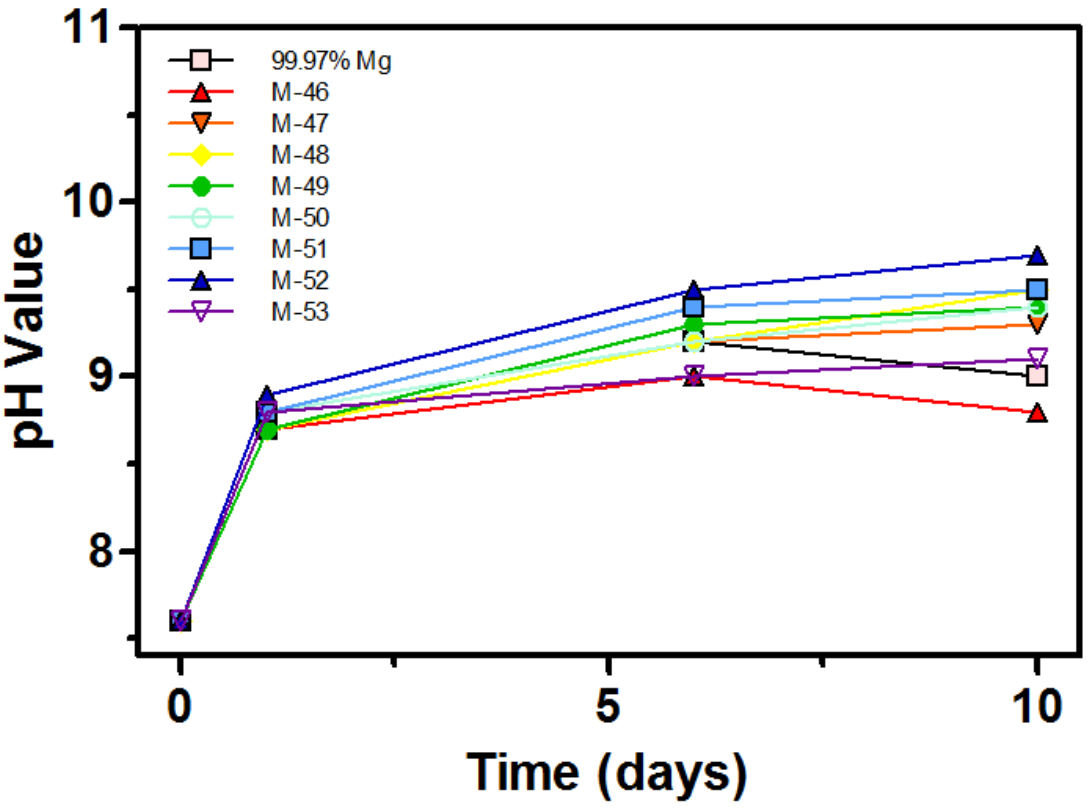

Figure 47. pH variation of MEMα cell culture solution versus the immersion testing time for as-cast Mg−*x*Zn−0.3Ca alloys.

After 24 hours immersion, all the pH values of the samples tend to stabilize around 9.3. This stabilization is important because the pH value around implants was also reported to a

crucial factor that can influence osteoblast differentiation and proliferation [118-120]. Previous studies have shown how the pH affects bone metabolism in that during metabolic acidosis (pH < 7.35) the activity of osteoblasts declines, whereas during metabolic alkalosis (pH > 7.45) osteoblast activity increases [119-125]. The pH variations of the MEMα solution (Figure 47) suggest that the experimental alloys can retain an environment that is conducive to healthy bone activity.

4.3.1.3 Corrosion rates of heat treated MgZnCa samples in 0.9% NaCl. Figure 48 presents the average corrosion rates of the heated treated M-50 samples compared to its as-cast counterpart and pure 99.97% Mg in the 0.9% NaCl solution for 10 days. The corrosion rate of the M-50 alloy experienced a significant increase as a function of the heat treatment processing. The different electrochemical behavior experienced between the α-Mg and the intermetallic secondary phase still plays a role in the corrosion behavior but that role is altered because of the heat treatment conditioning. Figure 31 shows that most of the solute elements have been dissolved into the primary Mg matrix which caused more refinement in the grain boundaries throughout the heat treated samples.

Additionally, based on the grain size data given in Figure 33, there is a significant increase in the average grain diameter of the heat treated (300°C 20 h + 480°C *x*h) M-50 samples compared with the as-cast sample. It has been shown that grain size can have a noteworthy effect on the corrosion behavior of an alloy. Fine grain size microstructures of Mg alloys were proven to provide a more negative corrosion potential which facilitates the formation of a layer of protective corrosion products that can increase the corrosion resistance [109]. A comprehensive study on the effects of grain size on corrosion rates of metals was done by Ralston *et al.* [126] where it was determined that in the examinations of systems where low rates of corrosion occur

or systems that exhibit some level a passivity, corrosion rates decreased with grain size reduction.

Improved resistance generally is attributed to an ability of high grain boundary density surfaces to passivate more readily [127, 128]. Furthermore, Ralston suggested that the grain refinement is restricted to controlling the rate of anodic reactions and have little effect on the rate of cathodic reactions because cathodic reactions are based on electronic more than ionic conduction. This is confirmed by Hoog *et al.* studies [110] which concluded that for cast Mg, a decrease in corrosion current (i_{corr}) was a function of the decreased grain size.

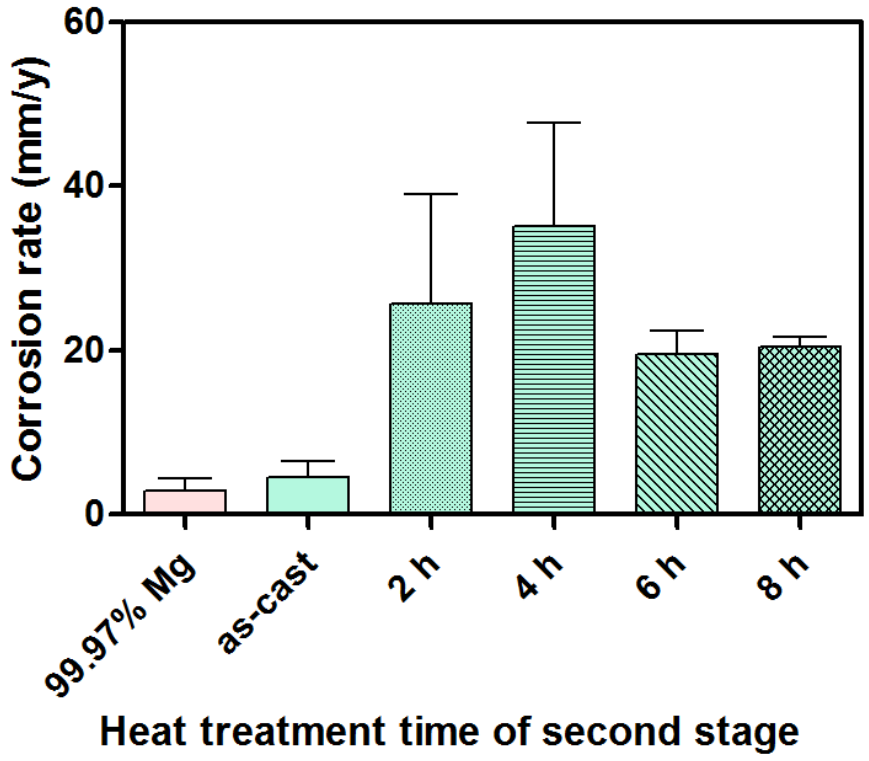

Figure 48. Average corrosion rate, in mm/y, of as-cast and heat treated M-50 alloys in 0.9% NaCl solution.

This phenomenon is confirmed in the present study. In the as-cast condition, the higher grain boundary density dictated the passivation rate on the surfaces of the as-cast

Mg−*x*Zn−0.3Ca material because of the continuous system of the secondary phase. This continuous system acts as a barrier to the aqueous environment and corrodes the Mg matrix first, but is stopped by the secondary phase barrier. The first two heat treatment parameters created holes within this barrier as a result of the dissolution of the secondary phase producing a more non-continuous system. As a result, the refinement of the grain boundary density and subsequent increase of grain boundary diameter reduced the corrosion resistance of the first two heat treated alloys. As discussed above, the $Ca_2Mg_6Zn_3$ phase acts as the cathode and α-Mg phase as the anode. This resulted in the structure of the α-Mg phase to corrode faster around the $Ca_2Mg_6Zn_3$ phase which is illustrated in Figure 49. Since the grain size increased compared to the as-cast M-50 sample, the α-Mg phase is more prevalent which means more overall corrosion and higher corrosion rates. The last two heat treatment parameters experienced a reduction in corrosion rates compared to the first two treatment parameters because the corrosion slows down since the microstructure is more of a single type phase compared to the first two parameters which makes it corrode a little more uniformly. This increased the corrosion resistance slightly of the heat treated alloys.

4.3.2 MgZnCa−RE alloys. The corrosion rates of the as-cast and heat treated MgZnCa−RE samples are shown in Figure 50. It is determined that there is no significant difference in the average corrosion rate of the as-cast MgZnCa−RE alloy compared to the 99.97% pure Mg which are 2.41 and 2.89 mm/year respectively. It can be seen that the as-cast MgZnCa−RE alloy's corrosion rate is lower than the M-48 alloy. It has been discovered by Birbilis *et al.* [51] that REEs tend to ennoble the E_{corr} values of Mg alloys because the REEs are more thermodynamically stable than the Mg and the MgZnCa−RE intermetallics themselves are resistant to corrosion.

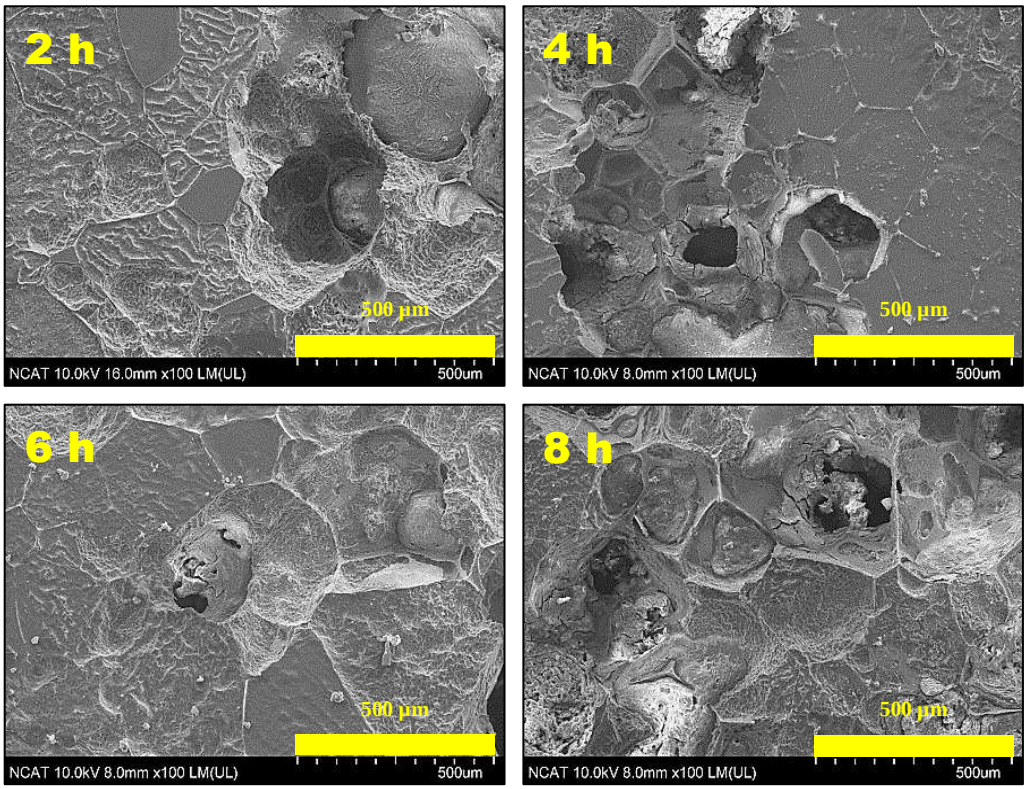

Figure 49. SEM micrographs of post immersion test surface morphology of M-50 alloys heat treated at 300°C for 20 h and then 480°C for 2, 4, 6, and 8 h.

Moreover, the presence of Gd has been shown to improve the corrosion behavior of Mg alloys up to 10 wt.% [50, 129]. However, Birbilis further explains that based on the response of individual MgZnCa−RE intermetallics; these intermetallics may increase I_{corr} overall, and therefore, owing to their electrochemical properties that differ from the matrix, can lead to galvanic corrosion. This phenomenon is seen in Figure 51a, which describes the corrosion morphology of the as-cast MgZnCa−RE sample post immersion in 0.9% NaCl solution. It can be seen that there is corrosion on the surface which appears to be mainly from the Mg matrix. There is a significant drop in the corrosion rates of the MgZnCa−RE alloys, once the heat treatment conditioning is introduced, to around 0.45 mm/year. The extension in heat treatment time beyond 2 h does not show any significant variation on the corrosion rate.

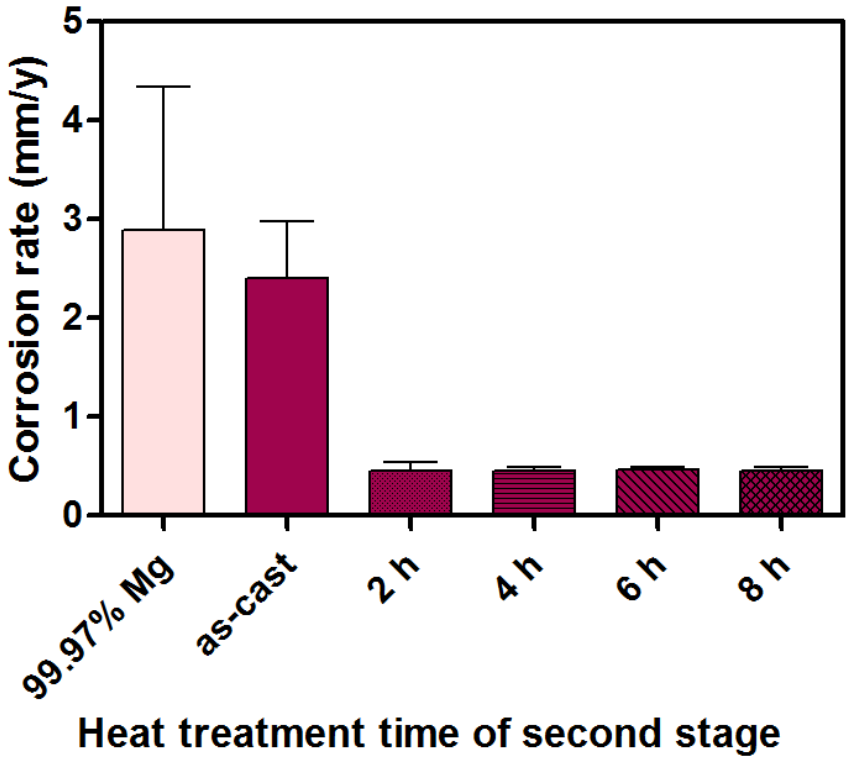

Figure 50. Average corrosion rate, in mm/year, of as-cast and heat treated MgZnCa−RE alloys in 0.9% NaCl solution.

It can be seen in Figure 42a, that the heat treatment conditions dissolve the solute elements into the primary matrix creating a single phase type of microstructure. Therefore, one aspect of the improved corrosion resistance can be attributed to the reduction of the galvanic coupling effect between the secondary phase and the primary matrix. This may explain the corrosion morphology of the MgZnCa−RE alloys post immersion in 0.9% NaCl solution, seen in Figure 51, which shows that there is more uniform corrosion on the surface of the heat treatment samples. However, the dissolution of secondary precipitates was also observed for the heat treated Mg−*x*Zn−0.3Ca alloys, but the opposite effect occurred in that the corrosion resistance decreased. Consequently, another factor must be at play in the improved corrosion resistance of the heat treated alloys.

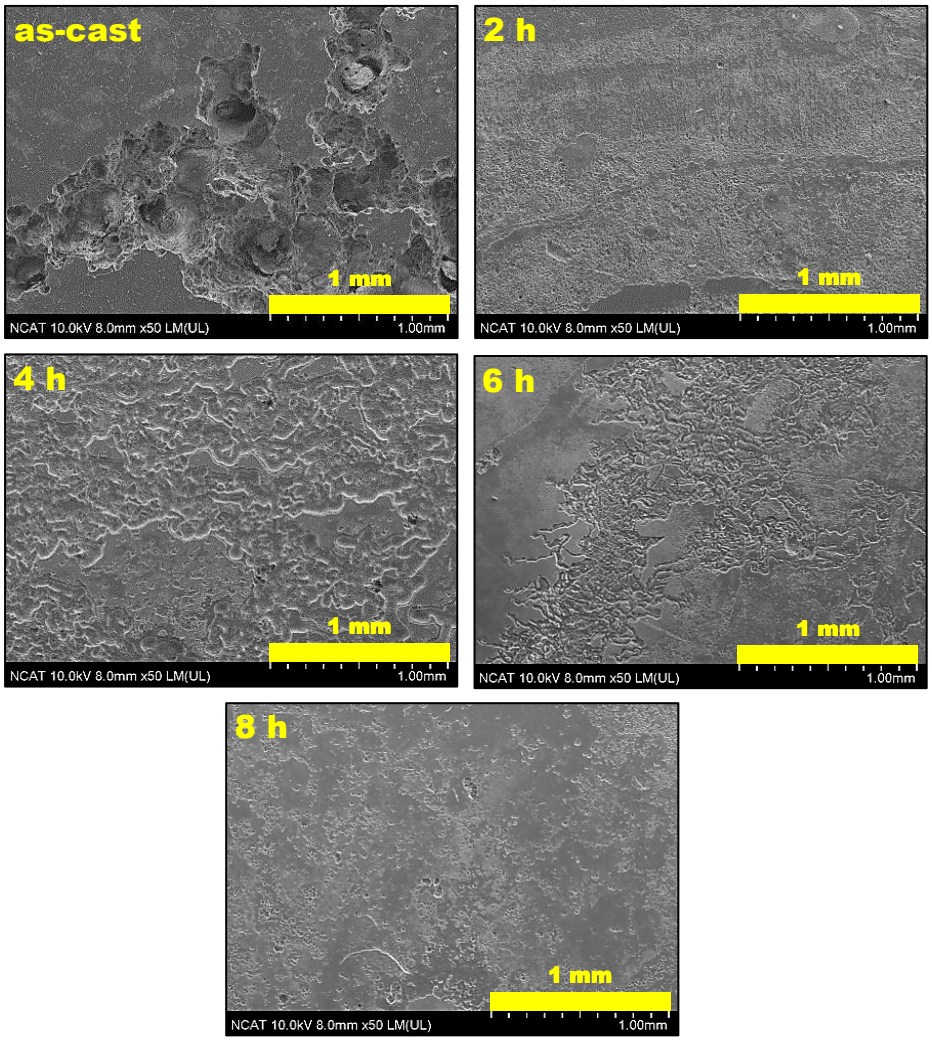

Figure 51. SEM micrographs of the surface morphology of MgZnCa−RE samples post immersion test in 0.9% NaCl solution in the as-cast and heat treated conditions.

Figure 42b illustrates the grain growth restricting qualities of the MgZnCa−RE samples after T4 heat treatment is applied. This consistency with the grain size after heat treatment is another factor in the improved corrosion resistance of the MgZnCa−RE after T4 heat treatment. Ultimately the reduction in the electrochemical coupling between of the secondary and primary phases, and the grain size restriction of the REEs within the grain boundary during the solution

treatment process served as a driving force for the increased corrosion resistance and the decreased corrosion rates of the heat treated MgZnCa−RE alloys.

4.4 Cytocompatibility Assessment

4.4.1 Live/dead assay.

4.4.1.1 Live/dead fluorescent images of MgZnCa alloys. The first study used to assess the cytocompatibility of the experimental alloys was the in-direct Live/Dead assay. The fluorescent OM images of the Live/Dead staining of the MC3T3 cells after 24 hours of incubation under M-50 alloy extracts is illustrated in Figure 52. These OM images show cells seeded with as-cast and heat treated (300°C 20 h + 480°C 2 h and 8 h) M-50 extracts of MEMα diluted from 100% to 25%. It can be seen that the majority of cells at each extract composition and dilution are alive and show healthy cell morphology. According to the ISO 10993-5: 2009 standard [130] the cytotoxic effects of the as-cast M-50 extracts at each dilution were given a grade of 0-1 (Table 8, Appendix) meaning that in terms of the qualitative images of cell morphology by the extract, the reactivity of the cells was minor. This is in agreement with Xia *et al.* [32] who determined that the as-extruded Mg−4.0Zn−0.2Ca alloy had the same grade. For the 100% 2 h heat treated M-50 extract, it can be seen that there is a reduction of cell growth compared to the lower in dilution extracts. Consequently, the ISO Grade is a 1-2. This reduction in cell density can be attributed to the corrosion behavior of the heat treated M-50 alloys seen in Figure 48. The increased corrosion rate of the 2 h treated samples compared to both the as-cast and the 8 h treated M-50 samples in the 0.9% NaCl solution suggests that there is a higher level on Mg ions in corresponding extract. This increase in ions could have reduced the cytocompatibility of the extract and consequently have a negative effect on the cell density as seen in Figure 52. The cytocompatibility of the 8 h heat treated M-50 extract at all dilutions was

given a grade of 0-1 which is similar to Sun *et al.* [44] who determined there Mg−4.0Zn−0.2Ca alloy which was homogenized at 330°C for 10 h and 400°C for 5 h had a grade between 0-1. Again the corrosion behavior of this alloy suggests that the Mg ion levels within the extract are lower than the 2 h treatment samples and is why it received a better grade.

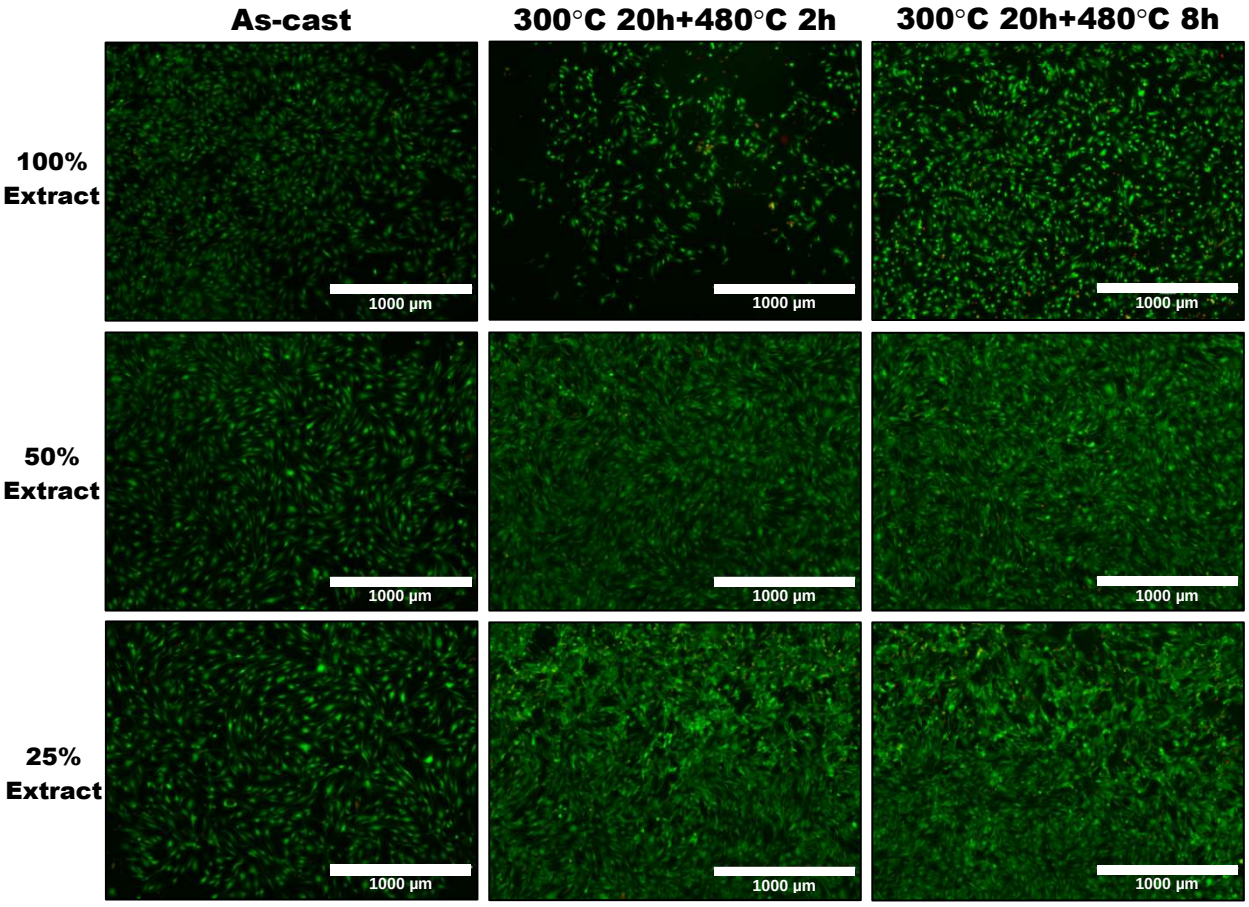

Figure 52. Fluorescent OM images of Live/Dead staining of MC3T3 osteoblast cells incubated under as-cast and heat treated M-50 alloy extract gradient of MEMα solution for 24 h.

4.4.1.2 Live/dead fluorescent images of MgZnCa−RE alloys. The fluorescent OM images of the Live/Dead staining of the MC3T3 cells incubated with MgZnCa−RE extracts are shown in Figure 53. The MEMα extracts dilutions were composed of as-cast MgZnCa−RE and heat treated (400°C 20 h + 500°C 2 h and 8 h) MgZnCa−RE alloys. As seen in the M-50 OM

Live/Dead staining images, the cells in these images all have healthy cell morphology, no reduction of cell growth, and the majority of cells fluoresce green indicating the life of the cells. As a result, the qualitative ISO Grade for each MgZnCa−RE extract is given a grade of 0.

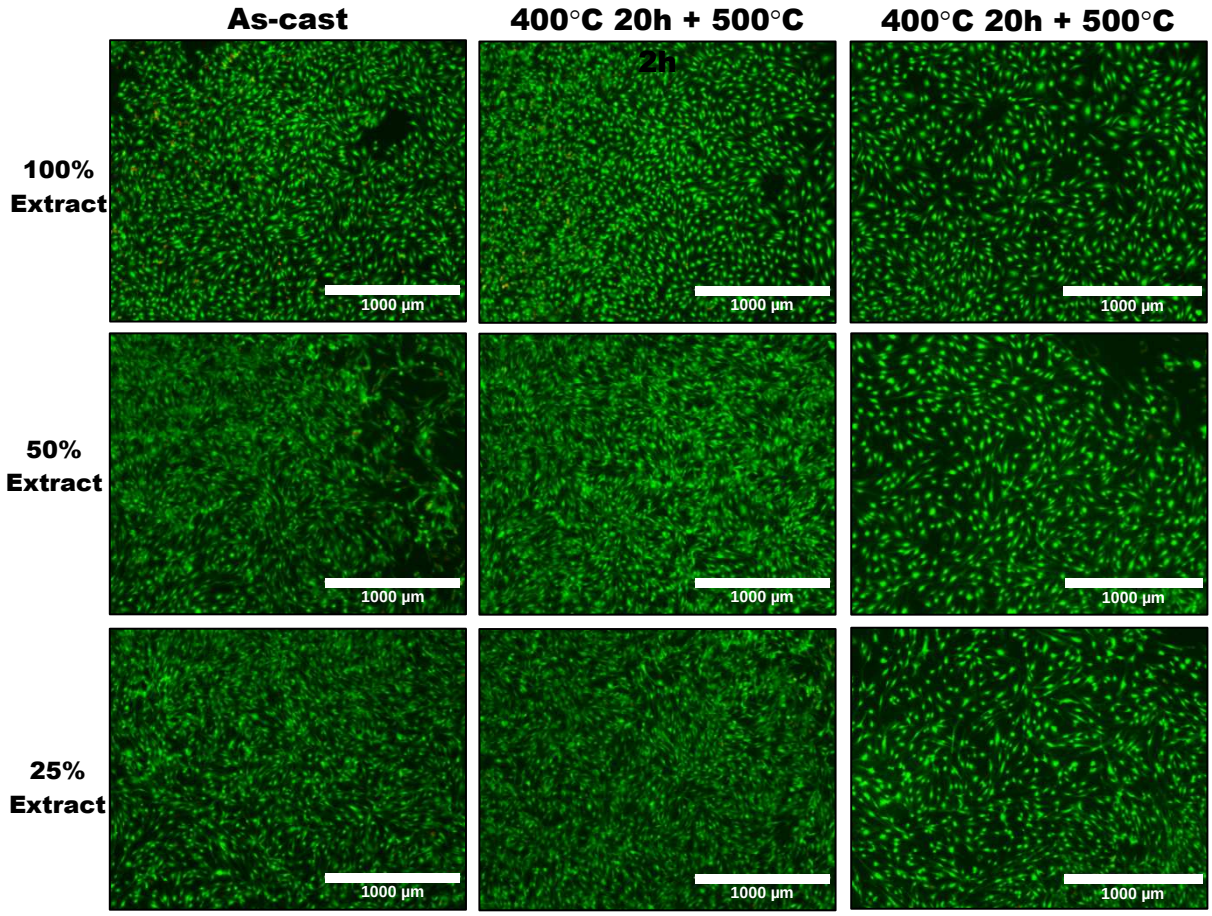

Figure 53. Fluorescent OM images of Live/Dead staining of MC3T3 osteoblast cells incubated under as-cast and heat treated MgZnCa−RE alloy extract gradient of MEMα solution for 24 h.

It can be noted that the intensity of the green fluorescence within the live cells incubated with the MgZnCa−RE extracts are more vivid than the images of the cells incubated with the M-50 extracts. This indicates that the MgZnCa−RE extracts are more cytocompatibile with the MC3T3 cells than the M-50 extracts. The positive qualitative results of this study is in agreement with Feyerabend *et al.* [49] in which he discovered the medium level RE containing elements,

which include Nd and Gd, show better cytotoxic effects than light level RE elements when looking at viability of macrophages, osteoblast-like cells and stem cells exposed to different REEs.

4.4.1.3 Cell coverage based on live fluorescent images. The corresponding average area of live cell coverage based on the fluorescent OM Live/Dead images was determined and shown in Figure 54. For the cells incubated with M-50 extracts (Figure 54a), the two-way ANOVA determined that extract composition has a significant effect on the results at the $p < 0.05$ level [$F(2, 24) = 4.83$, $p = 0.0173$]. Additionally, it was determined that the extract dilution was even more significant effect than the extract composition on the results at the $p < 0.05$ level [$F(3, 24) = 27.28$, $p < 0.0001$]. For the 100% concentrated as-cast M-50 extract, there was a significant reduction ($P < 0.01$) in the live cell coverage compared to the negative control. This reduction was more than 30% of the negative control mean and therefore it is concluded that the 100% as-cast M-50 extract has a cytotoxic effect on the MC3T3 cells according to the ISO standard [130]. As the extract dilution increases, the cell coverage increases, but is still lower than the control. This indicates that the as-cast M-50 alloy hinders cell proliferation at higher alloy ion concentrations. The cells that were treated with the 2 h and 8 h M-50 heat treated 100% extracts showed a significant increase ($P < 0.001$) in cell coverage between the means values compared with the negative control. The drop in cell coverage of the heat treated extracts is higher in magnitude than the as-cast extract. This suggests the heat treated M-50 100% extracts not only hinder healthy cell proliferation, but decreased the cytocompatibility of the M-50 system as well.

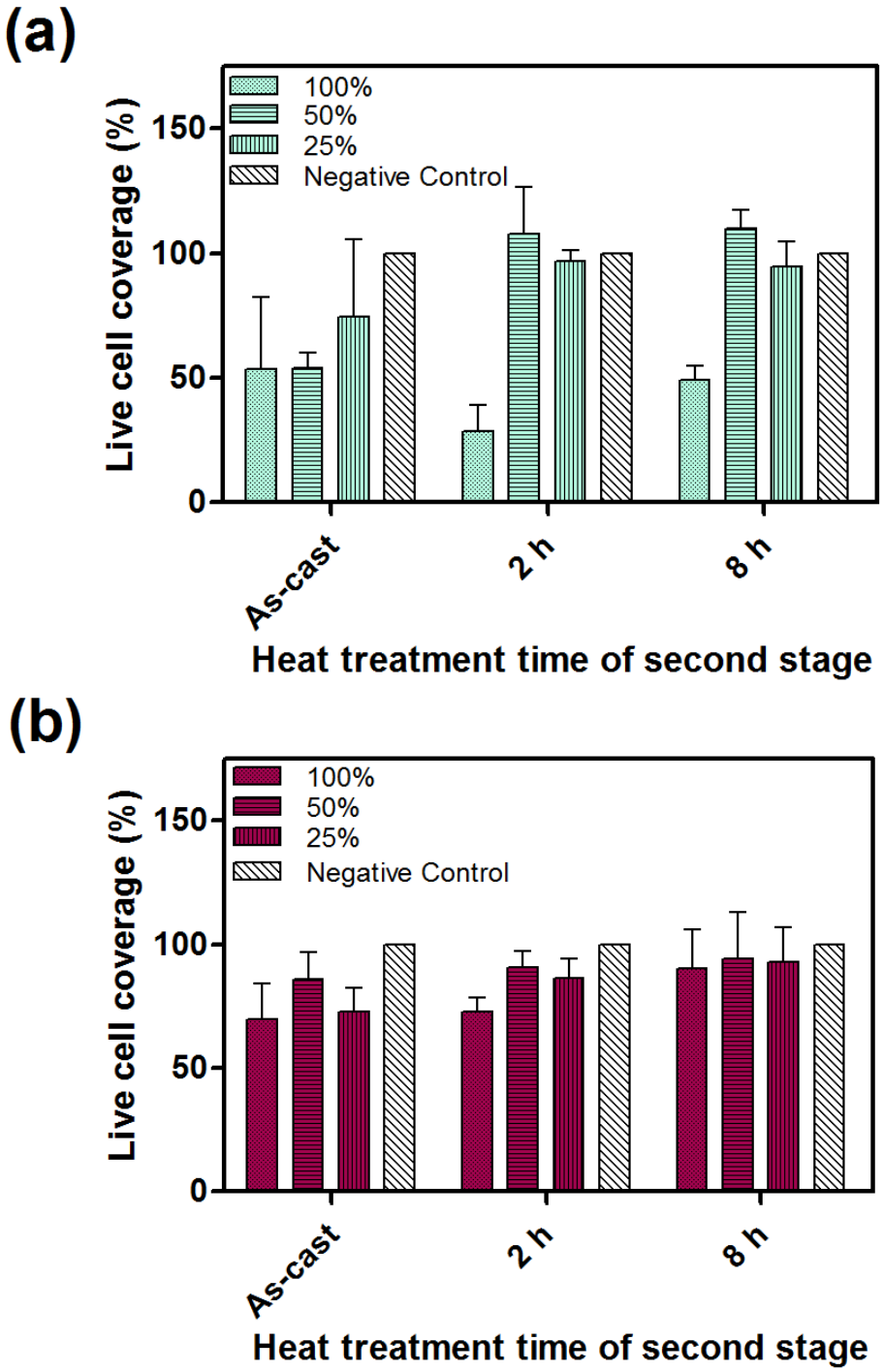

Figure 54. Average area of live cell coverage after 24 h of incubation based on the fluorescent OM Live/Dead images: a) M-50 extracts and b) MgZnCa−RE extracts.

The diluted heat treated extracts showed no significant difference from the negative control and the difference did not exceed 30% which indicates positive cytocompatiblity. This increase in the hindrance of cell proliferation of the heat treated extracts can attributed to the effects of the treatment processing on the microstructure of the M-50 alloys. Figure 33 describes how the treatment conditions significantly increased the grain size of the M-50 system which caused a significant reduction in corrosion resistance (Figure 48). The cytocompatibility of the extract solutions is based on the corrosion reactivity between the alloy and the corrosion medium. Consequently, the heat treated extracts consist of a higher concentration of Mg ions. However, the inherent biocompatible nature of the Mg, Zn, Ca elements resulted in the M-50 extracts not killing off the cells which is seen in the Live/Dead images. Optimizing the heat treatment processing is vital in creating viable biomaterials purposed for orthopaedic implant applications.

The live cell coverage illustrated in Figure 54b describe the OM staining images of cells incubated under MEMα extract composed of MgZnCa−RE alloys. The two-way ANOVA determined that the extract composition is considered to have a significant effect ($p < 0.05$ level [$F(2, 24) = 4.10$, $p = 0.0295$]) on the results and the extract dilution is considered to have a very significant impact ($p < 0.05$ level [$F(3, 24) = 7.28$, $p = 0.0012$]) on the results. It is determined that the reduction in the average area of live cell coverage of the cells incubated with the 100% as-cast MgZnCa−RE extract compared to the negative control is 30.5%. This difference barely meets the 30% constraint suggested by the ISO standard which indicates that the as-cast MgZnCa−RE extract is considered to have positive cytocompatibility with the cells. The diluted extracts show no significant difference and no need exceed 30% which is similar to the M-50 results.

The cells incubated with the 2 h heat treated extract also show a significant reduction in live cell coverage, but this reduction is not significant enough to suggest that the extract has negative cytocompatibility with the cells. The cell reduction for the 8 h extract is determined not to be significant and doesn't show any negative cytocompatibility. It can be noted that the 8 h heat treated extract has the best cell coverage compare to the 2 h and as-cast extracts and the as-cast has the worst. This trend can also be contributed to the effects of the treatment process on the microstructure of the MgZnCa−RE system. The grain size restricting nature of REEs in Mg during the treatment process coupled with the successful dissolution of solute atoms into the primary matrix caused a significantly increased in the corrosion resistance of the MgZnCa−RE system (Figure 50). According to the Live/Dead images and the live cell coverage data, the MgZnCa−RE system has shown to have an overall positive cytocompatibility with the MC3T3-E1 cell line.

4.4.1.4 Effects of protein-containing medium on the results. It must be noted that the cell medium composition and the presence of proteins within the medium can alter the corrosion characteristics of an alloy which ultimately can affect its cytocompatibility. There are many studies that show that *in vitro* and *in vivo* corrosion experiments differ in their results which stem from the fact that *in vivo* takes place in a very complicated environment which can affect its properties to some extent [117, 131-133]. As explained in section 4.3.1 of this dissertation, the corrosion medium has an impact on the speed and corrosion product formation. As a result, the tendency for corrosion to slow down when proteins are added to the corrosion medium regardless of medium composition [117]. For example, Willumeit *et al.* [117] incubated 99.94% pure Mg in DMEM under cell culture conditions for 74 h. It was determined that the osmolality of the solution, which can be attributed mainly to the Mg content of the solution, increased with

the increased amount of proteins within the solution. It is commonly believed that an increase of proteins in a solution would lead to corrosion resistance and consequently to a decrease in osmolality. However, Willumeit's findings contradict this paradigm but he does still conclude that the findings in his study point towards the belief that there is a mechanism of corrosion protection by proteins. In this study, the Mg alloys were immersed in FBS-containing MEMα medium which were seeded onto the cells. The protein found in this medium coupled with the buffering capacities could have helped strengthen the corrosion resistance in the MgZnCa−RE alloys which attributes to the positive cytocompatibility of the extract with the MC3T3-E1 cells.

4.4.2 MTT assay. The second study used to assess the cytocompatibility of the experimental alloys with the MC3T3-E1 cells was the MTT assay. The MTT assay assessment is a commonly used cytotoxicity test because it is a test that is financial accessible and easy to conduct. As discussed in section 3.5.3, this type of assay is a colorimetric assay that measures the transformation or reduction of yellow 3-(4,5-dimethythiazol-2-yl)-2,5-diphenyl tetrazolium bromide (MTT) by mitrochondrial succinate dehydrogenases in viable cells [134]. However, it must be noted that the use of a MTT test can lead to false positive or negative results in the case of Mg materials. This is caused by the ability of Mg in alkaline environments to produce tetrazolium salt, which could lead to a change in colors similar to the formation of formazan in MTT cells [44]. Consequently, the results could be different than what is actually occurring. Thus, in this study, the results of the MTT assay was closely compared to the results found in the Live/Dead study in the previous section.

4.4.2.1 Metabolic activity of the MgZnCa alloys. The total mitochondrial activity is related to the number of viable cells; therefore, the MTT assay is used to quantitatively evaluate the cytocompatibility of the experimental alloy extracts on the cells. The evaluation of the MTT

assay used in this study was based on the average percent of metabolic activity (Equation 12) of cells after 24 and 72 hours of incubation.

The percent of metabolic activity for cells treated with as-cast and heat treated M-50 MEMα extracts are presented in Figure 55. After 24 hours of incubation, it is determined that the 100% as-cast M-50 extract creates a significant reduction in metabolic activity compared to the negative control. This reduction is more than 30% which indicates a negative cytocompatible behavior. The metabolic activity of both the 100% heat treated extracts show a significant reduction compared to the negative control and also are determined to have a cytotoxic effect on the cells. This trend is in agreement with the live/dead cell coverage seen in Figure 54a. As discussed in the previous section, the corrosion behavior of the alloys attributed to the ionic release of Mg^{+2} after the 72 hours of static soaking of the M-50 alloys into the extract medium. Wang *et al.* [135] asserted that the Mg^{+2} concentration of the WE magnesium alloy extracts greatly varied in their cytotoxicity tests indicating that Mg^{+2} ions played a key role in the cytocompatibility evaluation *in vitro*.

In terms of comparing the as-cast and the heat treatment extracts to one another based off the negative control, it can be seen that there is no significant difference between the three extracts. These findings are consistent with Sun *et al.* [44] who concluded that there was no significant difference between the relative growth rate, which was determined from MTT assay analysis, of L-929 cells cultured in as-cast and extruded Mg−4.0Zn−0.2Ca extracts after 24 hours. The diluted extracts of all three conditions in this study show no significant difference with the negative control and therefore are considered to have good cytocompatibility with the cells outside of the 2 h heat treated extract which is treated as an outlier. This is also in agreement with the Live/Dead cell area of coverage done in this study.

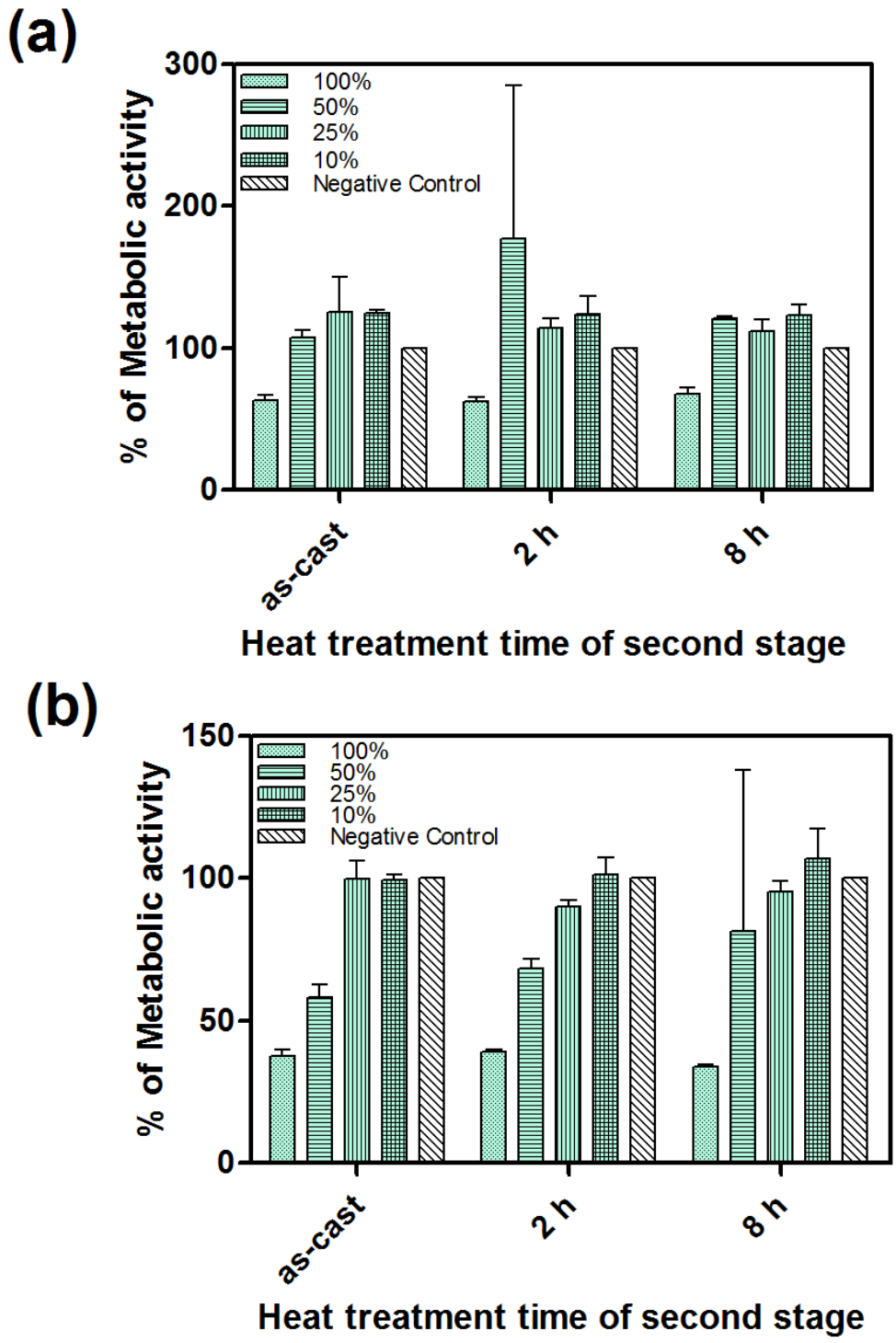

Figure 55. Average percent of metabolic activity of MC3T3 cells cultured under as-cast and heat treated M-50 extract dilutions for: a) 24 h and b) 72 h.

When studying the development of a grain structure, the size of the grains in an alloy varies with the rate of nucleation and growth which can influence certain mechanical and physical properties [62]. More specifically, smaller grains can alter the corrosion behavior and consequently the biological performance of an alloy. As stated previously in section 4.1.2, the one-way ANOVA compared the as-cast and heat treated (300°C 20 h + 480°C 2 h and 8 h) M-50 samples and determined that there was a significant difference in the mean grain size values among the differently processed alloys. This suggested that the treatment conditions used for this experiment had an effect on increasing the grain size through coalescence and therefore could be attributed to the metabolic levels of the corresponding cells showing reduced cytocompatibility with the M-50 alloy. Further studies must be done to determine if refining the grain size of the M-50 alloys may alter the cytocompatible behavior enough to acceptable levels.

After 72 hours, the extract compositions at the 100% and 50% dilutions significantly decreased in metabolic activity. This drop was significant enough to determine that both dilutions showed cytotoxic effects. This enhancement in negative cytocompatibility seen in the 100% and 50% dilutions may be attributed to the extended incubation time. This extended incubation time created an over absorption of the highly concentrated Mg^{+2} ions by the cells in the extract solutions. At the 25% and 10% dilutions, there were no cytotoxic effects shown for the three extract compositions. Overall, the metabolic activity of the extracts composed of higher Mg concentrations was reduced at an extended 72 hour incubation time compared to the first 24 hours. However the diluted extracts still showed no cytotoxic effects. More work must be done to understand what specific ions are in the extract and at what concentrations these ions exist to get a better understanding of the cytocompatibility of these alloys.

Ultimately the M-50 alloy system shows negative cytocompatibility when interacting with the MC3T3 cells according to both the MTT assay. According to the Live/Dead images this toxicity mainly affects the cell proliferation capabilities whereas the extracts do not have a major effect in terms of killing the cells. This affect in the hindrance of cell proliferation can be reduced or eliminated by diluting the extract which means the alloy system may be able to be employed in a biological system that has good fluid flow.

4.4.2.2 Metabolic activity of the MgZnCa−RE alloys. The percent of metabolic activity for cells treated with as-cast and heat treated MgZnCa−RE MEMα extracts are presented in Figure 56. For the initial 24 hour incubation time (Figure 56a), all three extracts at all dilutions show no significant difference compared to the negative controls. It must be noted that the 100% concentrated extracts all have high standard deviations which is due to outlier data points in each extract group which is indicative of measurement error or experimental error by the user. Additionally, the difference in means for each extract is less than 30% which denotes that there is positive cytocompatibility of the MgZnCa−RE alloys with the MC3T3 cells. This is in agreement with the qualitative and quantitative Live/Dead staining results seen in the previous section. After 72 hours (Figure 56b), it can be seen that 100% concentrated extracts show a significant decrease in metabolic activity compared to the negative controls which indicate a cytotoxic effect. Nonetheless, the diluted extracts still show no significant difference and no cytotoxic effects. RE containing Mg alloys showing good cell viability is a consistent occurrence to the point where Mg alloys with 5.2-9.9 wt.% RE and 3.7-5.5 wt.% Y have been claimed in a patent, and WE43 (4 wt.% Y and 3 wt.% RE) is a commercially available Mg alloy [9, 135].

Additionally, Feyerabend *et al.* [49] studies showed that the WE43 alloy is favorable to aluminum-containing alloys in terms of cell viability.

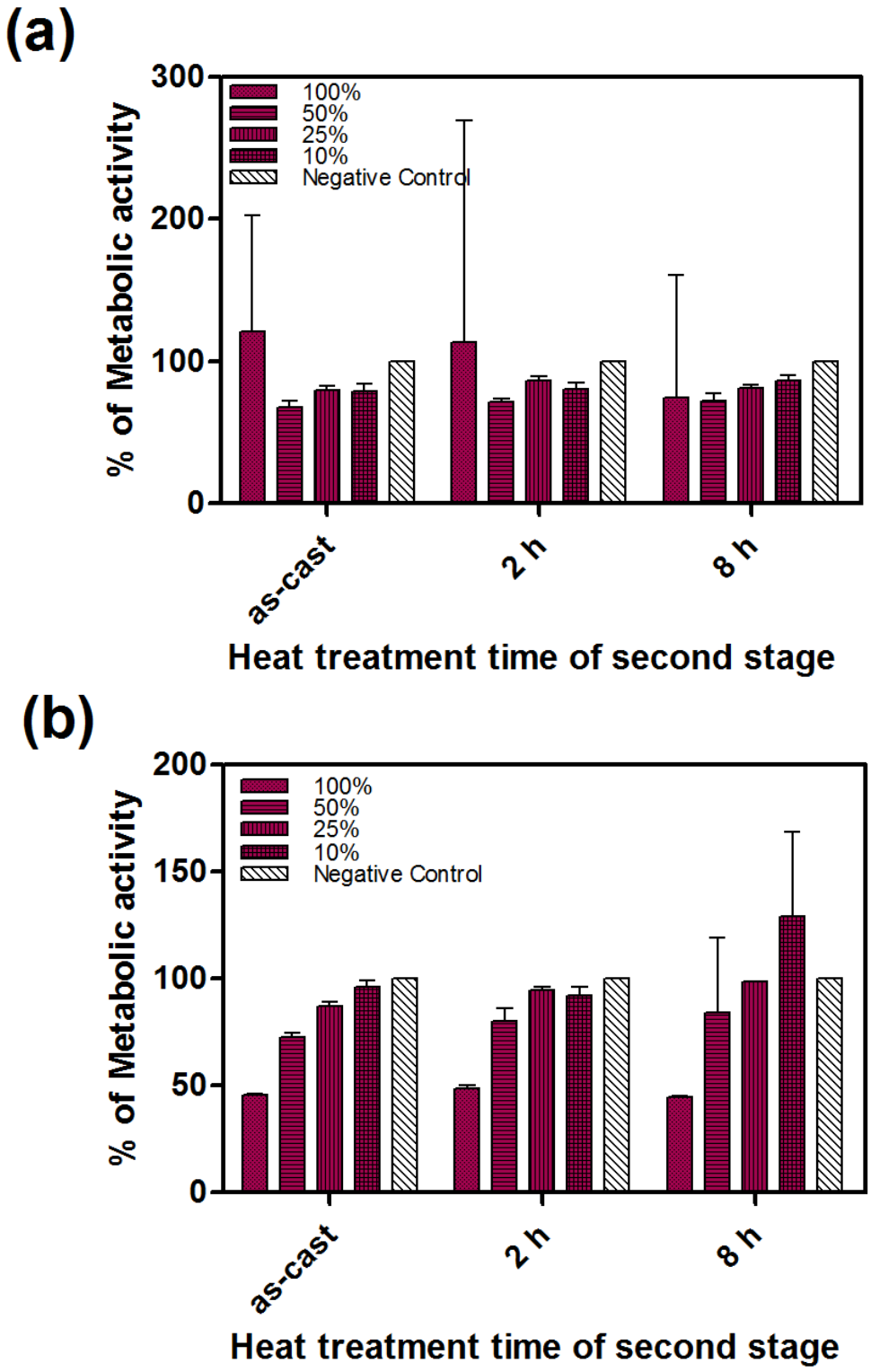

Figure 56. Average percent of metabolic activity of MC3T3 cells cultured under as-cast and heat treated MgZnCa−RE extract dilutions for: a) 24 h and b) 72 h.

However, the viability reactions exhibited by cells based of REEs vary from element to element. For example, for Mg alloys with high solid solubility's of Y, Gd, and Dy, Y was found to exhibit effects on viability and inflammatory reactions of macrophages, whereas the cellular reaction to Gd and Dy is comparably low [49].

4.4.2.3 Effects of using a cell line on the results. When performing, evaluating, and interpreting the *in vitro* cytotoxicity experiments, it is important to understand that the type of cell line used and the nature of the *in vitro* test conducted can play a major role in the analysis. For example, the human osteosarcoma cell line (MG63), tumor-derived mouse macrophage cell line (RAW 264.7), and human umbilical cord perivascular cells (HUCPV) were compared to understand the difference in reaction of cell lines and primary cells [49]. From the analysis of Mg and Ca, it was determined the RAW 264.7 are the most sensitive cells for the influence of salts, and HUCPV tends to be the most robust cellular assay system. Furthermore, it was concluded that primary osteoblasts showed a lower susceptibility to lanthanum (La) compared to MG63 cells.

The MC3T3-E1 cells used in this study are known as a cell line or sub-cloned cell which means they were derived from a primary cells. Primary cells are cells that are isolated straight from the tissue with no passages and therefore are morphologically similar to the parent tissue. Primary cells are considered by to be more physiologically similar to *in vivo* cells and represent the best experimental models for *in vivo* situations [136]. However primary cells are generally more difficult to culture than cell lines and ultimately have a limited life span. Cell lines are a more robust type of culture that can be utilized for long-term studies. They are also easier to work with than primary cells even though their behavior *in vitro* may not represent the *in vivo* situation. The rationale behind using cell lines in this study is based on the consideration that the

cytocompatibility assessment in this study is used an initial material screening evaluation for the experimental alloys. As a result, it was decided that using the more durable cell line culture was ideal.

4.5 Recommendations for Orthopaedic Applications and Further Discussion

There are four main criteria to consider when selecting implant materials. The first criterion that must be considered is the selection of a suitable application for the implementation of the implant material. Inherently, the purpose of this study is to develop biodegradable Mg implant materials for orthopaedic applications. Orthopaedics is a broad branch of medicine involving the musculoskeletal system. The purpose of an orthopaedic implant device, more specifically an implant device designed for the skeletal system, is to provide temporary mechanical support throughout the bone healing process. For biodegradable implants, the physical and mechanical integrity of the implant must be strong long enough to allow proper bone healing and then completely dissolve with an appropriate degradation rate that will not be harmful to the human body [137].

The second criterion to consider is the biological conditions within the environment that the implant material will be interacting. It is common knowledge that *in vitro* testing has its limitations in terms of the inconsistent correlation with *in vivo* results [33, 137]. The differences derive from the differences in the *in vitro* and *in vivo* environments in where the *in vivo* takes place in a very complex environment which can affect the material reaction to some extent [117, 131-133]. This was the motivation behind conducting immersion corrosion tests, in this study, in the MEMα cell culture solution for some of the experimental alloys. This was in an effort to test the experimental alloys in a solution that better represented what is seen in the *in vivo* in terms of the aqueous environment. The MEMα cell culture solution is more complex than the 0.9% NaCl

solution in terms of having an array of different amino acids, vitamins, inorganic salts, and other components. However, it is still recommended that the experimental alloys in this study should be examined through some sort of *in vivo* assessment. *In vivo* biocompatibility data will facilitate a better understanding of the possible biological capacities of the current experimental alloys. The third criterion to be considered is the biological response to the designed materials. Hort *et al.* [50] suggests that the impact of released alloying elements must be determined on human cells or cell lines for *in vitro* tests. For this study, the MC3T3-E1 cell line was used which is a cell line derived from mouse calvaria. Therefore it is recommended that further *in vitro* studies must be done on the experimental alloys developed in this study utilizing human cells to get a more acceptable depiction of the cytocompatibility in regards to humans. Furthermore, an MTT assay was utilized in this study for one of the quantitative cytocompatibility assessments. It has been shown that the use of Mg materials with a MTT assay is known to give false positives and false negatives [131, 138]. To combat against these effects, the MTT test in this study was confirmed by the Live/Dead staining results. As another recommendation, the MTT tests should be substituted with non-metabolic type assay. For example, the BrdU assay is an assay whose measurement principle is based on luminescence instead of absorption as seen with the MTT assays [139]. The BrdU assay detects Bromodeoxy Uridine (5-Bromo-2-DeoxyUridine, BrdU) nucleosides which are incorporated into cellular DNA during cell proliferation and therefore is a true measure of cell proliferation. Additionally, it was concluded that corroding Mg does not influence the results of the BrdU assay which makes it a more reliable assay when conducting cytocompatibility assessment on Mg alloys [131]. Moreover, in an effort to get a better representation of the cytocompatibility of the alloy, it is suggested that primary cell lines be used in future studies on the best materials because primary cell culture is more physiologically

similar to *in vivo* cells. Also understanding the relationship between ionic concentration and cell death is vital to getting better insight on the cytocompatibility behavior. Therefore it is suggested that inductively coupled plasma mass spectrometry (ICP-MS) be conducted which is an analytical technique used for elemental determinations and is capable of detecting metals and non-metals at concentrations as low as one part per million. Through the ICP-MS technique, specific species present within an extract can be determined.

The last criterion to consider when selecting an implant material is the material properties. The capability of the material in terms of degradation behavior and mechanical strength is important when assessing the implementation of said material into a suitable medical application. Hort *et al.* [50] explains that the selection of an application and the required properties provides a target for the design of implant materials and the material design must be adjusted until the material meet the target requirements.

For this study, the material properties of the experimental alloys were assessed and compared to the required properties of bone and literature suggestions to provide recommendations of on where the experiment alloys would garner possible success. Table 9 (Appendix) lists the average values for mechanical and physical properties of wet embalmed cortical bone from younger and older men [140]. Table 10 and Table 11 (Appendix) lists approximate estimates of the recovery time for different bone fractures and ligament tears respectively. For bone fractures, the implant mechanical support should last longer than 12 weeks depending on the clinical conditions. Additionally, Erinc *et al.* [141] recommended that the properties for biomaterials designed for bone fixtures needs to be as follows: corrosion rate less than 0.5 mm/year in simulated body fluid at 37°C; strengths higher than 200 MPa; and elongation higher than 10%. For the Mg−*x*Zn−0.3Ca alloys, the compressive strengths meet the

requirement suggested by Erinc. In terms of the ultimate tensile strengths, only the M-50 alloy met this criterion. However, cytotoxicity assays determined that the M-50 alloy has negative cytocompatibility with the MC3T3 cells according to ISO standards. The Live/Dead images indicated that this toxicity mainly affects the cell proliferation capabilities whereas the extracts do not have a major effect in terms of killing the cells because of the inherent biocompatible nature of the Mg, Zn, Ca elements. This affect in the hindrance of cell proliferation can be reduced or eliminated by diluting the extract. As a result, it is recommended that the M-50 alloy should be explored for use in biological systems that have good fluid flow. However, all of the Mg−*x*Zn−0.3Ca alloys produced in this study have a corrosion rate higher than 0.5 mm/year. More work must be done to optimize the Mg−*x*Zn−0.3Ca microstructure to produce more attractive materials properties.

In terms of the as-cast MgZnCa−RE samples, the tensile strength meets the 200 MPa requirement suggested by Erinc. However, the as-cast MgZnCa−RE has a corrosion rate of 2.4 mm/ year. This corrosion value is drastically reduced to around 0.46 mm/year after solution treatment which bolsters the cyto-compatibility of the system. Therefore the MgZnCa−RE alloy produced in this study has the potential to be successful as a biodegradable orthopaedic implant material. Further mechanical studies must be done on the heat treated MgZnCa−RE to confirm that the mechanical integrity is not altered after the introduction of heat treatment processing.

CHAPTER 5

Conclusion

The purpose of this study was to develop biodegradable Mg alloys for orthopaedic applications. The Mg−Zn−Ca alloy was the underpinning system for where these materials were developed from. The Zn content of this system was varied from 0.5 to 10.0 wt.% at a constant Ca composition of 0.3 wt.%. Optical microscopy images of these samples showed that the level of Zn content has an influence on the microstructure because the intermetallic phase observed along the grain boundaries and within the grains become more potent and the eutectics are thickened as the Zn concentration increases. Both the $CaMg_2$ and $Ca_2Mg_6Zn_3$ phases were detected in the alloys with a Zn level of 2.0%. As the Zn level increased to 6%, there was a suppression of the $CaMg_2$ phase. The $Mg_{12}Zn_{13}$ phase started to precipitate for the samples with 10% of Zn.

Based off the optical micrographs, it is also determined that there is a refinement in the average grain diameter by the increase of Zn content up to 4 wt.%. This reduction in grain size has a significant effect on the mechanical integrity and corrosion behavior of this group of as-cast alloys. The strength of the as-cast Mg−*x*Zn−0.3Ca alloy increases with the increased Zn content up to 4.0 wt.%. When Zn content exceeds more than 4.0 wt.%, the mechanical strengths decreases as a result of the Zn atom being rejected by the α-Mg and enhanced in the residual liquid in which often cause the formation of eutectic structures and micro-porosity. Additionally, the increase in Zn content caused an initial reduction in the corrosion rate up to 1 wt.% of Zn, but the corrosion rate experienced an overall increase as the Zn concentration increased to 10.0 wt.%.

The introduction of a double stage T4 solution treatment process on the Mg−3.0Zn−0.3Ca and Mg−4.0Zn−0.3Ca samples determined that solution temperatures ranging

from 400°C to 480°C with treatment times from 2 h to 144 h was able to activate the solute atoms enough for diffusion to occur which explains the significant decrease in secondary area compared to as-cast samples. However, due to the relatively high temperatures used for the heat treatment processing, most of the secondary phase at the grain boundaries dissolved causing grain assimilation which reduced the grain boundary density and increased the average grain diameter compared to the as-cast counterparts. Consequently, the corrosion resistance of the heat treated Mg−4.0Zn−0.3Ca samples is significantly reduced. This stems from the different electrochemical behaviors experienced between the α-Mg and the intermetallic secondary phase in which the $Ca_2Mg_6Zn_3$ phase acts as the cathode and α-Mg phase as the anode causing the α-Mg phase to corrode faster around the $Ca_2Mg_6Zn_3$ phase.

REEs were also introduced into the Mg−2.0Zn−0.3Ca alloy at 2.0 wt.%. It can be seen that the REEs have a grain refining effect on the Mg−*x*Zn−0.3Ca alloy since average grain diameter is considerably lower than the samples with no REEs. The secondary phase ($Mg_{74.8}Zn_{15.2}Nd_{4.3}Gd_{4.2}$) detected inside the grain boundaries of the MgZnCa−RE alloy, hinders the slip dislocation causing the MgZnCa−RE sample to have the highest yield strength, ultimate tensile strength, and elongation at failure values among the Mg−*x*Zn−0.3Ca alloys produced in this study. It can also be seen that the as-cast MgZnCa−RE alloy's corrosion rate is lower than the Mg−2.0Zn−0.3Ca counterpart with no rare earth additions because the REEs tend to ennoble the E_{corr} values of Mg alloys because the REEs are more thermodynamically stable and the MgZnCa−RE intermetallics themselves are resistant to corrosion.

The introduction of the double stage T4 solution heat treatment process on the as-cast MgZnCa−RE alloy creates a single phase type of microstructure. Additionally, REEs played an important role in restricting grain growth during the solution treatment process. As a result there

was a significant drop in the corrosion rates once the heat treatment conditioning is introduced because of the grain size restriction effect of REEs and the reduction of the galvanic coupling effect between the secondary phase and the primary matrix.

For the Mg−*x*Zn−0.3Ca alloys, the compressive strengths meet the requirement suggested by Erinc for materials designed for bone fixture implants. In terms of the ultimate tensile strengths, only the M-50 (Zn = 4%) alloy meets this criterion. However, cytotoxicity assays determined that the as-cast and heat treated M-50 alloys have negative cytocompatibility with the MC3T3 cells according to ISO standards. The Live/Dead images indicated that this toxicity mainly affects the cell proliferation capabilities whereas the extracts do not have a major effect in terms of killing the cells because of the inherent biocompatible nature of the Mg, Zn, Ca elements. This affect in the hindrance of cell proliferation can be reduced or eliminated by diluting the extract which means the alloy system may be able to be employed in a biological system that have good fluid flow. Additionally, all of the Mg−*x*Zn−0.3Ca alloys produced in this study have a corrosion rate higher than 0.5 mm/year, which exceeds the recommended rate; therefore more work must be done to optimize the Mg−*x*Zn−0.3Ca microstructure to produce more attractive materials properties. Nevertheless, the M-50 alloy is a good place to start the optimization utilizing heat treatment processing.

The MgZnCa−RE alloy may have potential to be successful as a biodegradable orthopaedic implant material because samples have positive cytocompatibility with the MC3T3 cells according to ISO standards and the tensile strengths meets the 200 MPa requirement suggested by Erinc. However, the as-cast MgZnCa−RE has a corrosion rate of 2.4 mm/ year which is a little high for orthopaedic implants. This corrosion value is drastically reduced to around 0.46 mm/year after T4 solution treatment which meets Erinc requirements. More

mechanical studies must be done on the heat treated MgZnCa−RE to confirm that the mechanical integrity is not altered after the introduction of heat treatment processing.

In summary, the study described in this dissertation shows that there is potential for the Mg−*x*Zn−0.3Ca alloy system to be developed into an orthopaedic implant material. Despite the challenges of obtaining ideal materials properties for biodegradable Mg alloys purposed for implantable applications, this alloy system can be constructed to meet implant requirements through unique heat treatment processing techniques and innovative alloying methods which include the addition of REEs. The necessity for innovation in medical devices that improve the quality of life through the creation of new alloys with the capabilities of biodegradation and bioabsorption without toxicity effects makes this alloy system worth the energy of future exploration and development and possible commercialization.

References

[1] *World preview 2013, outlook to 2018: the future of medtech,* in *EvaluateMedTech™ World Preview*, EvaluateMedTech™, Editor 2014: London, United Kingdom.

[2] *Orthopedic industry: market research reports, statistics and analysis.* Report Linker 2013; Available from: http://www.reportlinker.com/ci02254/Orthopedic.html.

[3] Slone, R., et al., *Orthopedic fixation devices.* Radiographics, 1991. **11**(5): p. 823-847.

[4] Westermark, A., et al., *The use of TMJ concepts prostheses to reconstruct patients with major temporomandibular joint and mandibular defects.* International Journal of Oral and Maxillofacial Surgery, 2011. **40**(5): p. 487-496.

[5] *Stryker: MTP CP plate*. 2013; Available from: http://footandanklefixation.com/product/mmi-mtp-cp-plate/.

[6] *Orthopedic hardware - UW radiology*. 2013; Available from: http://www.rad.washington.edu/academics/academic-sections/msk/teaching-materials/online-musculoskeletal-radiology-book/orthopedic-hardware.

[7] Curfman, G.D. and R.F. Redberg, *Medical devices-balancing regulation and innovation.* New England journal of medicine, 2011. **365**(11): p. 975-977.

[8] Moravej, M. and D. Mantovani, *Biodegradable metals for cardiovascular stent application: interests and new opportunities.* International journal of molecular sciences, 2011. **12**(7): p. 4250-4270.

[9] Witte, F., *The history of biodegradable magnesium implants: A review.* Acta Biomaterialia, 2010. **6**(5): p. 1680-1692.

[10] Friedrich, H.E. and B.L. Mordike, *Magnesium technology: metallurgy, design data, applications.* 2006.

[11] Shadkam, A., *A study of homogenization and precipitation hardening behaviour of magnesium-calcium-zinc alloys*, 2008, University of Waterloo (Canada): Canada. p. 178.

[12] Staiger, M.P., et al., *Magnesium and its alloys as orthopedic biomaterials: A review.* Biomaterials, 2006. **27**(9): p. 1728-1734.

[13] Huse, E., *A new ligature.* Chicago Med J Exam, 1878. **172**(2).

[14] Payr, E., *Beiträge zur technik der blutgefässe und nervennaht nebst mitteilunge ubre die verwendung eines resorbiebaren metallen in der chirurgie.* Arch. Klin. Chir, 1900. **62**: p. 67.

[15] Payr, E., *Zur verwendung des magnesiums für resorbirbare darmknöpfe und andere chirurgisch-technische zwecke.* Centralblatt Chir, 1901. **28**(20): p. 513-515.

[16] Lambotte, A., *L'utilisation du magnesium comme materiel perdu dans l'osteosynthèse.* Bull Mem Soc Nat Chir, 1932. **28**: p. 1325-1334.

[17] Verbrugge, J., *Le Matériel métallique résorbable en chirurgie osseuse, par Jean Verbrugge*1934: Masson.

[18] Groves, E.W.H., *An experimental study of the operative treatment of fractures.* British Journal of Surgery, 1913. **1**(3): p. 438-501.

[19] Zierold, A.A., *Reaction of bone to various metals.* Archives of Surgery, 1924. **9**(2): p. 365-412.

[20] Bobic, B., et al., *The effect of T4 heat treatment on the microstructure and corrosion behaviour of Zn27Al1.5Cu0.02Mg alloy.* Corrosion Science, 2011. **53**(1): p. 409-417.

[21] Dezellus, O., et al., *Mechanical testing of titanium/aluminium-silicon interface: Effect of T6 heat treatment.* Materials Science and Engineering: A. **528**(6): p. 2795-2803.

[22] Akhter, R., L. Ivanchev, and H.P. Burger, *Effect of pre/post T6 heat treatment on the mechanical properties of laser welded SSM cast A356 aluminium alloy.* Materials Science and Engineering: A, 2007. **447**(1-2): p. 192-196.

[23] Osório, W.R., et al., *Effects of eutectic modification and T4 heat treatment on mechanical properties and corrosion resistance of an Al-9 wt%Si casting alloy.* Materials Chemistry and Physics, 2007. **106**(2-3): p. 343-349.

[24] Li, H.-x., et al., *Ternary compounds and solid-state phase equilibria in Mg-rich side of Mg-Zn-Ca system at 300 °C.* Transactions of Nonferrous Metals Society of China, 2011. **21**(10): p. 2147-2153.

[25] Du, H., et al., *Effects of Zn on the microstructure, mechanical property and bio-corrosion property of Mg–3Ca alloys for biomedical application.* Materials Chemistry and Physics, 2011. **125**(3): p. 568-575.

[26] *Magnesium — health professional fact sheet*. 2009; Available from: http://ods.od.nih.gov/factsheets/Magnesium-HealthProfessional/.

[27] Wang, Y., et al., *In vitro degradation behavior of M1A magnesium alloy in protein-containing simulated body fluid.* Materials Science and Engineering: C, 2011. **31**(3): p. 579-587.

[28] Erne, P., M. Schier, and T. Resink, *The road to bioabsorbable stents: reaching clinical reality?* CardioVascular and Interventional Radiology, 2006. **29**(1): p. 11-16.

[29] Saris, N.-E.L., et al., *Magnesium: An update on physiological, clinical and analytical aspects.* Clinica Chimica Acta, 2000. **294**(1–2): p. 1-26.

[30] Wester, P.O., *Magnesium.* Am J Clin Nutr, 1987. **45**(5 Suppl): p. 1305-12.

[31] Zhang, E., et al., *Microstructure, mechanical and corrosion properties and biocompatibility of Mg-Zn-Mn alloys for biomedical application.* Materials Science and Engineering: C, 2009. **29**(3): p. 987-993.

[32] Xia, Y., et al., *In-vitro cytotoxicity and in-vivo biocompatibility of as-extruded Mg–4.0Zn–0.2Ca alloy.* Materials Science and Engineering: C, 2012. **32**(4): p. 665-669.

[33] Witte, F., et al., *In vivo corrosion of four magnesium alloys and the associated bone response.* Biomaterials, 2005. **26**(17): p. 3557-3563.

[34] Sudholz, A.D., et al., *Electrochemical behaviour and corrosion of Mg-Y alloys.* Corrosion Science, 2011. **53**(6): p. 2277-2282.

[35] Atrens, A., M. Liu, and N.I. Zainal Abidin, *Corrosion mechanism applicable to biodegradable magnesium implants.* Materials Science and Engineering: B, 2011. **176**(20): p. 1609-1636.

[36] Matsubara, H., et al., *Effect of impurity Fe on corrosion behavior of AM50 and AM60 magnesium alloys.* Corrosion Science, 2013. **66**(0): p. 203-210.

[37] Pan, F.S., et al., *Influence of impurities on microstructure and mechanical properties of ZK60 magnesium alloy.* Transactions of Nonferrous Metals Society of China, 2010. **20**(7): p. 1299-1304.

[38] *Calcium - element information, properties and uses | periodic table*. 2013; Available from: http://www.rsc.org/periodic-table/element/20/calcium.

[39] *Dietary supplement fact sheet: calcium — health professional fact sheet*. 2013; Available from: http://ods.od.nih.gov/factsheets/Calcium-HealthProfessional/.

[40] Li, Z., et al., *The development of binary Mg–Ca alloys for use as biodegradable materials within bone.* Biomaterials, 2008. **29**(10): p. 1329-1344.

[41] Bettles, C.J., M.A. Gibson, and K. Venkatesan, *Enhanced age-hardening behaviour in Mg–4 wt.% Zn micro-alloyed with Ca.* Scripta Materialia, 2004. **51**(3): p. 193-197.

[42] *Zinc - health professional fact sheet*. Available from: http://ods.od.nih.gov/factsheets/Zinc-HealthProfessional/.

[43] *Zinc (Zn) (chemical element) : history -- encyclopedia britannica*. 2013; Available from: http://www.britannica.com/EBchecked/topic/657264/zinc-Zn/8119/History.

[44] Sun, Y., et al., *Preparation and characterization of a new biomedical Mg–Zn–Ca alloy.* Materials & Design, 2012. **34**(0): p. 58-64.

[45] Langelier, B. and S. Esmaeili, *The effect of Zn additions on precipitation hardening of Mg-Ca alloys.* balance, 2010. **2**: p. 0.05.

[46] Ohishi, K., et al., *Age-hardening response of Mg–0.3 at.%Ca alloys with different Zn contents.* Materials Science and Engineering: A, 2009. **526**(1–2): p. 177-184.

[47] *Rare earth elements (REE)*. EniG. Periodic Table of the Elements 2013; Available from: http://www.periodni.com/rare_earth_elements.html.

[48] B. Haxel, G., J. B. Hedrick, and G. J. Orris. *Rare earth elements - critical resources for high technology* U.S. Geological Survey 2005; Available from: http://pubs.usgs.gov/fs/2002/fs087-02.

[49] Feyerabend, F., et al., *Evaluation of short-term effects of rare earth and other elements used in magnesium alloys on primary cells and cell lines.* Acta Biomaterialia, 2010. **6**(5): p. 1834-1842.

[50] Hort, N., et al., *Magnesium alloys as implant materials - principles of property design for Mg-RE alloys.* Acta Biomaterialia, 2010. **6**(5): p. 1714-1725.

[51] Birbilis, N., et al., *On the corrosion of binary magnesium-rare earth alloys.* Corrosion Science, 2009. **51**(3): p. 683-689.

[52] Zhang, T., et al., *Corrosion of hot extrusion AZ91 magnesium alloy. Part II: Effect of rare earth element neodymium (Nd) on the corrosion behavior of extruded alloy.* Corrosion Science, 2011. **53**(9): p. 2934-2942.

[53] Taslicukur, Z., C. Balaban, and N. Kuskonmaz, *Production of ceramic foam filters for molten metal filtration using expanded polystyrene.* Journal of the European Ceramic Society, 2007. **27**(2–3): p. 637-640.

[54] Campbell, J., *Castings* 2003: Butterworth-Heinemann.

[55] Mirak, A., et al., *Oxide film characteristics of AZ91 magnesium alloy in casting conditions.* International Journal of Cast Metals Research, 2007. **20**(4): p. 215-220.

[56] Tian, C., et al., *Effect of melt cleanliness on the formation of porosity defects in automotive aluminium high pressure die castings.* Journal of Materials Processing Technology, 2002. **122**(1): p. 82-93.

[57] Nazari, E., S.H. Razavi, and S.M.A. Boutorabi, *Effect of filtration on the morphology and mechanical properties of Mg molten alloy entering the mould cavity.* Journal of Materials Processing Technology, 2010. **210**(3): p. 461-465.

[58] Chen, F., et al., *Investigation on foam ceramic filter to remove inclusions in revert superalloy.* Materials Letters, 1998. **34**(3): p. 372-376.

[59] Wang, J., et al., *Effect of purification treatment on properties of Mg-Gd-Y-Zr alloy.* Transactions of Nonferrous Metals Society of China, 2010. **20**(7): p. 1235-1239.

[60] ASTM Standard B661-06, *Standard practice for heat treatment of magnesium alloys*, 2006, ASTM International West Conshohocken, PA

[61] Zhou, W., T. Shen, and N.N. Aung, *Effect of heat treatment on corrosion behaviour of magnesium alloy AZ91D in simulated body fluid.* Corrosion Science, 2010. **52**(3): p. 1035-1041.

[62] DeGarmo, E.P., J. Black, and A.R. Kohser, *Materials and processes in manufacturing: 8th ed.* Journal of Manufacturing Systems. Vol. 17. 1998, Upper Saddle River, NJ: Prentice-Hall. 235.

[63] Boyer, H.E., *Practical heat treating*1984, Metals Park, OH: American Society for Metals.

[64] William D. Callister, J., *Fundamentals of materials science and engineering: an integrated approach (second edition)*2005, Hoboken, NJ: John Wiley & Sons, Inc.

[65] Liu, X.-b., et al., *Effects of heat treatment on corrosion behaviors of Mg-3Zn magnesium alloy.* Transactions of Nonferrous Metals Society of China, 2010. **20**(7): p. 1345-1350.

[66] Hermawan, H., *Biodegradable metals: state of the art*, in *Biodegradable Metals*2012, Springer. p. 13-22.

[67] Witte, F., et al., *Biodegradable magnesium-hydroxyapatite metal matrix composites.* Biomaterials, 2007. **28**(13): p. 2163-2174.

[68] ISO, B., *10993-5: Biological evaluation of medical devices.* Tests for in vitro cytotoxicity, 1999.

[69] Zhang, X., *Bio-absorbable Mg-Zn-Ca three-elements magnesium alloy material*, S.I.P.O.o.t.P.s.R.o. China, Editor 2006, Shanghai Jiao Tong University: China.

[70] Gerold, B., *Implant with a base body of a biocorrodible magnesium alloy*, U.S.P.a.T. Office, Editor 2012, Biotronik Vi Patent: United States of America. p. 3.

[71] Zhang, B.P., Y. Wang, L. Geng, *Research on Mg–Zn–Ca alloy as degradable biomaterial*, in *Biomaterials - Physics and Chemisty* R. Pignatello, Editor 2011, InTech, Chapters. p. 183-204.

[72] Witte, F., *Current opinion of the science community on guidelines and testings of biodegradable metals*, 2012, Laboratory for Biomechanics and Biomaterials, Hannover Medical School: Hannover, Germany. p. 15.

[73] Levi, G., et al., *Solidification, solution treatment and age hardening of a Mg–1.6 wt.% Ca–3.2 wt.% Zn alloy.* Acta Materialia, 2006. **54**(2): p. 523-530.

[74] Hradilová, M., et al., *Structural and mechanical characteristics of Mg–4Zn and Mg–4Zn–0.4Ca alloys after different thermal and mechanical processing routes.* Materials Science and Engineering: A, 2013. **586**(0): p. 284-291.

[75] ASTM Standard E122-10, *Standard test methods for determining average grain size*, 2010, ASTM International West Conshohocken, PA

[76] *Brief introduction to scanning electron microscopy (SEM).* Manuals; Available from: http://micron.ucr.edu/public/manuals/Sem-intro.pdf.

[77] Hafner, B., *Scanning electron microscopy primer.* Characterization Facility, University of Minnesota-Twin Cities, 2007.

[78] Easton, M. *Scanning electron microscopy*. 2010; Available from: http://materialsworld.utep.edu/Background/SCANNING%20ELECTRON%20MICROSCOPY/SccaningElectronMicroscopy.htm.

[79] *Introduction to energy dispersive x-ray spectrometry (EDS).* Manuals; Available from: http://micron.ucr.edu/public/manuals/EDS-intro.pdf.

[80] ASTM Standard E9-09, *Standard test methods of compression testing of metallic materials at room temperature*, 2009, ASTM International: West Conshohocken, PA

[81] ASTM Standard E8/E8M, *Standard test methods for tension testing of metallic materials*, 2011, ASTM International: West Conshohocken, PA

[82] ASTM Standard E111-04, *Standard test method for young's modulus, tangent modulus, and chord modulus*, 2010, ASTM International: West Conshohocken, PA

[83] Skar, J.I., *Corrosion and corrosion prevention of magnesium alloys.* Materials and Corrosion, 1999. **50**(1): p. 2-6.

[84] Song, Y., et al., *The role of second phases in the corrosion behavior of Mg–5Zn alloy.* Corrosion Science, 2012. **60**(0): p. 238-245.

[85] Roberge, P. *Welcome to corrosion doctors* Corrosion Doctors 2012; Available from: http://www.corrosion-doctors.org/KTS/roberge.htm.

[86] Bender, S., et al., *A new theory for the negative difference effect in magnesium corrosion.* Materials and Corrosion, 2012. **63**(8): p. 707-712.

[87] Cramer, S.D. and B.S. Covino, *ASM handbook vol. 13A. corrosion: fundamentals, testing, and protection.* Materials Park, OH: ASM International, 2003. 1135, 2003.

[88] ASTM Standard G31-72, *Standard practice for laboratory immersion corrosion testing of metals*, 2004, ASTM International: West Conshohocken, PA

[89] Huan, Z., et al., *In vitro degradation behavior and cytocompatibility of Mg–Zn–Zr alloys.* Journal of Materials Science: Materials in Medicine, 2010. **21**(9): p. 2623-2635.

[90] Tunev, S.S., *Differences between in vitro, in vivo, and in silico studies.*

[91] Pan, T., et al., *In-vitro cytotoxicity assessment based on KC50 with real-time cell analyzer (RTCA) assay.* Computational Biology and Chemistry, (0).

[92] *Cytotoxicity*. Cellular Function 2013; Available from: http://www.moleculardevices.com/Applications/Cellular-Function/Cytotoxicity.html.

[93] Polli, J.E., *In vitro studies are sometimes better than conventional human pharmacokinetic in vivo studies in assessing bioequivalence of immediate-release solid oral dosage forms.* The AAPS journal, 2008. **10**(2): p. 289-299.

[94] Wang, D., et al., *Isolation and characterization of MC3T3-E1 preosteoblast subclones with distinct in vitro and in vivo differentiation/mineralization potential.* Journal of Bone and Mineral Research, 1999. **14**(6): p. 893-903.

[95] Bilezikian, J.P., L.G. Raisz, and T.J. Martin, *Principles of bone biology, two-volume set* 2008: Access Online via Elsevier.

[96] 10993-12, I.S., *Biological evaluation of medical devices: sample preparation and reference materials*, 1996, European Committee For Standardization

[97] van Meerloo, J., G.J. Kaspers, and J. Cloos, *Cell sensitivity assays: the MTT assay*, in *Cancer Cell Culture*2011, Springer. p. 237-245.

[98] Lane, D.M. *Analysis of variance*. 2013; Available from: http://onlinestatbook.com/2/analysis_of_variance/intro.html.

[99] Maxwell, S.E. and H.D. Delaney, *Designing experiments and analyzing data: A model comparison perspective*2004: Psychology Press.

[100] Seltman, H.J., *Experimental design and analysis.* Pittsburgh, PA: Carnegie Mellon University, 2012.

[101] Rumsey, D., *Statistics for dummies, 2nd edition*2011: Wiley. com.

[102] McCain, W.D. and W.T. Ziegler, *Critical temperature, critical pressure, and vapor pressure of argon.* Journal of Chemical & Engineering Data, 1967. **12**(2): p. 199-202.

[103] Bakhsheshi-Rad, H.R., et al., *Relationship between the corrosion behavior and the thermal characteristics and microstructure of Mg–0.5Ca–xZn alloys.* Corrosion Science, 2012. **64**(0): p. 184-197.

[104] Kubok, K., et al., *Investigation of structures in as-cast alloys from the Mg-Zn-Ca system* Archives of Metallurgy and Materials, 2013. **58**(2).

[105] Clark, J.B., *The solid constitution in the magnesium-rich region of the Mg-Ca-Zn phase diagram,* in *ASM Alloy Phase Diagram Center*, H.a.C. Okamoto, K., Editor 1961, ASM International: Materials Park, OH, USA.

[106] Wasiur-Rahman, S. and M. Medraj, *Critical assessment and thermodynamic modeling of the binary Mg–Zn, Ca–Zn and ternary Mg–Ca–Zn systems.* Intermetallics, 2009. **17**(10): p. 847-864.

[107] StJohn, D., et al., *Solidification of cast magnesium alloys.* 2003.

[108] Porter, D.A. and K.E. Easterling, *Phase transformations in metals and alloys.* 1992: CRC press.

[109] Alvarez-Lopez, M., et al., *Corrosion behaviour of AZ31 magnesium alloy with different grain sizes in simulated biological fluids.* Acta Biomaterialia, 2010. **6**(5): p. 1763-1771.

[110] Estrin, Y., M.X. Zhang, and N. Birbilis, *Surface grain size effects on the corrosion of magnesium.* Key Engineering Materials, 2008. **384**: p. 229-240.

[111] Ning, Z.L., et al., *Effects of Nd on microstructures and properties at the elevated temperature of a Mg–0.3Zn–0.32Zr alloy.* Materials & Design, 2010. **31**(9): p. 4438-4444.

[112] Gao, X., et al., *Precipitation-hardened Mg-Ca-Zn alloys with superior creep resistance.* Scripta Materialia, 2005. **53**(12): p. 1321-1326.

[113] Zhang, B., et al., *Mechanical properties, degradation performance and cytotoxicity of Mg–Zn–Ca biomedical alloys with different compositions.* Materials Science and Engineering: C, 2011. **31**(8): p. 1667-1673.

[114] Tong, G.-d., H.-f. Liu, and Y.-h. Liu, *Effect of rare earth additions on microstructure and mechanical properties of AZ91 magnesium alloys.* Transactions of Nonferrous Metals Society of China, 2010. **20, Supplement 2**(0): p. s336-s340.

[115] Witte, F., et al., *Degradable biomaterials based on magnesium corrosion.* Current Opinion in Solid State and Materials Science, 2008. **12**(5–6): p. 63-72.

[116] Witte, F., et al., *Biodegradable magnesium–hydroxyapatite metal matrix composites.* Biomaterials, 2007. **28**(13): p. 2163-2174.

[117] Willumeit, R., et al., *Chemical surface alteration of biodegradable magnesium exposed to corrosion media.* Acta Biomaterialia, 2011. **7**(6): p. 2704-2715.

[118] Feng, A. and Y. Han, *Mechanical and in vitro degradation behavior of ultrafine calcium polyphosphate reinforced magnesium-alloy composites.* Materials & Design, 2011. **32**(5): p. 2813-2820.

[119] Timothy, R.A., *Protons and osteoclasts.* Journal of Bone and Mineral Research, 1990. **5**(11).

[120] Frick, K.K. and D.A. Bushinsky, *Chronic metabolic acidosis reversibly inhibits extracellular matrix gene expression in mouse osteoblasts.* American Journal of Physiology-Renal Physiology, 1998. **275**(5): p. F840-F847.

[121] Kohn, D.H., et al., *Effects of pH on human bone marrow stromal cells in vitro: implications for tissue engineering of bone.* Journal of Biomedical Materials Research, 2002. **60**(2): p. 292-299.

[122] Bushinsky, D.A., J. Goldring, and F.L. Coe, *Cellular contribution to pH-mediated calcium flux in neonatal mouse calvariae.* American Journal of Physiology-Renal Physiology, 1985. **248**(6): p. F785-F789.

[123] Bushinsky, D.A., *Metabolic alkalosis decreases bone calcium efflux by suppressing osteoclasts and stimulating osteoblasts.* American Journal of Physiology-Renal Physiology, 1996. **271**(1): p. F216-F222.

[124] Frick, K.K., L. Jiang, and D.A. Bushinsky, *Acute metabolic acidosis inhibits the induction of osteoblastic egr-1 and type 1 collagen.* American Journal of Physiology-Cell Physiology, 1997. **272**(5): p. C1450-C1456.

[125] Krieger, N.S., N.E. Sessler, and D.A. Bushinsky, *Acidosis inhibits osteoblastic and stimulates osteoclastic activity in vitro.* American Journal of Physiology-Renal Physiology, 1992. **262**(3): p. F442-F448.

[126] Ralston, K.D., N. Birbilis, and C.H.J. Davies, *Revealing the relationship between grain size and corrosion rate of metals.* Scripta Materialia, 2010. **63**(12): p. 1201-1204.

[127] Chung, M.-K., et al., *Effect of the number of ECAP pass time on the electrochemical properties of 1050 Al alloys.* Materials Science and Engineering: A, 2004. **366**(2): p. 282-291.

[128] Tsai, T.C. and T.H. Chuang, *Role of grain size on the stress corrosion cracking of 7475 aluminum alloys.* Materials Science and Engineering: A, 1997. **225**(1–2): p. 135-144.

[129] Rokhlin, L.L., *Magnesium alloys containing rare earth metals: structure and properties*2003: Taylor & Francis.

[130] ISO, B., *Biological evaluation of medical devices - part 5: tests for in vitro cytotoxicity (ISO 10993-5:2009)*, 2009

[131] Fischer, J., et al., *Interference of magnesium corrosion with tetrazolium-based cytotoxicity assays.* Acta Biomaterialia, 2010. **6**(5): p. 1813-1823.

[132] Mueller, W.-D., M. Lucia Nascimento, and M.F. Lorenzo de Mele, *Critical discussion of the results from different corrosion studies of Mg and Mg alloys for biomaterial applications.* Acta Biomaterialia, 2010. **6**(5): p. 1749-1755.

[133] Gu, X., Y. Zheng, and L. Chen, *Influence of artificial biological fluid composition on the biocorrosion of potential orthopedic Mg–Ca, AZ31, AZ91 alloys.* Biomedical Materials, 2009. **4**(6): p. 065011.

[134] Hamid, R., et al., *Comparison of alamar blue and MTT assays for high through-put screening.* Toxicology in Vitro, 2004. **18**(5): p. 703-710.

[135] Wang, G., et al., *Study on the biodegradability and biocompatibility of WE magnesium alloys.* Materials Science and Engineering: C, (0).

[136] Provost, J., *Mammalian and plant cell culture*, in *Department of Biochemisty and Biotechnology*, M.S.U. Moorhead, Editor 2012: Moorhead, Minnesota.

[137] Moravej, M., et al., *Electroformed pure iron as a new biomaterial for degradable stents: In vitro degradation and preliminary cell viability studies.* Acta Biomaterialia, 2010. **6**(5): p. 1843-1851.

[138] Song, G.L. and A. Atrens, *Corrosion mechanisms of magnesium alloys.* Advanced Engineering Materials, 1999. **1**(1): p. 11-33.

[139] Muir, D., S. Varon, and M. Manthorpe, *An enzyme-linked immunosorbent assay for bromodeoxyuridine incorporation using fixed microcultures.* Analytical biochemistry, 1990. **185**(2): p. 377-382.

[140] Evans, F.G., *Mechanical properties and histology of cortical bone from younger and older men.* The Anatomical Record, 1976. **185**(1): p. 1-11.

[141] Erinc, M., et al., *Applicability of existing magnesium alloys as biomedical implant materials.* Magnesium technology, 2009: p. 209-214.

[142] Eiff, M.P. and R.L. Hatch, *Fracture management for primary care.* 2011: Elsevier Health Sciences.

[143] Rockwood, C.A., et al., *Rockwood and Green's fractures in adults*. Vol. 1. 2010: Wolters Kluwer Health.

Appendix

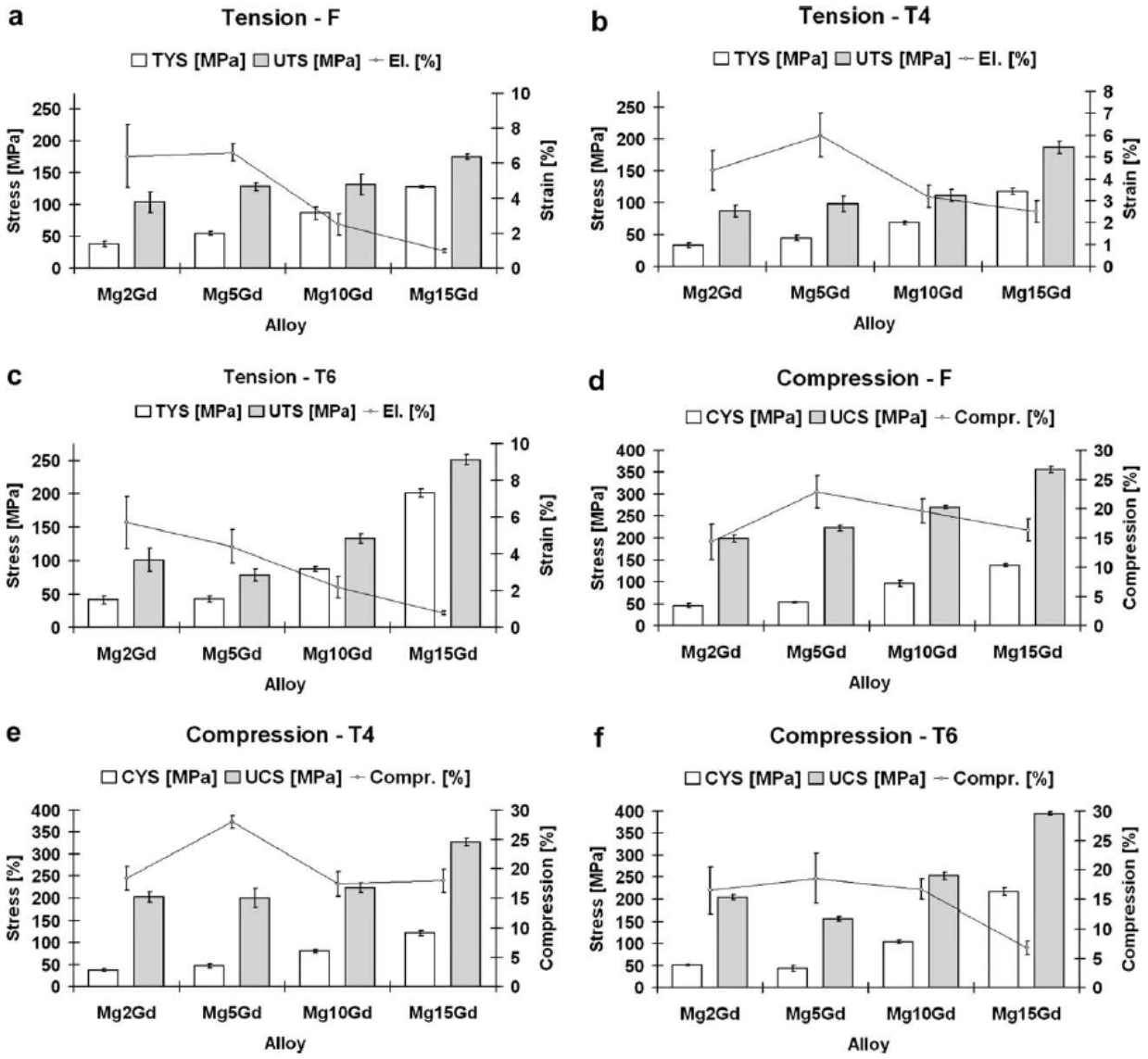

Figure 57. Mechanical properties of the Mg−Gd alloys in tension: (a) F (as-cast), (b) T4, and (c) T6; and in compression: (d) F, (e) T4 and (f) T6 [50].

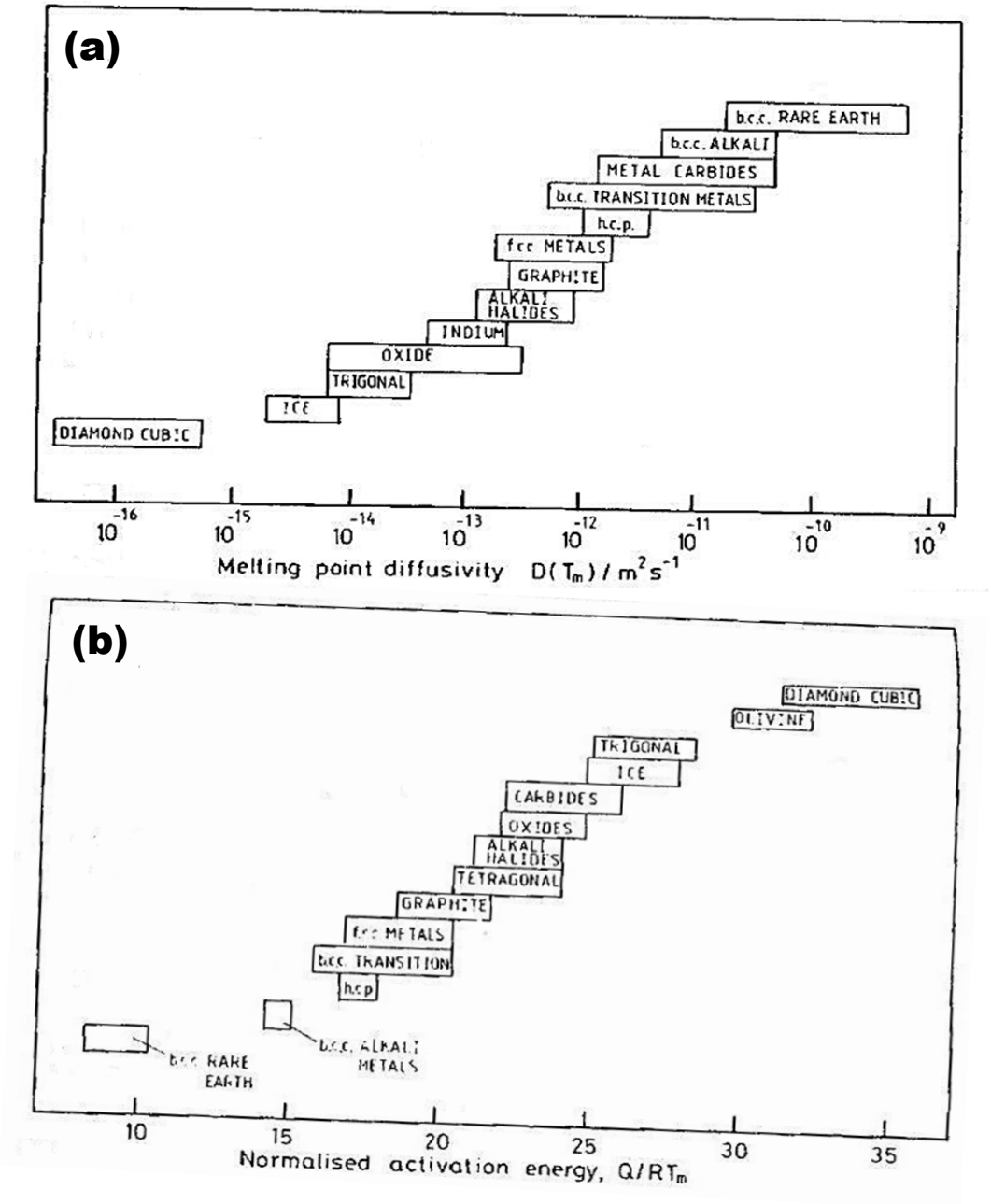

Figure 58. (a) Melting point diffusivities and (b) normalised activation energies for various classes of materials [108].

Table 7

SEM-EDS analysis of actual composition of the Mg−xZn−0.3Ca alloy system after casting.

Alloy Name	designed composition	actual composition					
		Mg		Zn		Ca	
	wt.%	wt.%	at.%	wt.%	at.%	wt.%	at.%
M-46	Mg-0.5Zn-0.3Ca	97.76	99.04	1.76	0.67	0.49	0.30
M-47	Mg-1.0Zn-0.3Ca	97.47	98.98	2.23	0.84	0.30	0.19
M-48	Mg-2.0Zn-0.3Ca	96.01	98.38	3.57	1.36	0.43	0.26
M-49	Mg-3.0Zn-0.3Ca	94.77	97.89	4.80	1.85	0.43	0.27
M-50	Mg-4.0Zn-0.3Ca	94.49	97.81	5.19	2.00	0.31	0.20
M-51	Mg-5.0Zn-0.3Ca	92.48	96.95	7.03	2.74	0.49	0.32
M-52	Mg-6.0Zn-0.3Ca	91.98	96.77	7.65	2.99	0.38	0.24
M-53	Mg-10.0Zn-0.3Ca	88.69	95.41	11.04	4.41	0.28	0.18

Table 8

Qualitative morphological grading of cytotoxicity of extracts [130].

Grade	Reactivity	Conditions of all cultures
0	None	Discrete intracytoplasmatic granules, no cell lysis, no reduction of cell growth.
1	Slight	Not more than 20 % of the cells are round, loosely attached and without intracytoplasmatic granules, or show changes in morphology; occasional lysed cells are present; only slight growth inhibition observable.
2	Mild	Not more than 50 % of the cells are round, devoid of intracytoplasmatic granules, no extensive cell lysis; not more than 50% growth inhibition observable.
3	Moderate	Not more than 70 % of the cell layers contain rounded cells or are lysed; cell layers not completely destroyed, but more than 50% growth inhibition observable.
4	Severe	Nearly complete or complete destruction of the cell layers.

Table 9

Average values for mechanical and physical properties of wet embalmed cortical bone from younger and older men [140].

Bone	Age	No. Specimen	Breaking Load (N)	UTS (MPa)	Elongation (%)	Modulus of Elasticity (MPa)	Density (g/cm3)
Femur	41.5	35	698.23	100.03	1.32	14.61	1.91
	71.0	35	560.94	66.69	1.07	13.34	1.85
Tibia	41.5	67	813.95	103.95	1.76	18.53	1.96
	72.0	34	694.31	82.38	1.56	15.89	1.83
Fibula	33.0	20	636.45	98.07	2.10	18.83	1.91
	59.0	16	564.86	78.45	1.19	14.91	1.73

Table 10

Estimated recovery times of common bone fractures [142].

Bone fracture	Recovery time (weeks)
fingers	3
metacarpals	4−6
distal radius	4−6
lower arm	8−10
humerus	6−8
femoral neck	12
femoral shaft	12
tibia	10
clavicle	3−12
scaphoid	12+
pelvis	8−12

Table 11

Estimated recovery times of ligament tears [143].

Ligament Rupture	Recovery time (months)
ACL	6−9
LCL	3
MCL	3
PCL	6−9